Complex photonic structures in nature: from order to disorder

Olimpia D. Onelli

Supervisor: **Dr. Silvia Vignolini**

Department of Chemistry
University of Cambridge

This dissertation is submitted for the degree of
Doctor of Philosophy

Murray Edwards College March 2018

To those who walk in heavy boots

Ibergekumene tsores iz gut tsu dertseyln

Declaration

I hereby declare that except where specific reference is made to the work of others, the contents of this dissertation are original and have not been submitted in whole or in part for consideration for any other degree or qualification in this, or any other university. This dissertation is my own work and contains nothing which is the outcome of work done in collaboration with others, except as specified in the text and Acknowledgements. This dissertation contains fewer than 60,000 words, including abstract, tables, and footnotes.

Olimpia D. Onelli
March 2018

Abstract

Structural colours arise from the interaction of visible light with nano-structured materials. The occurrence of such structures in nature has been known for over a century, but it is only in the last few decades that the study of natural photonic structures has fully matured due to the advances in imagining techniques and computational modelling. Even though a plethora of different colour-producing architectures in a variety of species has been investigated, a few significant questions are still open: how do these structures develop in living organisms? Does disorder play a functional role in biological photonics? If so, is it possible to say that the optical response of natural disordered photonics has been optimised under evolutionary pressure? And, finally, can we exploit the well-adapted photonic design principles that we observe in Nature to fabricate functional materials with optimised scattering response?

In my thesis I try to answer the questions above: I microscopically investigate *in vivo* the growth of a cuticular multilayer, one of the most common colour-producing strategies in nature, in the green beetles *Gastrophysa viridula* showing how the interplay between different materials varies during the various life stages of the beetles; I further investigate two types of disordered photonic structures and their biological role, the random array of spherical air inclusions in the eggshells of the honeyguide *Prodotiscus regulus*, a species under unique evolutionary pressure to produce blue eggs, and the anisotropic chitinous network of fibres in the white beetle *Cyphochilus*, the whitest low-refractive index material; finally, inspired by these natural designs, I fabricate and study light transport in biocompatible highly-scattering materials.

Table of contents

List of figures

List of tables

Chapter 1

General introduction

"Chaos was the law of nature; Order was the dream of man."

Henry Adams, *The Education of Henry Adams*

1.1 Structural colours

Visible light is loosely defined as the part of the electromagnetic spectrum that spans the range of wavelengths that are perceived as *colours* by the human eye [1]. Light plays an essential biological role in the vast majority of living organisms [2]. Intra- and inter-specific communication is based on the ability of producing and modifying colours and patterns for camouflaging, signalling, and mating purposes [3, 4]. Even in our contemporary society information is often colour-encoded when fast and accurate communication is required, as in the case of traffic lights or geographical maps [5].

Most colours in nature are caused by the selective absorption of certain wavelengths by chemicals known as *pigments* [6]. This phenomenon is defined as "subtractive colouration". When white light interacts with a pigment, part of the incident spectrum is absorbed and part is scattered: the latter is perceived as colour. Due to their versatility and availability, pigments are widely used in industrial applications as dyes or inks [7].

However, colour can also be obtained from the interference of light rather than its absorption [8]. Such structural colours (or *physical colours*), in fact, originate from the interaction of light with materials which are structured at the same length scale of the light wavelength. Therefore, by spatially modulating the refractive index of a material so that only the required colours are reflected (or transmitted) it is possible to introduce constructive or destructive interference [9].

Structural colours are common in living organisms and are often distinguishable from pigmentary colours by their metallic or iridescent appearance [10]. A common example are peacock feathers whose shimmering appearance has mesmerised scientists for millennia [11].

However, the interaction of light with nanostructures can also produce a matte, angularly-independent appearance [12]. This is typically the case when the modulation of the material is not periodic: the presence of a certain degree of disorder cancels the angular correlations needed to produce iridescence [13].

In fact, disorder in photonic structures explain a variety of phenomena, ranging from strong whiteness (*i.e.* the reflection of all colours) to anisotropic angular responses [14, 15] and depolarisation effects [16, 17].

1.2 Investigating complex photonic structures

Understanding how a particular colouration relates to a specific structure is, in most cases, far from trivial. A variety of imaging and analytical techniques are necessary to disentangle the complex interplay between the various contributions.

Typically, the first step is individuating the colour-producing architecture. To achieve this, a number of imaging techniques are used, from optical to x-ray and electron microscopy [18]. These methods generally allows one to estimate the characteristic sizes of the structures which determine their interaction with light.

The reflected or transmitted spectra also need to be quantified in terms of intensity as well as their angular dependence. This can be achieved both macro- and micro-scopically by optical spectroscopy. Reliable quantification is key for the comparison of the performance of various materials. Furthermore, spectroscopic data can help detect the contribution of pigmentary colours due to their characteristic "subtractive" spectrum. It is also important to consider the vision system of the organisms involved and interpret the measured optical signal considering the sensitivity of the organisms' photoreceptors to the different wavelengths.

Finally, theoretical calculations and numerical experiments can further assist in correlating the spectral information with the structure. For example, it is possible to use numerical models to predict the optical response of a given structure and compare the accuracy of the agreement with the one measured experimentally.

Historically, periodic photonics have been the first to be explored and only recently the attention has shifted to disordered systems [19]. This is most probably due to the higher

complexity of random systems whose investigation requires more advanced imaging and computational techniques [20].

1.3 Synopsis

This thesis tackles the subject of structural colour from two different ends. On one hand, it focuses on the fundamental understanding of the evolution and development of structural colours in biology. On the other, it investigates methods for the fabrication of photonic materials using both natural structures as templates and scalable bottom-up approaches.

The thesis is structured as follows:

Chapter 2 lays out the theoretical background needed to understand and predict light propagation in periodic as well as disordered systems.

Chapter 3 introduces the experimental techniques necessary to extract information about a photonic material. The emphasis is on the imaging techniques used to map the colour-producing architectures.

Chapter 4 reviews the most recent advances in the field of natural disordered photonics. This includes a discussion of the various strategies observed in nature for producing extraordinary optical responses.

Chapter 5 presents the first developmental study of the multilayer responsible for the green colouration of the dock beetle *Gastrophysa viridula*.

Chapter 6 focuses on the study of the interplay of pigmentary and structural colouration in avian species which are competing for the nesting resources.

Chapter 7 begins with a discussion of the evolutionary advantage of the photonic structure observed in white beetle *Cyphochilus* and continues with the description of two techniques for using such optimised architecture as a template for the fabrication of strongly scattering materials.

Chapter 8 introduces a novel technique for the production of cellulose-based scattering materials which are tuneable in whiteness.

Chapter 9 summarises the findings of the preceding chapters in the light of the aims of the thesis and offers a perspective on the possible future work.

Chapter 2

Theoretical Background

To comprehend the interaction of light with matter, one needs to understand the fundamentals of the electromagnetic field's propagation, as described by Maxwell's equations. In this chapter, the theoretical framework for describing light propagation in homogeneous and layered media will be introduced. Then, some fundamental aspects of the interaction of light with complex (or random) media will be analysed, highlighting how these systems cannot easily be described by Maxwell's equations and require, instead, to be re-interpreted in terms of the diffusion equation. Finally, the limit in which normal diffusion becomes anomalous will be discussed in relation to light propagation.

2.1 Wave propagation in homogeneous media

2.1.1 The electromagnetic field

The whole of classical electromagnetism can be described by just four relationships, Maxwell's equations [21]:

$$\nabla \cdot \mathbf{D} = \rho, \tag{2.1}$$

$$\nabla \cdot \mathbf{B} = 0, \tag{2.2}$$

$$\nabla \times \mathbf{E} = -\frac{\partial \mathbf{B}}{\partial t}, \tag{2.3}$$

$$\nabla \times \mathbf{H} = \mathbf{J} + \frac{\partial \mathbf{D}}{\partial t}. \tag{2.4}$$

These equations relate vector and scalar fields, where:
ρ is the charge density (in C/m^3)
D is the electric flux density (or electric displacement, in C/m^2)
B is the magnetic flux density (or magnetic induction, in Wb/m^2)
E is the electric field vector (or electric field strength, in V/m)
H is the magnetic field vector (or magnetic field strength, in A/m)
J is the electric current density (in A/m^2)

Maxwell's equations can be uniquely solved only if the relationship between **B** and **H** as well as the one between **E** and **D** are known. Therefore, two more equations are necessary - these are known as "constitutive equations" (or "material equations") [22]:

$$\mathbf{D} = \varepsilon\mathbf{E} = \varepsilon_0\mathbf{E} + \mathbf{P}, \tag{2.5}$$

$$\mathbf{B} = \mu\mathbf{H} = \mu_0\mathbf{H} + \mathbf{M}, \tag{2.6}$$

where ε and μ are known as permittivity and permeability; **P** and **M** are the electric and magnetic polarisation of the medium, respectively. ε_0 is the permittivity of vacuum while μ_0 is its permeability.
The most important result that can be derived from Maxwell's equations is the existence of electromagnetic waves. Applying the curl operator to Equation 2.3 gives [21]

$$\nabla\times\nabla\times\mathbf{E} = -\frac{\partial\nabla\times\mathbf{B}}{\partial t}. \tag{2.7}$$

By applying the "curl of the curl" identity

$$\nabla\times(\nabla\times\mathbf{u}) = \nabla(\nabla\cdot\mathbf{u})-\nabla^2\mathbf{u}, \tag{2.8}$$

equation 2.7 becomes

$$\nabla(\nabla\cdot\mathbf{E})-\nabla^2\mathbf{E} = -\frac{\partial\nabla\times\mathbf{B}}{\partial t}. \tag{2.9}$$

Hence, in absence of charges or currents, one obtains

$$\nabla^2\mathbf{E} = \mu\varepsilon\ddot{\mathbf{E}}, \tag{2.10}$$

a wave equation for the electric field (n.b. $\ddot{\mathbf{E}} = \frac{\partial^2\mathbf{E}}{\partial t^2}$). Similarly, a wave equation for the **H**-field can be derived.

This result implies the existence of electromagnetic waves propagating in vacuum at velocity c,

$$c = \frac{1}{\sqrt{\mu_0 \varepsilon_0}}. \tag{2.11}$$

In a medium, light propagates at velocity

$$v = \frac{c}{n}, \tag{2.12}$$

where $n = \sqrt{\mu\varepsilon/\mu_0\varepsilon_0}$. This quantity is known as *refractive index* and is typically "dispersive", meaning that it varies with frequency. The refractive index n is a complex number where the imaginary part is the *extinction coefficient* which indicates the amount of attenuation when the electromagnetic wave propagates through the material. In the framework of this thesis, it is assumed that $\mu = \mu_0$ (as in most diamagnetic materials), allowing for the simplification $n = \sqrt{\varepsilon/\varepsilon_0}$.

It can be shown that plane waves in the form

$$\mathbf{E} = \mathbf{u}_1 E_0 e^{i(\omega t - \mathbf{k}\cdot\mathbf{r})} \tag{2.13}$$

satisfy Maxwell's equation in free-space with phase velocity as in Equation 2.12, frequency ω, wave propagation vector $\mathbf{k}$, and position $\mathbf{r} = (x, y, z)$ in Cartesian coordinates ($\mathbf{u}_1$ is a unit vector normal to the direction of propagation and E_0 is the amplitude of the electric field at time $t = 0$ and position $\mathbf{r} = (0,0,0)$) [23].

2.1.2 Snell's law and Fresnel equations

After defining the form of the propagating electromagnetic field in a homogeneous medium, it is possible to analyse what occurs at an interface between two media. Due to the continuity of Maxwell's equations, a wave (as in Equation 2.13) with frequency ω and propagation vector $\mathbf{k}_0$) impinging on a surface will be generally split into two components, assuming that the absorption is negligible: a reflected and a transmitted wave, as shown in Figure 2.1. The condition to be satisfied for continuity using coordinates $\mathbf{r}$ is [24]

$$(\mathbf{k}_i \cdot \mathbf{r})_{x=0} = (\mathbf{k}_r \cdot \mathbf{r})_{x=0} = (\mathbf{k}_t \cdot \mathbf{r})_{x=0}, \tag{2.14}$$

where the subscripts i, r, and t indicate the incident, reflected, and transmitted wave respectively.

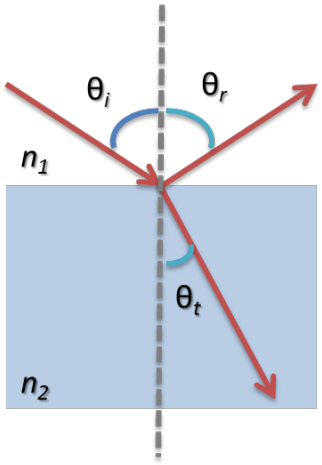

Fig. 2.1 A light beam propagating through a medium of refractive index n_1 is incident on a slab of material of refractive index n_2 at angle θ_i. The beam is partly reflected back at an angle θ_r and partly transmitted at an angle θ_t.

Hence, the following continuity relation must hold:

$$n_1 \sin\theta_i \quad = \quad n_1 \sin\theta_r \quad = \quad n_2 \sin\theta_t, \tag{2.15}$$

leading to Snell's law [24]

$$\frac{\sin\theta_i}{\sin\theta_t} \quad = \quad \frac{n_2}{n_1}. \tag{2.16}$$

At this point, two boundary conditions at the interface must be imposed: the components of electric fields parallel to the plane of incidence (denoted by subscript s) need to be continuous as well as the perpendicular components of the magnetic field (denoted by subscript p). This implies that for the case of incidence from above:

$$E_{1,s} + E'_{1,s} \quad = \quad E_{2,s}, \tag{2.17}$$

where E_1 is the incident amplitude where, E'_1 is the reflected amplitude, and E_2 is the transmitted amplitude.

Given that $E = vB$ and $\theta_1 = \theta_2$ where θ_1 and θ_2 are the angles of the wave vectors k_1 and k_2,

$$\sqrt{\frac{\varepsilon_1}{\mu_1}}(E_{1,s} - E'_{1,s})\cos\theta_1 \quad = \quad \sqrt{\frac{\varepsilon_2}{\mu_2}}E_{2,s}\cos\theta_2. \tag{2.18}$$

Hence, defining the reflection and transmission coefficients r_s and t_s for a single interface as

$$r_s \quad = \quad \frac{E'_{1,s}}{E_{1,s}}, \quad t_s \quad = \quad \frac{E_{2,s}}{E_{1,s}}, \tag{2.19}$$

one obtains

$$r_s = \frac{n_1 \cos\theta_1 - n_2 \cos\theta_2}{n_1 \cos\theta_1 + n_2 \cos\theta_2}, \tag{2.20}$$

and

$$t_s = \frac{2n_1 \cos\theta_1}{n_1 \cos\theta_1 + n_2 \cos\theta_2}. \tag{2.21}$$

Similarly, for the perpendicular components of the field, it can be shown that:

$$r_p = \frac{n_1 \cos\theta_2 - n_2 \cos\theta_1}{n_1 \cos\theta_2 + n_2 \cos\theta_1}, \tag{2.22}$$

and

$$t_p = \frac{2n_1 \cos\theta_1}{n_1 \cos\theta_2 + n_2 \cos\theta_1}. \tag{2.23}$$

These four equations are known as Fresnel formulas [25].

2.2 Wave propagation in layered media

2.2.1 Matrix formulation for multilayer systems

The theoretical framework introduced so far can be used to solve any isotropic layered media system. However, iterating the calculation for a large number of layers can become challenging due to the increasing number of equations involved. Thus, a matrix-based approach has been developed in order to provide a systematic method to analyse such systems. The method is particularly suitable to be implemented computationally [26] and is known as *transfer-matrix method*.

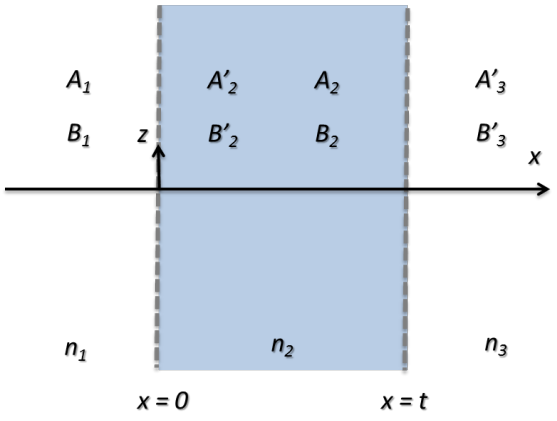

Fig. 2.2 A thin layer of refractive index n_2 placed between two media of refractive indices n_1 and n_2. $A(x)$ and $B(x)$ are the amplitude of the left- and right-propagating field at position x.

Considering light propagation in a thin film of thickness t and refractive index n_2 placed between two layers of infinite thickness and refractive indices n_1 and n_3 (Figure 2.2), the electric field $E(x)$ consists of left- and right-propagating waves, $A(x)$ and $B(x)$ respectively:

$$E(x) = A(x) + B(x). \tag{2.24}$$

In each of the portions of the volume, it is possible to define, for each interface, the electric fields as follows:

$$\begin{aligned} A_1 &= A(x = 0^-), \\ B_1 &= B(x = 0^-), \\ A_2^{'} &= A(x = 0^+), \\ B_2^{'} &= B(x = 0^+), \\ A_2 &= A(x = t^-), \\ B_2 &= B(x = t^-), \\ A_3^{'} &= A(x = t^+), \\ B_3^{'} &= B(x = t^+). \end{aligned} \tag{2.25}$$

Recalling the continuity equations (Equation 2.17-2.18), now one can rewrite A and B in matrix notation as

$$\begin{pmatrix} A_1 \\ B_1 \end{pmatrix} = \mathbf{D}_1^{-1}\mathbf{D}_2 \begin{pmatrix} A_2^{'} \\ B_2^{'} \end{pmatrix} \equiv \mathbf{D}_{12} \begin{pmatrix} A_2^{'} \\ B_2^{'} \end{pmatrix}, \tag{2.26}$$

$$\begin{pmatrix} A_2^{'} \\ B_2^{'} \end{pmatrix} = \mathbf{P}_2 \begin{pmatrix} A_2 \\ B_2 \end{pmatrix} = \begin{pmatrix} e^{i\phi_2} & 0 \\ 0 & e^{-i\phi_2} \end{pmatrix} \begin{pmatrix} A_2 \\ B_2 \end{pmatrix}, \tag{2.27}$$

$$\begin{pmatrix} A_2 \\ B_2 \end{pmatrix} = \mathbf{D}_2^{-1}\mathbf{D}_3 \begin{pmatrix} A_3^{'} \\ B_3^{'} \end{pmatrix} \equiv \mathbf{D}_{23} \begin{pmatrix} A_3^{'} \\ B_3^{'} \end{pmatrix}, \tag{2.28}$$

where $\mathbf{D}_1$, $\mathbf{D}_2$, and $\mathbf{D}_3$ are defined as the *dynamical matrices* given by

$$\mathbf{D}_i = \begin{cases} \begin{pmatrix} 1 & 1 \\ n_i\cos\theta_i & -n_i\cos\theta_i \end{pmatrix} \text{for } s \text{ waves}, \\ \begin{pmatrix} \cos\theta_i & \cos\theta_i \\ n_i & -n_i \end{pmatrix} \text{for } p \text{ waves}, \end{cases} \tag{2.29}$$

where $i = 1,2,3$ and θ_i is the angle in each layer.

The *propagation matrix* $\mathbf{P}_2$ describes the propagation through the bulk of the layer with phase ϕ

$$\phi_2 \quad = \quad k_{x,2}t \tag{2.30}$$

where the subscript x indicates the x-component of the wavevector $\mathbf{k}$. Hence, the amplitude of the field to the left of the layer is related to the amplitude to the right by

$$\begin{pmatrix} A_1 \\ B_1 \end{pmatrix} \quad = \quad \mathbf{D}_1^{-1}\mathbf{D}_2\mathbf{P}_2\mathbf{D}_2^{-1}\mathbf{D}_3 \begin{pmatrix} A_3^{'} \\ B_3^{'} \end{pmatrix}. \tag{2.31}$$

In other words, the column vectors describing the field in each layer are related by a 2x2 matrix product. Each interface is represented by a dynamical matrix while the bulk material is described by a propagation matrix.

To extend this approach to multilayers with N layers, it is possible to reiterate the matrix formulation for each layer and their interfaces - leading to

$$\begin{pmatrix} A_0 \\ B_0 \end{pmatrix} \quad = \quad \begin{pmatrix} M_{11} & M_{12} \\ M_{21} & M_{22} \end{pmatrix} \begin{pmatrix} A_S^{'} \\ B_S^{'} \end{pmatrix}, \tag{2.32}$$

with

$$\begin{pmatrix} M_{11} & M_{12} \\ M_{21} & M_{22} \end{pmatrix} = \mathbf{D}_0^{-1} \left[\prod_{j=1}^{N} D_j P_j D_j^{-1} \right] \mathbf{D}_S, \tag{2.33}$$

where $A_S^{'}$, $B_S^{'}$ are the amplitudes at $x = x_N$.

The reflectance is given by

$$R \quad = \quad |r|^2 \quad = \quad \left| \frac{M_{21}}{M_{11}} \right|^2. \tag{2.34}$$

The expression for $\mathbf{M}$ becomes complicated as the number of layers increase: in such cases, the model is typically handled computationally. A number of open source codes are available. In this work, the script developed and tested in [27] is adapted by the author to study light propagation in biological materials.

2.2.2 Examples

While the quantitative evaluation of the reflectivity can be rather complex, it is important to qualitatively understand how each parameter affects independently the overall response.

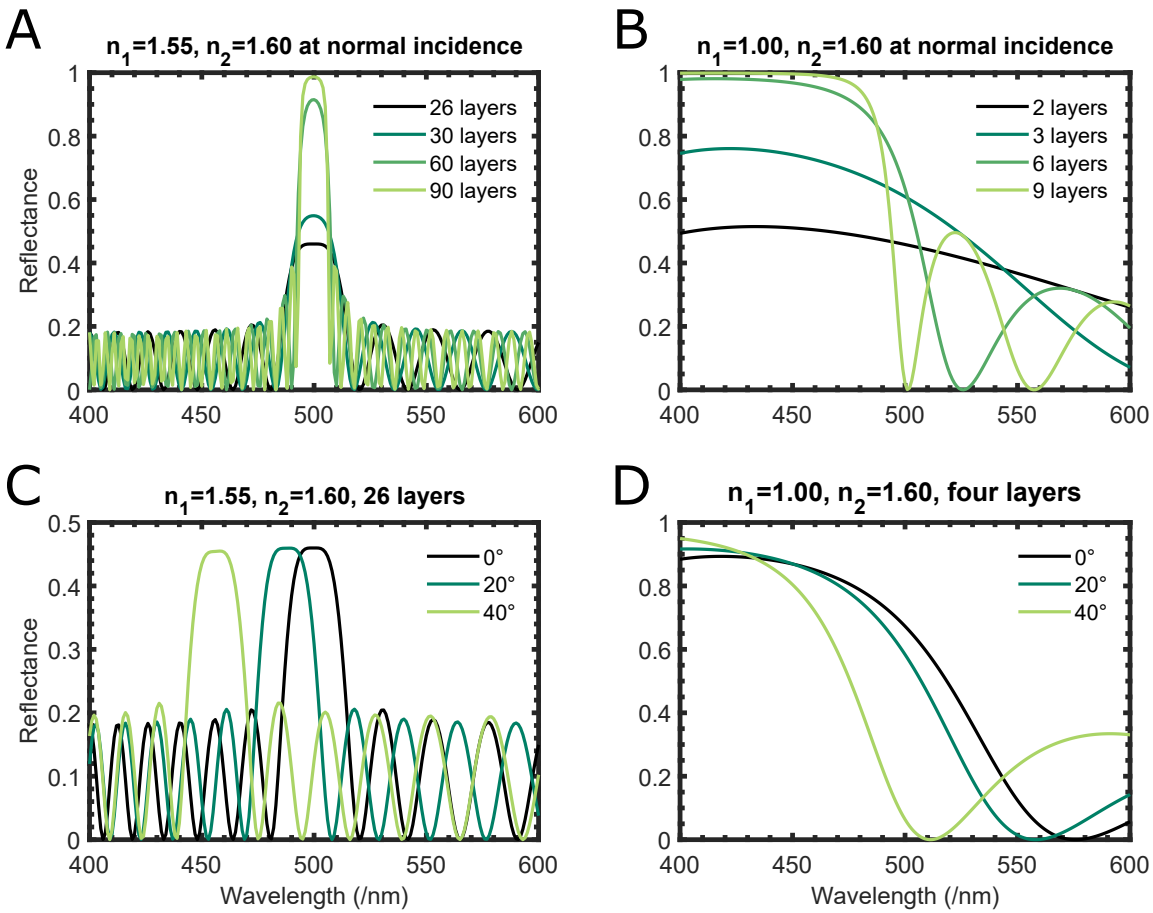

Fig. 2.3 The effect of varying the refractive index contrast, number of layers, and incident angle on a multilayer (*s*-polarisation only). The thickness of layer 1 is 81 nm; the thickness of layer 2 is 78 nm. Design based on [28].

Here, the role of the refractive index, layer thickness and number, and angle of incidence is discussed.

Multilayers can be categorised as *ideal* and *non-ideal* depending on whether the following condition is satisfied or not [29]:

$$n_1 t_1 \quad = \quad n_2 t_2, \tag{2.35}$$

where n_1 and n_2 are the refractive indices of layers of thickness t_1 and t_2, respectively. Equation 2.35 implies that the optical length of the layers is constant for ideal multilayers - the main consequence of this is that the reflectivity peak is symmetric in this case [19].

Figure 2.3 shows the reflectance of multilayers that have refractive index difference Δn between the layers: in panel A the difference is smaller than in B (0.05 and 0.60, respectively).

Note how the larger Δn is, the higher the reflectance is; thus, fewer layers are needed to achieve unity. However, an increase in Δn leads to an increase in the bandwidth.

Moreover, it can be noticed how the optical response varies as a function of the angle of incidence of the incoming light (Figure 2.3C-D). This phenomenon is known as *iridescence*, a signature trait of thin film and multilayer structural colouration.

Additionally, the peak reflectivity increases with increasing number of layers. In addition, it is possible to observe that there is a background oscillation of 0-20% (Figure 2.3A). This is due to the Δn between air and the stack being larger than the interlayer Δn, meaning that the multilayer itself behaves as a thin film [19].

Finally, two more factors that influence the optical response are the dependence of the refractive index on the wavelength and the absorption of the material. Both of them can change the overall shape and intensity of the reflected (or transmitted) signal significantly. However, both are often neglected when building computational models leading to inconclusive results. Arguably, this is due to the difficulty of measuring n (especially in biological samples) even though a few techniques are available, Jamin-Lebedeff interferometry being the most widely spread [30, 31].

2.3 Wave propagation in random media

White is the colour that the human eye perceives when exposed to light which contains all the wavelengths in the visible spectrum with similar intensity [32]. Typically, white colourations are produced by diffuse broadband reflection of light from randomly dispersed scattering centres [33]. The scattering centres, or scattering particles, are regions where the refractive index n is different with respect to the surrounding medium.

Light scattering is a phenomenon that is often regarded as a nuisance. For example, in the field of astronomy, the glare from the surrounding fog can dramatically worsen the quality of a telescope's measurement [34, 35]. However, studying and understanding scattering can lead not only to the reduction of glare but also to many other interesting applications: ranging from imaging through turbid media [36, 37] and light trapping for energy harvesting [38], to the optimisation of white coatings and paints [39].

2.3.1 Light transport in random media

When light encounters a scattering centre embedded in the propagation medium it deviates from its straight path (also known as "ballistic path", Figure 2.4) so that the direction of propagation is eventually completely randomised after sufficient scattering events.

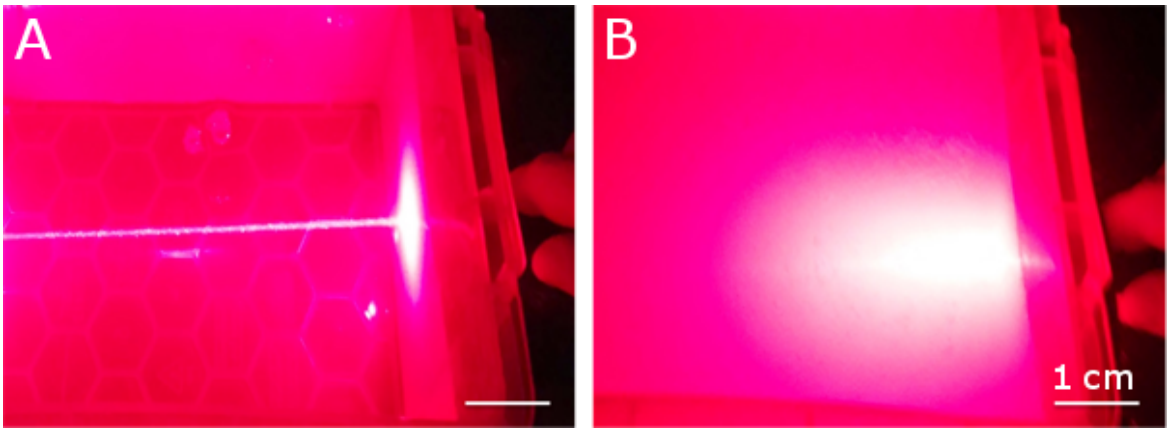

Fig. 2.4 A: a laser beam propagating ballistically through a tank of clear water. Due to minimal scattering from impurities it is possible to see the beam which would otherwise be invisible. B: the intensity of the beam is diffused laterally when milk, whose particles act as scatterers, is added to the tank.

For a sufficiently large number of particles where the arrangement of the scatterers is not periodic, light does not propagate in a straight line but is instead affected by multiple scattering events. As a consequence, the system cannot be modelled as the sum of the contribution from the individual particles. This approach would be extremely demanding in terms of computational power (as Maxwell's equations would need to be solved at each scattering event), requiring billions of interactions for a bulk material.

It is from classical mechanics that one can draw inspiration to solve the seemingly insurmountable problem of multiple scattering. When modelling many-particle systems, the Newtonian laws of motion have to be abandoned to embrace a more probabilistic model [40]. This does not imply that multiple scattering is itself a random phenomenon (it is, in fact, uniquely predicted by Maxwell's equations) but only that it is more easily treated as a stochastic process [41].

2.3.2 The diffusion approximation and the scattering mean free path

Each scattering event can be either elastic, when there is no change in the electromagnetic field amplitude or frequency of the incoming light, or inelastic, when the field changes in amplitude or frequency [42]. The latter is the case of absorption. This work is mainly concerned with the case of elastic scattering and how this phenomenon can be quantified and modelled. Therefore, absorption will be neglected.

It is possible to approximate the photons' propagation between scattering events to a random walk. This interpretation relies on the assumption that each scattering event is

independent from the previous one and that the scatterers are identical and homogeneously dispersed in the medium.

Approximating the light path to a random walk implies that the same mathematical framework that applies to diffusive regimes such as Brownian motion [43] can now be applied to the scattered light. Hence, the probability of a photon travelling undisturbed a distance Δx decays exponentially with the average step-length l_s [44]:

$$P(\Delta x) \quad \sim \quad e^{-\Delta x/l_s}. \tag{2.36}$$

The quantity l_s (known as *scattering mean free path*) is inversely proportional to the density of scatterers N and to the scattering cross-section σ_s, defined as the effective area that quantifies the intrinsic likelihood of a scattering event [44]:

$$l_s \quad = \quad (N\sigma_s)^{-1}. \tag{2.37}$$

The scattering cross-section is not necessarily isotropic. This means that a single scattering event does not necessarily produce the complete randomisation of the direction of the light propagation. This bias is taken into account by introducing a key quantity in the formalism of scattered light, the *transport mean free path*, l_t [44]:

$$l_t \quad = \quad \frac{l_s}{1- < \cos\theta >}, \tag{2.38}$$

where $< \cos\theta >$ is the average cosine of the scattering angle (that is, the angle between the direction of light propagation before and after the scattering event). In other words, the transport mean free path represents the length over which the light loses memory of its initial direction of propagation.

Both θ and the scattering cross-section σ_s depend on the geometry and size of the scatterers. Assuming spherical scatterers, one can identify different scattering regimes depending on their diameters, D, with respect to the wavelength of the incident light, λ. If $D \ll \lambda$, then it is possible to observe either Thomson scattering (for the particles are charged, *e.g.* free electrons in the solar corona) [45] or Rayleigh scattering [46] (for neutral particles) which is responsible for the blue colouration of the sky [47]. Rayleigh's model breaks down when $D \sim \lambda$, as the geometry of the particles start to play an important role in shaping the scattered field. In this case, Mie scattering describes the interaction [48], which is observed in many emulsions such as milk and paint. Finally, if $D \gg \lambda$, it is possible to use the ray approximation for modelling the scattering events. This regime is known as "geometrical

scattering" and explains, for example, the phenomenon of rainbows [49].

Knowing σ_s and N, l_s can be calculated as follows. Considering light propagating through a medium of finite thickness L, the transport regime can either be described by the single scattering approximation when l_s is long (*i.e.* small σ_s and low N) or by multiple scattering when l_s is short (*i.e.* large σ_s and high N). In the single scattering regime, the transport of the unscattered (or ballistic) light in space r and time t through a slab of material follows Lambert-Beer law [50]

$$I(\mathbf{r},t) \quad = \quad I(0,t)e^{-\mathbf{r}/l_s}, \tag{2.39}$$

where $I(\mathbf{r})$ is the intensity of the ballistic beam of light at position $\mathbf{r}$.

In the multiple scattering regime, light propagation can instead be approximated by the diffusion equation [51]

$$\frac{\partial I(\mathbf{r},t)}{\partial t} \quad = \quad D\nabla^2 I(\mathbf{r},t) - \frac{v_e}{l_i} I(\mathbf{r},t) + S(\mathbf{r},t), \tag{2.40}$$

in which $S(\mathbf{r},t)$ is the light source, v_e is the electromagnetic energy transport group velocity [52] diffusing with constant D, and l_i is the absorption length, over which the light intensity decays by a factor $1/e$. Since ballistic light travels a shorter path than diffuse light to reach the same depth, the diffusive absorption length l_A is shorter than l_i and is given by [42]

$$l_A \quad = \quad \sqrt{(l_s l_i)/3}. \tag{2.41}$$

The solution to Equation 2.40 can be calculated for different propagation medium geometries. However, all the diffusive systems described in this work are reasonably approximated by a slab geometry. Thus, it is important to impose the relevant boundary conditions dictated by this particular spatial configuration. For a light source positioned at $x = (s,0)$ inside a diffusive slab of thickness L, the simplest boundary condition assumes that the diffuse intensity is null at the physical limits of the slab (in Figure 2.5 this would be $x = 0$ and $x = L$). This statement excludes the possibility that the diffuse intensity can be reflected at the slab boundaries. A better approximation is to impose that the diffuse intensity falls to zero at distance z_e outside the slab (Figure 2.5). The quantity z_e is known as "extrapolation length" and can be calculated as [53]

$$z_e \quad = \quad \frac{2}{3}\left(\frac{1+R^D}{1-R^D}\right) l_s, \tag{2.42}$$

where R^D is the reflectivity at the boundaries (averaged over all angles and polarisations). According to [54],

$$\left(\frac{1+R^D}{1-R^D}\right) \quad = \quad V(n), \tag{2.43}$$

where V depends only on the effective refractive index n_{eff} (the exact form of V can be found in [54] as well as a polynomial expansion to simplify what is a fairly complicated expression). Equation 2.43 can be extremely useful when measuring R^D is experimentally impracticable.

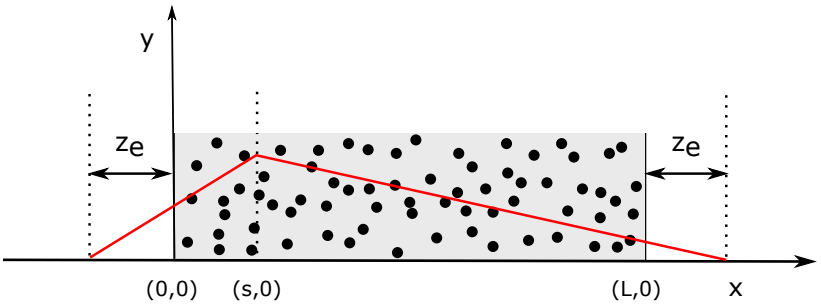

Fig. 2.5 Diagram showing the solution of the diffusion equation (in red) for a δ-light source at position (0,s) inside a random medium extending from x = 0 to x = L and infinite in the y and z directions. The extrapolation length z_e marks the boundary conditions. Design based on [55].

Given the boundary conditions discussed above for a slab extending from $x = 0$ to thickness $x = L$

$$I(x) \quad = \quad 0 \quad \text{at} \quad \begin{cases} z = -z_e, \\ z = L + z_e, \end{cases} \tag{2.44}$$

the solution to the diffusion equation in 2.40 can be shown to be [56]

$$T(L,\lambda) = \frac{\cosh(z_e/l_A)\sinh(5z_e/3l_A)}{\sinh(L+2z_e/l_A)}, \tag{2.45}$$

where T is the total transmittance through the slab.

In a system where $L \gg l_s$ and negligible absorption, T can be approximated to [55]

$$T(L,\lambda) \simeq \frac{1}{1+AL} \propto l_s/L, \tag{2.46}$$

where $A = (2z_e)^{-1}$.

2.3.3 Anomalous diffusion through random media

In the framework of light diffusion presented above, the average square distance, $\langle x^2 \rangle$, travelled by light increases linearly with time t, as in the case of Brownian motion [57]:

$$\langle x^2 \rangle \quad = \quad Dt^{\gamma}, \tag{2.47}$$

where D is the diffusion constant and γ is a parameter that describes the diffusion regime ($\gamma = 1$ in this case). This formalism relies upon two key assumptions: the existence of a mean free path and a mean time between two scattering events [58]. In recent years a number of examples have been found in which these two statements do not hold [57]. In these systems, $\langle x^2 \rangle$ can grow faster than linearly (*i.e.* $\gamma > 1$, known as "superdiffusive regime") or more slowly (*i.e.* $\gamma < 1$, known as "subdiffusive regime") [59]. Collectively, these phenomena are known as *anomalous diffusion* [57].

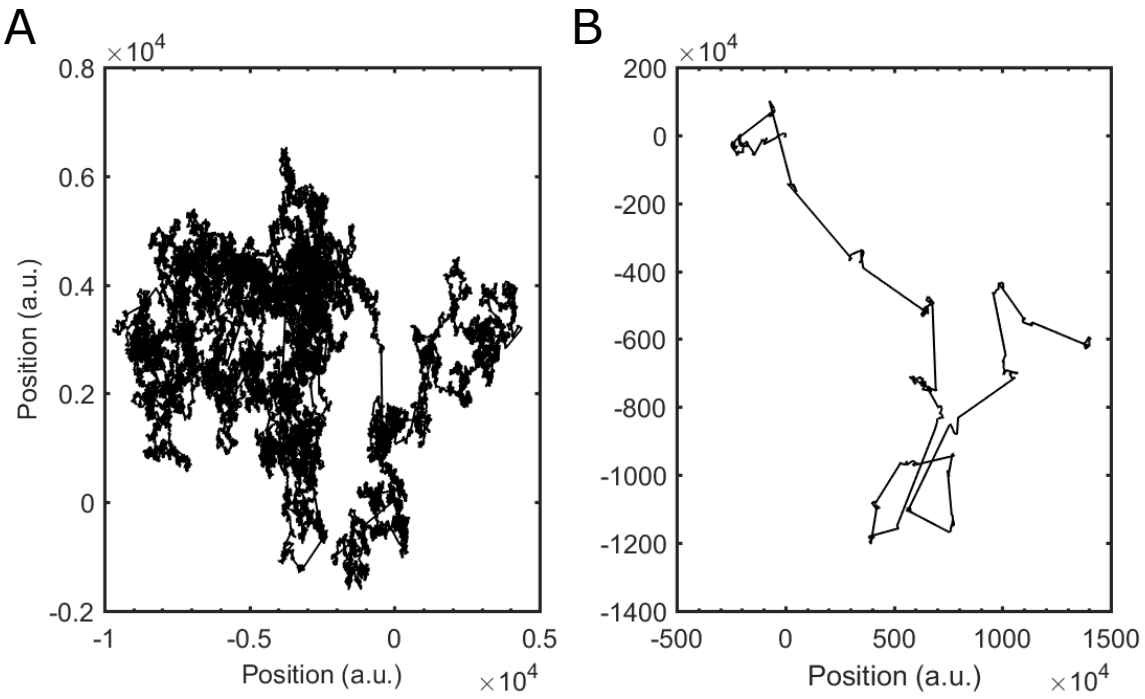

Fig. 2.6 Examples of random walks with unit step size. A: normal diffusion is characterised by a uniform distribution of step lengths. B: superdiffusive systems can explore a larger area due to the occurrence of longer steps as compared to normally diffusive ones. MATLAB script for random walk generation adapted from [60].

Anomalous diffusion is caused by the breakdown of the central limit theorem [59] which states that when independent variables of finite variance are added, their sums tends toward a normal distribution [61]. In other words, in anomalous systems the distribution of the paths

is not Gaussian so that one cannot define a meaningful average step-length (Figure 2.6). In particular, this can be caused by anomalies in the spatial distribution of the steps or in the time spent covering each step. In fact, the exponent γ can be further separated into its spatial and temporal component, σ and κ, which are defined in relation to the steps probability distribution P as function of length r and time intervals Δt [62]:

$$P(r) \sim r^{-\sigma}, \tag{2.48}$$

$$P(\Delta t) \sim \Delta t^{-1-\kappa}, \tag{2.49}$$

so that

$$\gamma = \begin{cases} \sigma/2\kappa & if \quad \sigma < 2 \quad and \quad \kappa < 1, \\ \sigma/2 & if \quad \sigma < 2 \quad and \quad \kappa \geqslant 1, \\ 1/\kappa & if \quad \sigma \geqslant 2 \quad and \quad \kappa < 1, \\ 1 & if \quad \sigma \geqslant 2 \quad and \quad \kappa \geqslant 1, \end{cases} \tag{2.50}$$

giving the phase diagram reported in Figure 2.7.

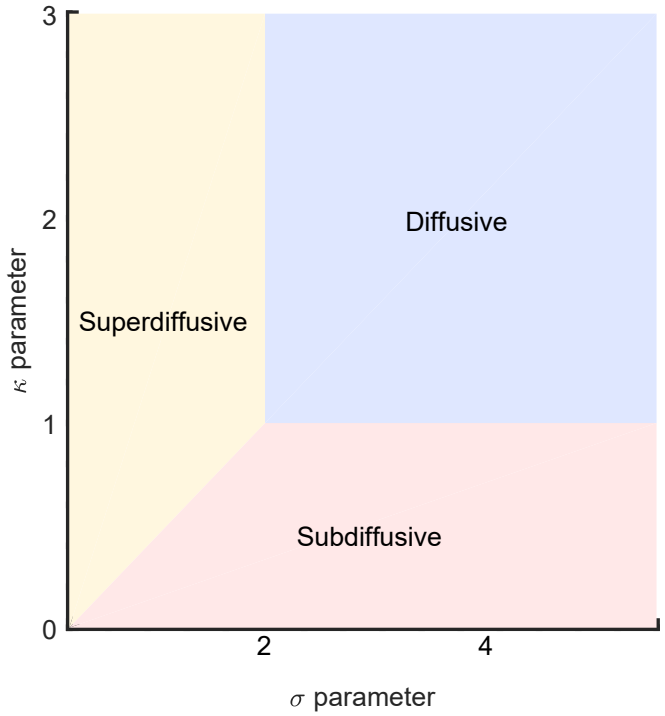

Fig. 2.7 Phase diagram distinguishing the three diffusion regimes according to the σ and κ parameters.

Anomalous diffusion is not only observed for light but is, in fact, ubiquitous in nature: for instance, superdiffusion is typical of predator search pattern [63] while subdiffusion has been linked to cytoplasmatic crowding [64].

In the field of photonics, anomalous diffusion has been predicted and measured in carefully engineered materials in which the fractal nature of the scattering medium introduces a heavy-tailed distribution of step lengths [65, 66]. Here, the dependence of the total transmission, T, on the sample thickness, L in Equation 2.46 has to be corrected to account for the anomaly so that [65]

$$T(L,\lambda) \simeq \frac{1}{1+AL^{\alpha/2}}, \tag{2.51}$$

where α is the parameter describing the diffusion regime (*i.e.* it is related to γ so that $\alpha = 2$ for diffusive systems and $\alpha \neq 2$ for anomalous ones) and A is a constant accounting for the absorption length l_A and extrapolation length z_e. The full derivation can be found in [67].

When α = 1/2, the superdiffusive behaviour is known as *Lévy flight* [68]. In particular, the light transport mechanism described in [65, 66] shows a Lévy flight behaviour due to the density fluctuations in the distribution of the scatterers. Where the scatterer density is high, light performs a large number of short steps; in contrast, where the scattering density is low, light propagates in long "jumps".

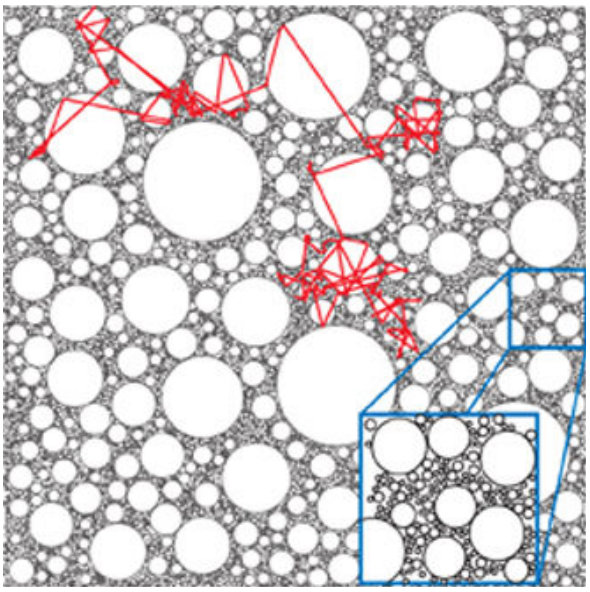

Fig. 2.8 A diagram representative of the photonic glass used in [65] to produce a Levy flight (in red) for light. Reproduced from [65] with permission.

To experimentally obtain such effect for light transport, a material composed by transparent glass spheres embedded in a scattering medium (constituted by an acrylate polymer and titania powder, TiO_2) was prepared. The spheres were matched in refractive index the polymeric portion of the material so that only the TiO_2 particles would act as scatterers.

Light progressed in short, random steps in the scattering medium whereas it propagated ballistically through the spheres (Figure 2.8). Hence, the sole purpose of the spheres was to modify the scatterers' density.

By tuning the extent of the density fluctuations (*i.e.* by varying the amount and size of the spheres) it was possible to introduce very long jumps so that the step distribution was skewed and the light transport could be approximated to a Lévy flight. Furthermore, the size distribution of the sphere's diameters was chosen to be scale-invariant to avoid the introduction a characteristic scattering distance.

This explanation has been, however, criticised in [69] where it was argued that a system can be normally diffusive even if the step-length distribution is non-Gaussian as long as the steps are not independent. This latter argument was also supported by earlier calculations in [70].

To unravel the cause of the disagreement, one has to refer back to the difference between *annealed* and *quenched* disordered systems. In annealed systems, like those presented so far, the steps between each scattering event are assumed to be completely independent from each other (this is why these structures also known as "memoryless"). In contrast, quenched systems are characterised by the presence of certain degree of correlation between the steps so that one cannot assume that the steps are independent from each other.

For example, in the case of the Lévy glass described here, it is reasonable to predict that light is likely to be "trapped" in the transparent spheres and be scattered back and forth inside the spheres before re-entering the embedding medium [71]. A light path as such contributes less to the average square displacement of the photons as it explores a smaller volume than it would have if it had not been trapped.

In the specific case of [65], it has been shown that the steps do not show any correlation and thus the superdiffusive approximation is an appropriate description [72] but there is general consensus that quenched disorder strongly affects the transport [73].

In Chapter 8, a novel cellulose-based superdiffusive system is described in which the anomaly is introduced by the size distribution of the scattering centres and their anisotropy in the spatial distribution. To date, no subdiffusive systems have been reported for light, even though preliminary calculations have shown their potential [74].

2.3.4 Anderson localisation

There are many analogies between the propagation of light in a disordered medium and the motion of electrons in a solid: both are scattered by the inhomogeneities in the structure as if they were particles and can interfere with each other as waves so that the same mathematical treatment can be applied to both [75].

Historically, the exploration of the disorder-induced phenomena began in the field of electronics in the late 1950s. The main question was whether the scattering mean free path l_s decreases indefinitely with increasing disorder or whether it reaches a minimum value [76]. P. W. Anderson was the first to demonstrate that, beyond a critical amount of disorder, the diffusion of the electrons comes to a halt [75]. Intuitively, this can be explained by l_s of the electrons becoming smaller than their de Broglie wavelength, resulting in the complete suppression of the diffusion current. The effect has later been experimentally proven [77], setting the basis for the investigation of the so-called *minimum conductivity*.

The idea that localisation could also be observed for classical waves started to emerge thirty years later. Both [78, 79] and [80] theorised that the same concepts should apply to the propagation of light through disordered media, predicting that photon localisation would be achieved for a material in which $kl_s \leq 1$, where k is the photon wavevector.

Localisation of light can be seen as a consequence of constructive interference [81]. A random light path that returns to the initial point can be followed in two opposite directions. Having acquired the same phase difference, the two waves will interfere constructively at the source location. This implies that there is a higher probability of the wave going back to the origin. As l_s decreases, the likelihood of observing such loops increases, eventually making it impossible for photons to "escape" the structure. In other words, light is spatially localised.

More quantitatively, in a localised regime the transmission through a medium decreases exponentially rather than linearly with the thickness of the sample [76]. At the critical point of transition between the two regimes, the transmission is predicted to have an inverse quadratic dependence [75].

Photonic systems offer various advantages with respect to electronic ones for observing Anderson localisation [76]. First of all, photons do not interact with each other and are facile to control at room temperature. Furthermore, while for electrons one can only directly monitor the conductance, there are a number of quantities that can be measured for photons in addition to the transmittance (*e.g.* amplitude, phase, time-of-flight, etc) with a higher degree of control over the polarisation states and angular response.

Fabricating a material where localisation can be observed poses three major challenges [80]. Firstly, to achieve strong scattering, it is necessary to increase the density of the scatterers. However, beyond a 50% fraction, the photons will be scattered by the cavities rather than the particles [82]. Secondly, unlike electrons, photons have a small scattering cross-section for long wavelengths due to the weaker Rayleigh scattering [76]. Lastly, localisation must not be confused with absorption. Materials with high refractive indices and low absorption can be chosen, but only careful characterisation of the medium can confirm that the regime of localisation has been achieved. In fact, reports of observation of Anderson

localisation (*e.g.* [81] for a two-dimensional GaAs powder) are often put into question by the scientific community due to the unconvincing absorption measurements [83]. To date, the only observation of localisation in a three-dimensional material [84] has also been challenged [85].

Achieving light localisation would not only unequivocally prove that Anderson's conjecture is valid, but it would also have useful applications for random lasing and quantum information processing [86].

One of the possible strategies to overcome the experimental issues mentioned above is the optimisation of the geometry of the disordered structure combined with a material of appropriately high refractive index. In Chapter 7, a novel method based on exploiting the white beetle's three-dimensional scattering network is shown to deliver promising results in the visible and infra-red wavelengths. Based on the finding that fibrillar networks allow strong scattering in low refractive index-materials, a bioinspired cellulose-based material is developed for industrial applications such as white coatings and paints (see Chapter 8).

2.3.5 Experimental estimation of the scattering mean free path in the diffusion approximation

The scattering mean free path is a key parameter impacting the performance of scattering media [87] independently from their thickness, filling fraction, and refractive index [88]: for long scattering mean free paths, light propagates almost undeflected through a slab of thickness L. Instead, a short scattering mean free path implies that light is scattered multiple times within the same thickness. Hence, the stronger a material scatters, the shorter its mean free path is.

Here, three methods for the experimental determination of l_s are presented: the first technique, the integrating sphere method, relies on the assumption that light intensity is a scalar quantity while the other two techniques, the speckle autocorrelation and the backscattering cone, take into account the vectorial nature of the photon propagation and interference. Photon interference requires having scatterers that are *frozen* at a fixed position in space. The latter condition is true even for materials that are not solid, as the time that photons spend in the medium ($\sim$ ps) is much shorter than the Brownian motion relaxation time ($\sim$ ms) [40].

The integrating sphere

The integrating sphere is a tool for the measurement of the total transmission (or reflection) of a material (see also Experimental Section 3.1.3). As it is possible to see from Equation 2.46, the mean free path can be estimated from the total transmission and thickness of a

sample [81]. However, because any error in the estimation of T, z_e, or L can lead to a large uncertainty in the value of l_s, it is customary to measure these quantities for various values of the thickness and perform a curve fit of T versus L to estimate l_s. To improve the quality of the fit, the condition $T_{(L=0)} = 1$ is imposed, as one expects complete transmission for zero thickness. Figure 2.9 shows an example of such procedure for a scattering material made of polymethyl methacrylate (PMMA) which is nanostructured as to enhance scattering[1].

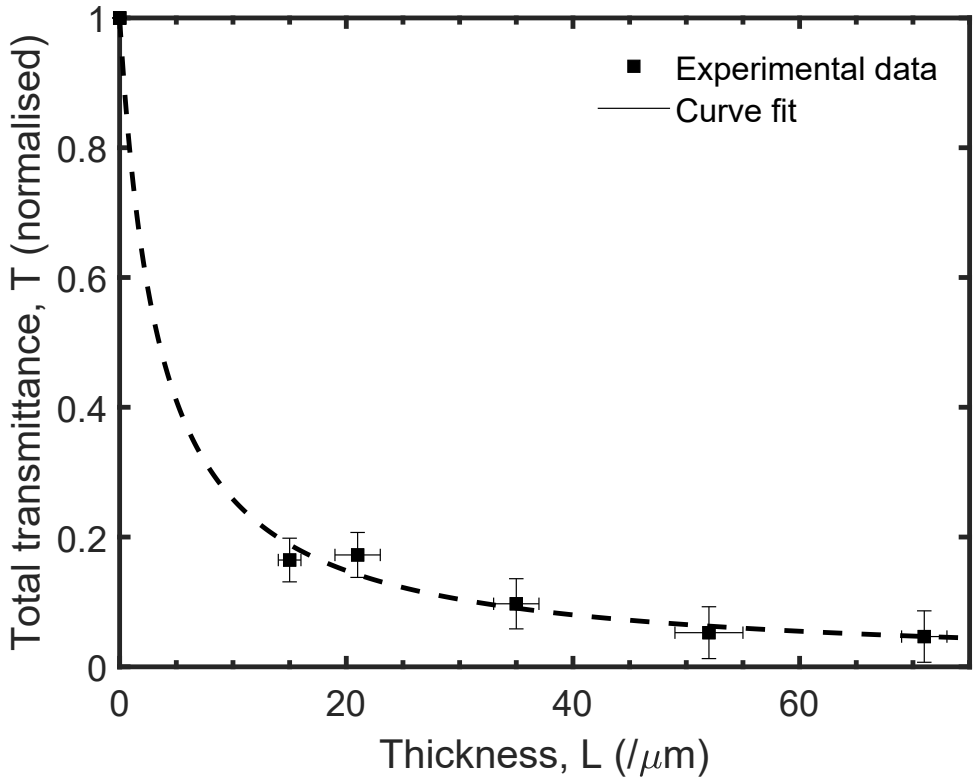

Fig. 2.9 Least-square fitting (black line, Equation 2.46) of the experimentally measured total transmission T (black markers) through various slabs of nano-patterned PMMA of thickness L. The fit satisfies the condition that for null thickness the transmittance is unity. From the curve fitting it is possible to infer that $l_s = (2.6 \pm 0.2)\ \mu$m for an estimated $z_e = \frac{2}{3} l_s$ given a filling fraction of 61% PMMA versus air ($n_{PMMA} \sim 1.54$ and $n_{air} = 1.00$).

Speckle autocorrelation

In absence of absorption, light undergoing multiple scattering collides elastically with the scattering elements. Therefore, the scattered waves must have a constant relative phase

[1]This work has been accepted for publication as: Syurik', J., Jacucci' G., Onelli, O. D., Vignolini, S., & Hölscher, H. Bio-inspired highly scattering networks *via* polymer phase separation. Advanced Functional Materials (2018). 'These authors have contributed equally to the work.

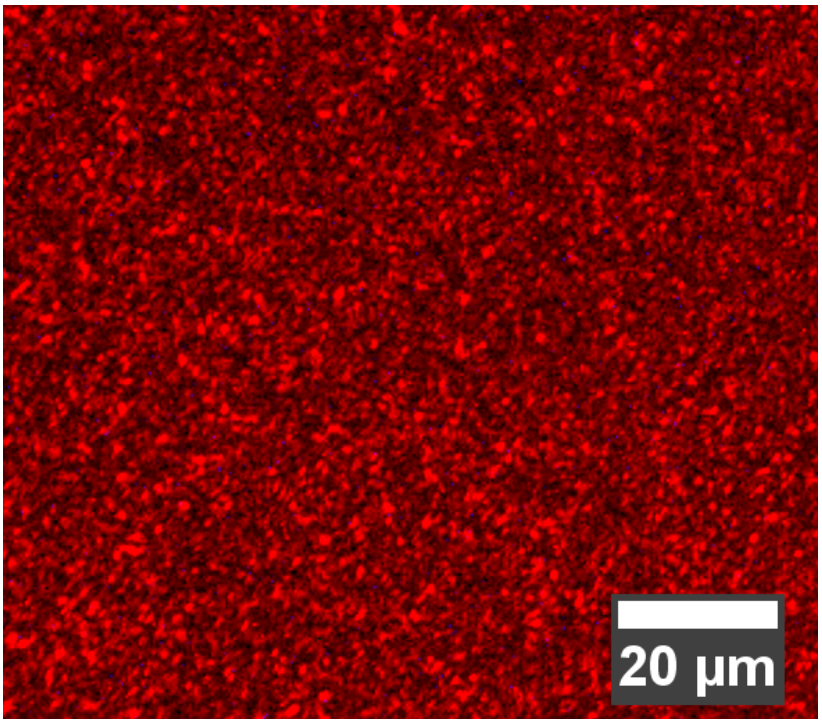

Fig. 2.10 A typical speckle pattern produced by shining laser light on a sheet of common paper.

difference determined by the optical path length between the field at each single scatterer and at the point of observation. It is thus possible to deduce that different scattering paths can interfere coherently with each other as the phase is not lost in the scattering process [89]. Such interference effects are not considered by the diffusion approximation described earlier in this chapter. Therefore, the theoretical framework needs to be expanded to include them.

The most common manifestation of this interference phenomenon is the speckle: a static granular pattern which forms on the surface of a diffusive medium when illuminated by a coherent light source. Speckles are most conspicuous when using laser light due to its high spatial coherence. In fact, one of the simplest methods for observing speckles is shining a laser beam on a rough surface such as a wall or on a piece of paper [90]: the laser's coherence length is much greater than the height of the surface features so that scattered wavefronts differ by a constant relative phase and can thus interfere with each other. It is, however, also possible to observe multicoloured speckles when sunlight impinges on a grainy surface. In fact, when the sky is clear, the sunlight spatial coherence can exceed 50 μm [91].

Due to its random nature, the intensity of the speckle pattern does not appear to be immediately related to the original object [92]. However, speckle patterns contain correlations that can be exploited to gain insight into the nature of the diffusive medium [93]. The speckle grain size in the far-field, h, is found to depend only on the distance of observation, u and of

the diameter of the illuminated area, D, according to the following relation [89]:

$$h = \frac{2.4\lambda u}{D}. \tag{2.52}$$

This is a consequence of the fact that the speckle grain is ultimately determined by the Airy disk diameter of the system [94]. Interestingly, the correlation between the patterns can encode further information.

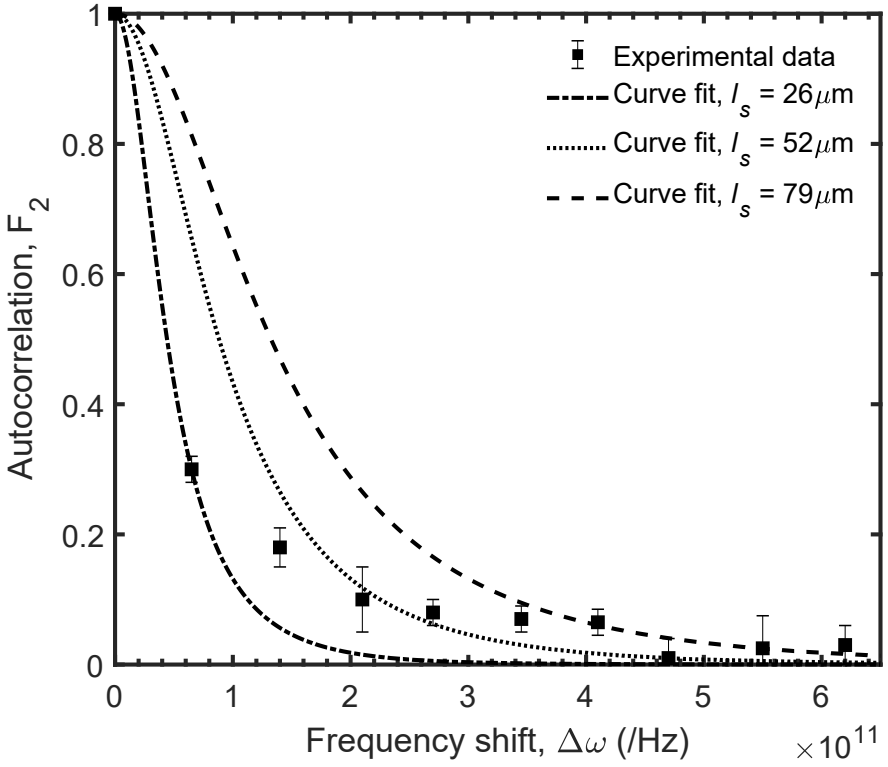

Fig. 2.11 Autocorrelation function: comparison between experimental data and the theoretical fits (Equation 2.54). The sample is common paper (thickness $\sim$400 μm), whose l_t is known to be around 25 μm [14]. From the curve fit, it is possible to estimate that $l_s = (52 \pm 26)$ μm. The large uncertainty is most probably due to the weak scattering properties of paper.

One of the most useful pieces of information that can be extracted from the speckle patterns and their correlation is the scattering mean free path. It has been shown that diffuse wave transport can sustain both short- and long-range correlations [95]. In particular, three types of correlations have been calculated for short-, long-, and infinite-range; they are known in the literature as $C^{(1)}$-, $C^{(2)}$-, and $C^{(3)}$-type correlations, respectively [96].

$C^{(1)}$ is a Gaussian statistics approximation for the field amplitude [97], as calculated in [98] and experimentally measured in [99, 100]. In the diffusive regime, $C^{(1)}$-type correlations dominate and the average size of a speckle spot is determined by this short-range interaction [101].

$C^{(2)}$, and $C^{(3)}$ are non-Gaussian correlations that decay on considerably larger scales. In particular, $C^{(3)}$ refers to those correlations that arise from the ensemble average of all transmission paths (or "channels") and can therefore be measured by total transmission measurements [95].

The focus in this work is on $C^{(2)}$-type correlations as these are key to estimate l_s. As calculated in [102] for a slab of thickness L with N number of transmitted modes,

$$C^{(2)} = (l_s/9NL)F_2(\Delta\omega, L), \tag{2.53}$$

with

$$F_2 = \frac{3}{2}x^{-1}\frac{\sinh(2x)-\sin(2x)}{\cosh(2x)-\cos(2x)}, \tag{2.54}$$

where $x = (\Delta\omega/D)^{1/2}L$ and $D = vl_s/3$ ($\Delta\omega$ being the frequency shift).

The first experimental confirmation of the shape of the function F_2 proved that the long-correlation function decays as $(\Delta\omega)^{1/2}$ and that its full width at half maximum is proportional to L^{-2} can be found in [95]. This work paves the way towards new techniques for imaging through turbid media [103]: if the shape of F_2 is known, it is possible to infer l_s *via* curve fitting (for a slab of known thickness) hence allowing spatial mapping of the scattering properties of the material, being it a colloidal suspension or a biological tissue [36]. In Chapter 7 an experimental set-up for the measurement of l_s is described.

In Figure 2.11 an example of such estimation technique is shown, with emphasis on the dramatic effect that varying l_s has on the curve shape. It can be noticed that the fit is not very satisfactory: this can be ascribed to two factors. First of all, the scattering in a medium such as white paper is weak and probably not able to sustain long-range correlations. Secondly, the experimental error bars are derived from the standard deviation of the speckle image autocorrelation (calculated using MATLAB). However, additional factors influence the uncertainty in the fitting, such as the error in the slab thickness measurement and the error in its refractive index.

The backscattering cone

One of the most solid demonstrations of the persistence of interference phenomena among waves that undergo multiple scattering is the coherent backscattering cone (also known

as "weak localisation") [104]. In contrast to the speckle pattern described above, weak localisation is an effect where the intensity of the light reflected in the backscattered direction is enhanced with respect to the other directions. This is a consequence of the interference between direct and reverse paths in the direction of illumination [105].

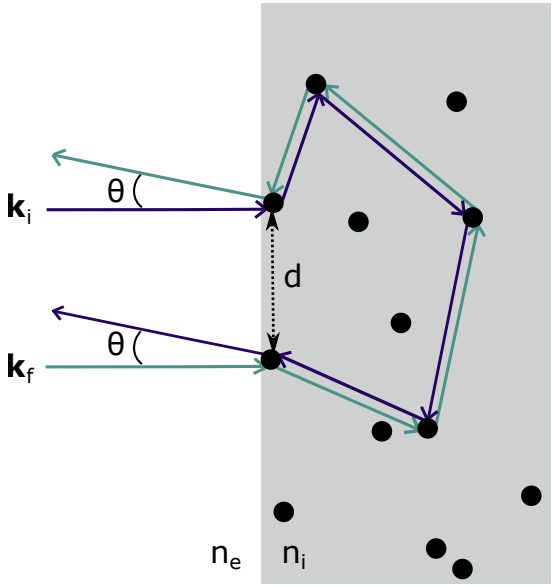

Fig. 2.12 Schematic diagram showing how the two counter-propagating paths give rise to interference as θ tends to zero.

In particular, the intensity I at angular position (θ,ϕ) due to the interference between many two-wave interference patterns can be written as [104]

$$I(\theta,\phi) \quad = \quad I_0(1+\zeta\cos(\mathbf{d}\cdot\Delta\mathbf{k})), \tag{2.55}$$

where I_0 is the intensity neglecting interactions, ζ is the contrast difference between constructive and destructive interference, $\mathbf{d}$ is the distance between the entry/exit positions (Figure 2.12), and $\Delta\mathbf{k}$ is defined as follows:

$$\Delta\mathbf{k} \quad = \quad \mathbf{k}_f - \mathbf{k}_i, \tag{2.56}$$

where, *e.g.* for normal incidence,

$$\mathbf{k}_i \quad = \quad (0,0,k), \tag{2.57}$$

$$\mathbf{k}_f \quad = \quad k(\sin\theta\cos\phi, \sin\theta\sin\phi, \cos\theta). \tag{2.58}$$

Consequently, the waves interfere with maximum intensity at $\theta = 0$, as long as reciprocity is preserved (*i.e.* both paths are exactly the same, Figure 2.12). The phase difference, $\Delta\phi$, between the two paths is therefore

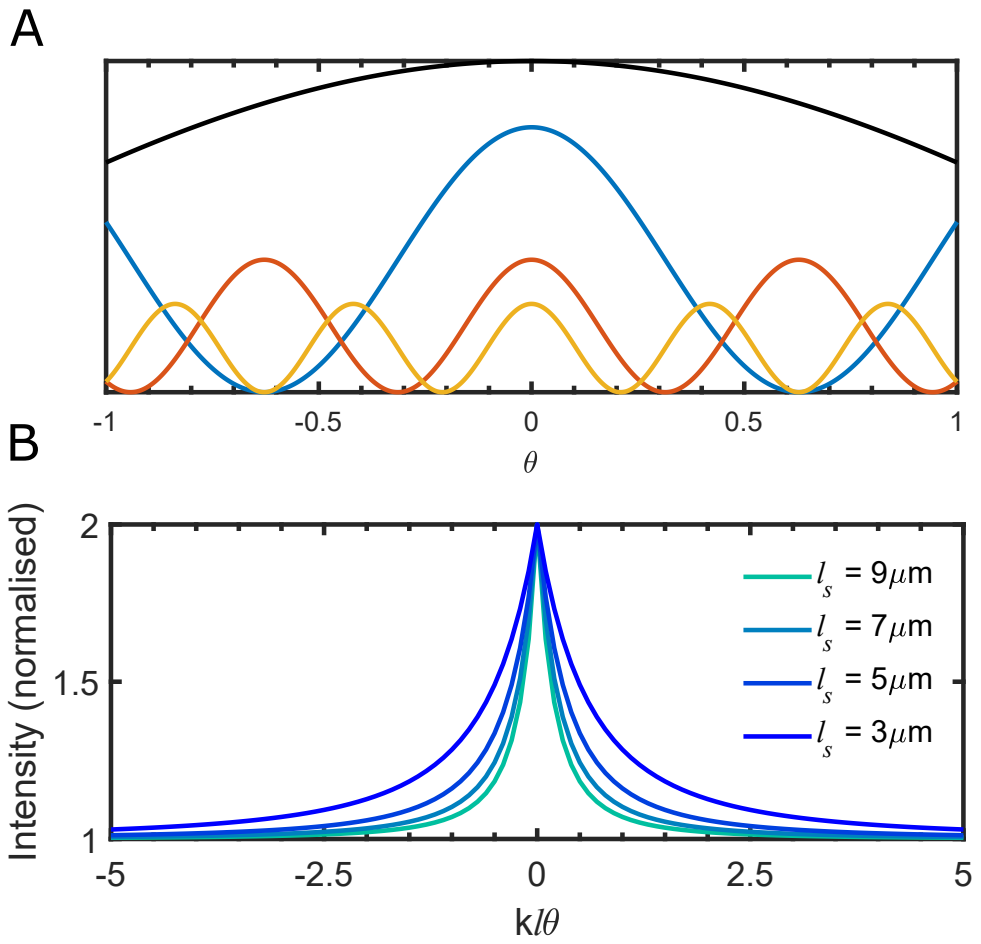

Fig. 2.13 A: the backscattering cone originates from the pair-wise interference of many waves that are in phase at $\theta = 0$. The wider curve corresponds to the shorter paths and vice versa. B: the width of the cone increases with decreasing scattering mean free path. The equation for generating the plot is reported in [106].

$$\Delta\phi \quad = \quad \frac{2\pi}{\lambda}(\mathbf{d}\cdot\Delta\mathbf{k}), \tag{2.59}$$

which, in the limit of small θ can be approximated to

$$\Delta\phi \quad \approx \quad \frac{2\pi}{\lambda} \mid \mathbf{r}_N - \mathbf{r}_i \mid . \tag{2.60}$$

where $\mid \mathbf{r}_N - \mathbf{r}_i \mid$ is the separation between the first scattering event at position $\mathbf{r}_i$ and the last one at $\mathbf{r}_N$.

$\mid \mathbf{r}_N - \mathbf{r}_i \mid$ represents the mean separation between the first and last scattering event and it is roughly of the order of the transport mean free path l_t so that

$$\Delta\phi \approx \frac{2\pi}{\lambda}\theta l_t. \tag{2.61}$$

It can be demonstrated that the width, W, of the backscattering cone can be approximated by [107, 108]

$$W(\theta) \simeq \frac{0.7}{2\pi}\frac{n_i}{n_e}\frac{\lambda_i}{l_t} = \frac{0.7}{2\pi}\frac{\lambda_e}{l_t}, \tag{2.62}$$

in which n_i is the effective refractive index of the sample and λ_i is the wavelength of light propagating in the sample; n_e is the refracting index of the medium between the illumination source and λ_e is the wavelength of the incident light.

This expression can be intuitively explained as follows:

- $\frac{n_e}{n_i}$ accounts for the light refraction at the sample interface;
- the factor 0.7 arises from the ensemble average over many scattering order contributions - its value is close to unity as double scattering dominates;
- the shape of the cone at the vertex is primarily determined by the longer paths whereas the shape of the cone at large angles is mostly driven by the shorter paths.

The latter consideration implies that the shape of the coherent backscattering depends on the diffusion parameter α. In [92, 109], it is shown that when α is decreased, the top of the cone is sharper as its shape is primarily dictated by the longer paths which are more abundant in superdiffusive systems. Similarly, the tails of the cone decrease more slowly as they stem out from the interaction between shorter paths.

The expected intensity of the coherent backscattering, I_{coh}, with respect to the incoherent background, I_{inc}, can be estimated considering that if two waves of equal amplitude A interact coherently, they sum as follows [110]

$$I_{coh} = |A + A|^2 = 4A^2, \tag{2.63}$$

whereas incoherent waves sum as

$$I_{inc} = |A|^2 + |A|^2 = 2A^2. \tag{2.64}$$

Hence, the coherent backscattering intensity is theoretically predicted to be twice the background intensity.

Even though the enhancement is conspicuous, two main experimental issues prevented the observation of this effect until the 1980s when it was first reported in [111, 112]. The first

limitation is that the backscattering direction coincides, by definition, with the direction of illumination. Hence, the light detector for collecting the backscattered intensity "blinds" the light source. The second limitation is that the width of the cone is typically of the order of tens or hundreds milliradians so that a very high angular resolution is needed to distinguish the shape of the cone.

Ever since its discovery, measurements of the backscattering cone have been used to estimate the scattering mean free path of materials [113]. Due to the wavelength dependence of the cone's width, it has been shown that multi-wavelength, broadband measurements are possible [114, 115] as well as observation of the phenomenon in frequencies other than the visible, giving information about *e.g.* the chemical composition of the icy moons of Jupiter as predicted by the measured scattering cross-section [116].

Drawbacks

Estimating the scattering mean free path experimentally is crucial to evaluate and compare the scattering efficiency of materials. However, measuring l_s is a non-trivial problem and even though a few techniques are available they all have disadvantages: the integrating sphere method can be considered the most straightforward and it applies to both anomalous and standard diffusive systems. However, it relies on having at least 3-5 samples that differ in thickness, spanning at least one order of magnitude, which may not be feasible for some materials; the backscattering cone technique is independent of thickness but it is notoriously difficult due to the fine alignment needed and the troublesome normalisation. Furthermore, the sample needs to be sufficiently thick so that a significant number of scattering events can occur and build up the interference pattern (typically, at least ten times thicker than the scattering mean free path); finally, the speckle autocorrelation method requires having a tuneable laser whose sensitivity is such that the autocorrelation function can be traced accurately over the required frequency range and a suitable CCD camera for the acquisition of low-intensity images.

Chapter 3

Experimental materials and methods

To understand and model structurally coloured materials, it is often crucial to image the three-dimensional architecture of the photonic structure. Due to the nanoscopic size of the features, electron microscopy is generally necessary to resolve the structures of interest. At the same time, the microscopic arrangement of the architecture is often relevant in building up the overall, macroscopic optical properties of a material. Hence, optical microscopy is used to extract information at a larger scale.

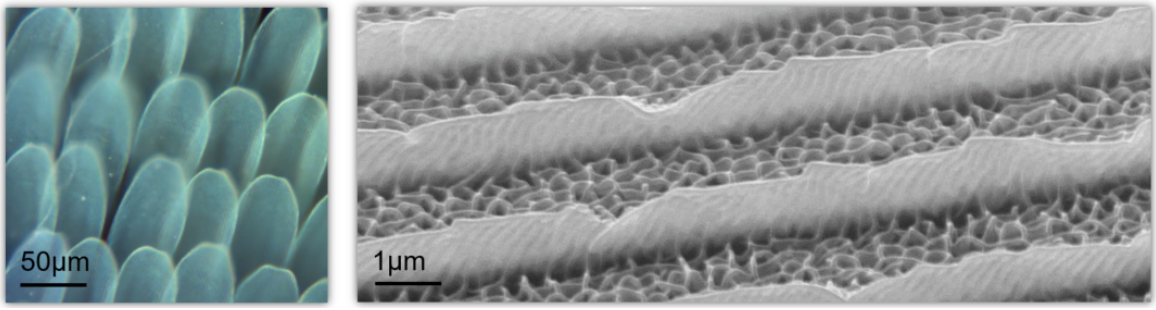

Fig. 3.1 *P. nireus* butterfly. On the left, an optical micrograph of the wing's blue scales reveals the presence of longitudinal ridges. On the right, a SEM image of a single scale: here it is possible to appreciate the nanostructures in-between the ridges.

3.1 Optical measurements

3.1.1 Optical microscopy

A customised Zeiss Axio microscope is used to perform optical microscopy. Illumination is the most important factor affecting the quality of the images. Hence, before every measurement, the microscope is aligned to achieve optimal Köhler illumination.

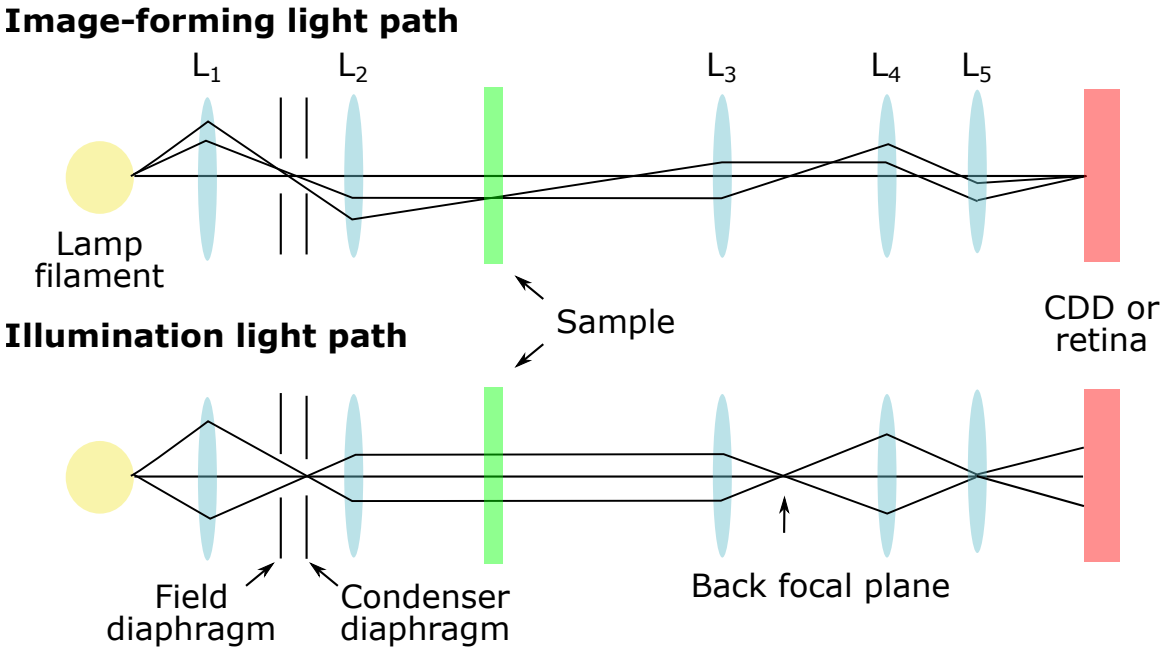

Fig. 3.2 Schematics of a Köhler microscope set up (transmission configuration). In the image-forming light path, the specimen image is focused at the eyepoint (or at on CCD sensor). In the illumination path the image of the lamp filament is defocussed at the sample plane as well as at the observation position to obtain an even illumination.

Köhler illumination consists of having two sets of conjugated planes in the light path (Figure 3.2): the first one, known as *image-forming light path*, is constituted by the field diaphragm, the focused specimen, and the retina of the observer or the camera sensor plane; the second one, known as *illumination light path*, includes the lamp filament, the condenser diaphragm, the back focal plane of the objective, and the eyepoint (located a few centimetres above the eyepiece). In this work, a charged-couple device (CCD) camera (IDS UI-3580LE) is used to record the images.

Alignment of the conjugated planes is critical not only to achieve artefacts-free images but also to be able to control the lighting conditions. This can be achieved by changing the field diaphragm and the condenser diaphragm aperture.

The field diaphragm controls the the field of view of the objective. This mostly affects the image quality. Typically, optimal results are obtained when the field of view is 2/3 of the total image as this discards the peripheral areas of the image which are most likely to be affected by distortions.

Similarly, the condenser diaphragm controls the angular width of the illumination light beam which is quantified by a dimensionless number, the numerical aperture (NA). The nominal numerical aperture of the objectives is achieved only if the condenser diaphragm is

completely open. The correct management of the numerical aperture is very important when characterising structurally coloured samples: by changing the angular range of illumination, the appearance of the structures imaged changes drastically.

For example, when the 20X and 50X objectives are mounted on the microscope their numerical aperture (*NA*) are 0.6 and 0.95 respectively. As a consequence, the half-angle θ of the maximum cone of light that can enter or exit the lens is 40° for the 20X objective and 71° for the 50X objective as calculated according to [117]

$$NA = nsin\theta, \tag{3.1}$$

where *n* is the refractive index of the medium between the objective and the sample (here, air. Figure 3.3). Hence, the light scattered from highly scattering specimens is collected using the 50X objective as a broader half-angle guarantees the collection of a greater proportion of the light scattered laterally.

3.1.2 Optical spectroscopy

Spectroscopy in the visible range allows to quantify the optical properties of a material. In particular, its reflectivity and transmittivity can be measured as compared to standard materials of reference. A customised set-up for spectra collection is used to characterise the reflectivity of the samples. By coupling it to the optical microscope *via* optical fibres, it is possible to probe small areas of the samples (down to 1 μm in diameter, depending on the lenses used for the coupling).

Using the Köhler set-up described in Section 3.1.1, it is possible to split the signal from the sample so that half of the beam is collected by the camera and half is coupled into a spectrometer (AvaSpec-HS2048, Avantes) *via* an optical fibre (50-600 μm core, Avantes). This allows the acquisition of spectra from specific areas of the sample.

A silver mirror (Thorlabs, PF10-03-P01) is generally used to normalise the spectra obtained from reflective samples. In contrast, the spectra of strongly scattering samples are normalised against a standard white diffuser (LabSphere USRS-99-010) whose angular profile is Lambertian in order to avoid aberration. The latter can also be used as normalisation when performing near-UV measurement: the reflectance of silver mirrors falls sharply below 400 nm while diffusers can allow measurements for wavelengths as short as 300 nm.

Because the collection NA of the spectrometer is the same of the microscope, it is important to point out that the spectra vary according to the NA used. Hence, if the spectra are utilised for theoretical modelling using techniques such as the transfer matrix method

(see Chapter 2.2), it is crucial to match the angles over which the simulation is iterated with the numerical aperture of the experimental set-up to obtain comparable results. In fact, if a large numerical aperture is used for the collection of the signal, the spectra will be composed of multiple peaks leading to spectral broadening.

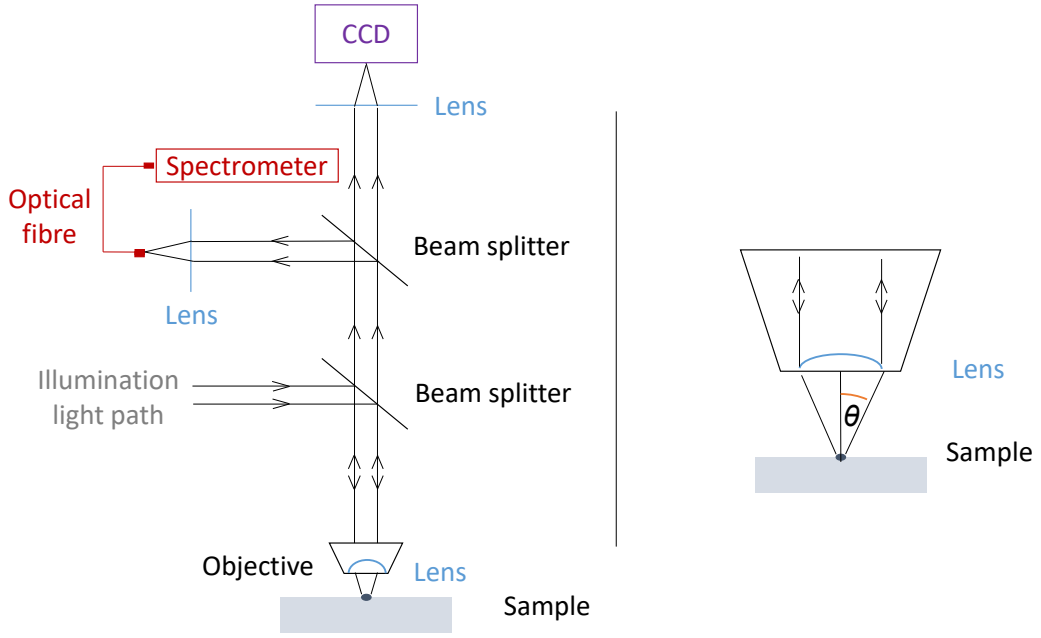

Fig. 3.3 On the left: the customised set-up for optical microscopy and spectroscopy used to characterise the samples. The beam splitters are placed at the conjugated planes to preserve the Köhler illumination condition. On the right: close-up of the objective and sample, highlighting the collection half-angle θ.

The Double-ended fibre

The Double-ended fibre (or Bifurcated fibre-optic probe, here Ocean Optics P600-1-UV-VIS. NA = 0.22) is a versatile device for the collection of spectra from cm-sized areas. It consists of an optical fibre where six light guides are placed around a core guide: the outer guides deliver light from a light source (Xenon lamp Ocean Optics HPX-2000) to the sample while the inner one collects the signal from the sample and transmits it to a spectrometer (Avantes AvaSpec-HS2048).

The wavelength range of the instrument principally depends on the characteristics of the fibre. As a consequence, it is possible to carry out measurements at short wavelengths ($\sim$ 250 - 300 nm) which are, instead, difficult to perform with a microspectroscopy set-up as the one described above due to poor performance of the optical components in the near UV.

Another advantage of the Double-ended fibre is that the area of collection is larger than in the case of microspectroscopy (mm *versus* μm). Reflectivity from a macroscopic sample can be a more relevant quantity to measure if one is interested in the overall appearance of a material.

However, a Double-ended fibre reading tends to be less reliable and more prone to error than a microscopic measurement. This is due to the difficulty of focusing the fibre on the sample: the focal point of the fibre is determined by its numerical aperture so if the gap between the fibre end and the sample is varied even slightly, the fluctuations in the signal can be very significant. Hence, it is important to mount the reference material (*e.g.* a mirror) and the sample at exactly the same distance from the fibre.

3.1.3 The integrating sphere

The integrating sphere is a widely used instrument to measure the total reflection and total transmittance of a material [118]. It consists of a hollow sphere whose internal surface is coated with a highly reflective material so that any impinging light is scattered in multiple directions and distributed equally in the volume. In this way, the directionality of the signal is lost, but the total intensity is retained. The signal is then measured by a spectrometer (see the diagram in Figure 3.4A).

There are two main advantages of using an integrating sphere. Firstly, the effective numerical aperture is very close to unity. As a consequence, the signal at wider angles is not discarded (this is in contrast to microscope measurements and Double-ended fibre acquisitions). Secondly, the coating material is very efficient over a wide wavelength range (300-1000 nm). The spectral range, however, is often limited by the light source used.

There are three different configurations in which the integrating sphere can be used, depending on the sample and information needed (Figure 3.4B-E) [119, 120]:

1. total transmission, TT: the sample is mounted at the illumination port, which is kept open to let in the sphere the light transmitted through the sample. This type of configuration is extremely useful to estimate the scattering mean free path of a material (see Chapter 2.3.1).

2. total reflection, TR: the sample is mounted outside the port which is opposite the illumination aperture. The reflected light is collected by the spectrometer. Typically, bafflers are placed inside the sphere so that light which has scattered only once (or twice) cannot be detected.

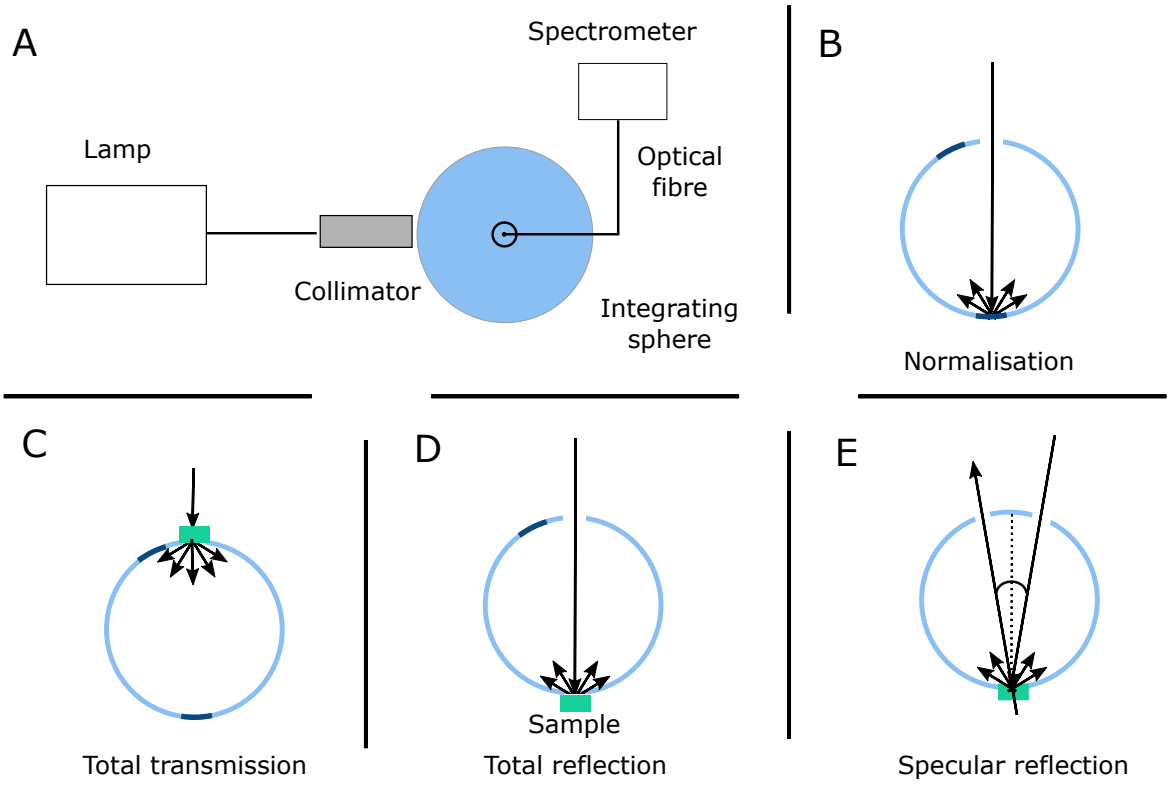

Fig. 3.4 A: the experimental set-up consists of a light source (Ocean Optics HPX-2000) coupled into an optical fibre (Thorlabs FC-UV100-2-SR) *via* a collimator (Thorlabs). The transmitted/reflected light is collected with the integrating sphere (Labsphere) and the signal is acquired by a spectrometer (Avantes HS2048). B: the intensity is normalised with respect to the closed integrating sphere. C: for a transmission measurement, the sample is mounted just outside the illumination port. D: total reflection measurement in which the sample is placed outside the port opposite to the light source. D: scattering measurement. Here, a third port is open to let out the specular reflection from the sample.

3. scattering, S: the system is set up as in 2 but the port which is diametrically opposite the sample is open so that the specular reflection, SR, exits the sphere and is not measured by the spectrometer.

Approaches $1-3$ together can provide useful information about the magnitude of the specular reflection with respect to the scattering from the sample and its absorption, A. In fact, it is possible to say that the total amount of light input is fractioned as

$$1 \quad = \quad T + SR + S + A, \tag{3.2}$$

so that, by subtraction, any of the quantities can be determined separately.

3.2 Electron microscopy

Electron microscopy has a resolving power which exceeds that of optical microscopes by a few orders of magnitude [121]. Such performance is achieved using a beam of electrons created by an electron gun as illumination source rather than light: the de Broglie wavelength of electrons is significantly shorter than that of photons so that the diffraction limit is of the order of tens of pm for electron microscopes as compared to the limit for optical microscopes which is around 200 nm [122].

Most microscopy principles apply to optical microscopes as well as electron ones. However, in optical microscopes the light beam is manipulated using glass lenses while in the case of electron microscopes the lenses are effectively substituted by magnets which can direct the flow of electrons towards the sample [123]. Another difference is that electron microscopes operate under *vacuum* while optical microscopes can be used in air- or in liquid-filled environments (*e.g.* oil immersion microscopes) [122]. This is due to the fact that the electrons are be scattered by the air molecules (or other media) and it would not be possible to obtain a focused beam.

One can distinguish two types of electron microscopes according to their operation mode: transmission electron microscopes (TEM) and scanning electron microscopes (SEM). Both machines use the interactions between the electron beam and the sample to infer information about the latter. In fact, when the electrons impinge on the specimen surface, they lose energy *via* a number of mechanism such as low-energy secondary electrons and high-energy backscattered electrons, heat, and light or X-ray emission. The information obtained with an electron microscope is a map of the intensity and type of the detected energy losses converted to an image. Typically, heat and light are not considered in electron microscopy which, instead, concentrates on the analysis of the other products.

In TEM, the electrons that are scattered (and diffracted) as the beam is transmitted through the specimen are used to reconstruct spatial information regarding the sample [124]. The latter needs to be transparent to electrons and is thus typically very thin (<200 nm).

In SEM, information about the specimen is reconstructed from the electrons that are generated or scattered from the surface of the sample [125].

The main difference between TEM and SEM is that the beam in the latter is more focused (up to 1 nm). Hence, the probe needs to "scan" the surface of the sample to map the entire field of view whereas TEM can analyse larger areas simultaneously.

Biological samples are notoriously difficult to image *via* electron microscopy: they are not conductive so the electron beam interacts with the specimens for a longer time. Even

at low beam voltages biological samples often suffer irremediable damages due to such extended exposure to high energy electrons.

Another shortcoming is caused by the fact that electron microscopes operate in *vacuum*: biological samples have to be dehydrated in order to prevent damage due to the rapid evaporation of water when the sample is placed under *vacuum*. This can be prevented by deep-freezing the sample beforehand or *via* fixation using resins.

Hence, sample preparation and optimisation of the parameters for imaging are of fundamental importance to achieve optimal results (see Appendix B for details on the sample preparation).

Focused ion beam

Focused ion beam (FIB) milling provides a reliable way of exposing the cross-section of a sample and, combined with SEM imaging, it allows the reconstruction of the full 3D volume from sequences of 2D images [126].

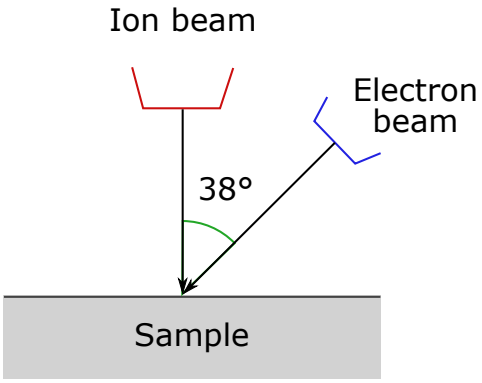

Fig. 3.5 In a FIB/SEM system the ion beam is normal to the surface of the specimen while the electron beam is tilted so that the angle between the two beams is 38°.

A FIB set-up functions very similarly to a SEM but the focused beam is constituted by ions rather than electrons. The most common type of ions used for this application is gallium ions (Ga^+) as these can be finely focused [127]. At low beam currents, the ions can be used for imaging while at high currents they can remove material from the sample with sub-micrometre precision [128].

FIB/SEM stations are set-ups where the ion and electron beam column can be used at the same time. As shown in Figure 3.5, the ion beam is typically normal to the surface of the specimen while the electron beam is at 52° to it - in this way the two beams do not impede

each other. The main application for the FIB/SEM set-up is known as "slice-and-view": as the two beams can be operated simultaneously, it is possible to slice the sample with the ion beam and image the section with the electron microscope.

FIB milling is carried out in three stages: first, the surroundings of the area of interest are cleared out using a high current. Then, a rough cut is made using a lower current and finally the cross-section is slowly cleared using a very low-intensity cross-section cut (known as *cleaning* cross-section). The machine used in the context of this thesis is a FEI Philips Dualbeam Quanta 3D system. The parameters used vary depending on the hardness of the sample and are summarised in Table B.1 in Appendix B.

For tomographies, the region of interest is coated with a 0.5 μm-thick Pt (platinum) using a micromanipulator. Slices of even thickness are cut with the ion beam and the surfaces exposed are imaged, to obtain a collection of sequential two-dimensional images that is later used to reconstruct the three-dimensional volume. A fiducial mark is placed in order to automate the image acquisition (iSpy software by FEI) and help with the later re-alignment of the images. Furthermore, the mark is used to determine *a posteriori* the thickness of the slices.

The three-dimensional volume is reconstructed using Avizo (software by FEI). First of all, the images are aligned and corrected for shear and tilt. Then, a median filter is applied in order to remove the noise. The stack of images is subsequently converted to binary using an interacting thresholding procedure. At this point it is possible to segment the volume and partition the features of interest. Each of these is labelled and their volume is calculated. From the partition and labelling, it is possible to extrapolate information about the structure (*e.g. radii*, filling fraction, etc.). To produce an animated visualisation of the dataset, a volume rendering is created from the images stack.

Chapter 4

Review: disordered photonics in nature

The ubiquity of colour-producing nano-structures in nature spans various groups of organisms, including: bacteria [129], protists [130], plants [18], and animals [10]. From one- to three-dimensional systems, the variety of colour-producing photonic mechanisms is tremendous, with structural colour known to play a key role in animal communication [131], mating [132], and camouflage [133] in a number of animals. These structures can be highly periodic (where long-range correlations between elements give rise to bright metallic colouration [134]), partially disordered (where short-range correlations allow matte, isotropic colour [12]), or completely random (with the absence of correlation between the scattering centres providing brilliant white reflectivity [135, 14]). Fossil evidence shows that structural colouration existed as long as 500 million years ago [8, 136, 137].

The past decades have seen increasing interest in biological photonics, especially as a source of inspiration for biomimetic devices and applications [138]. More recently, the attention of the scientific community has shifted from ordered to disordered structures [33] as it became apparent that most architectures deviate from perfect periodicity, on both short- and long-range length scales [19].

Recent advances in imaging techniques - in terms of resolution and field of view - and in computational techniques made it possible to access these complex systems and understand the interplay of order and disorder in living photonic structures [20].

Broadly speaking, the effects that disorder can introduce can be classified into four categories: broadband reflectance (as opposed to narrow-band responses), modulation of the angular response, polarisation effects, and polycrystallinity-related optical properties. In

this chapter[1] each phenomenon will be discussed in relation to recent examples from the literature.

4.1 Broadband optical response

4.1.1 Metallic appearance

In Chapter 2.2 the propagation of light through layered media has been discussed - showing how spectral broadening can occur as a consequence of a high refractive index difference between the layers and of the variation in the incident angle. Breaking the periodicity of the multilayers can also lead to a similar result, causing an intense metallic appearance.

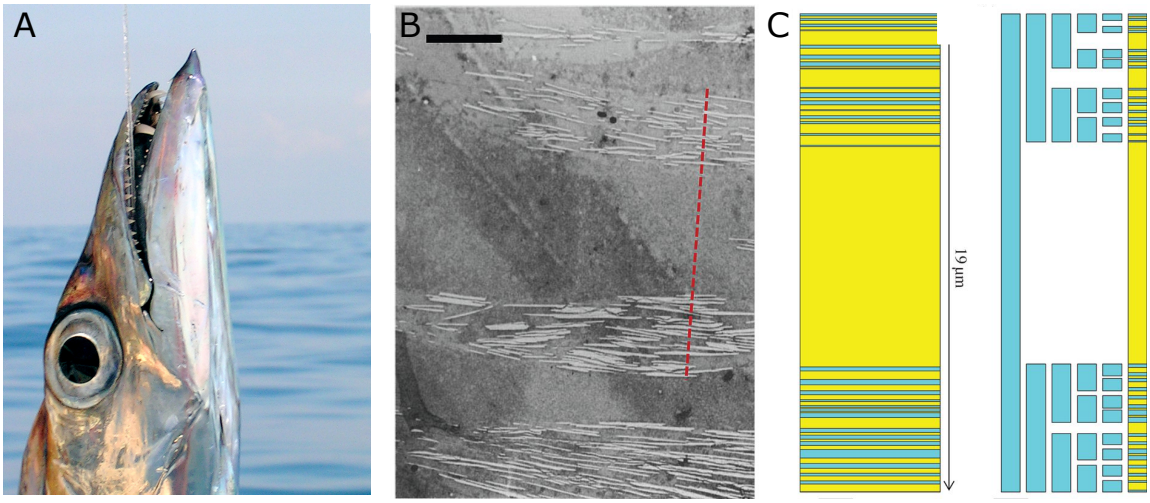

Fig. 4.1 A: *Lepidopus caudatus* photographed by Flavia Brandi on Flickr (licensed under CC BY-NC 2.0); B: cross-sectional TEM image of the fish's silver skin (scale bar: 5 μm); C: Five-stage fractal approximating the reflector, the guanine crystals are represented in blue and the cytoplasm in yellow. B and C are reproduced from [139] under CC BY 4.0.

The most commonly recurring metallic colouration in nature is the silver appearance of a number of pelagic mid-water fish (Figure 4.1A) such as *Clupea harengus* (Atlantic herring) and *Sardina pilchardus* (European sardine) [140]. Even though their colouration appears extremely conspicuous in air, underwater the silver reflection acts as a perfect mirror, reflecting the diffuse light from the fish skin [141]. This effect is achieved by having a multilayer reflector composed by anhydrous guanine crystals separated by cytoplasm where the spacing between crystals and the crystals' size varies significantly (Figure 4.1B)

[1]Parts of this chapter will be published as: Johansen, V. E., Onelli, O. D., Steiner, L. M., Vignolini, S. "Photonic structures in nature: from order to disorder". *Functional Surfaces in Biology III*. Edited by E. Gorb and S. Gorb. London: Springer, 2018

[142, 140]. This variability leads to a peak intensity that is lower than in the ideal case. As a consequence, the signal at wavelengths outside the main range of reflectivity is higher, which is more favourable for a silvery, broadband colouration [142].

Guanine/cytoplasm Bragg stacks can be found either in the fish's *stratum argenteum* (a sub-dermal layer of the skin) or in the inner surface of the scales. In the case of the family Trichiurus, no scales are present but a disordered multilayer has been imaged *via* TEM.

It was thought that the structure was completely random thus optimised for broadband reflectivity [143, 144]. However, it has recently been suggested that the layering follows a fractal geometry [139]. By computationally generating patterns, one can show that seemingly random layering can be replicated by having three or more fractal generators randomly spread throughout the crystal growth (Figure 4.1C). This implies that the system is not fully disordered: if the initial conditions are known, the final structure can be determined. The high degree of pattern variability would not be achievable in perfectly regular systems. Interestingly, this places the fish reflector in-between the completely deterministic and random extremes. It would be interesting to investigate experimentally how the guanine/cytoplasm multilayer forms and whether it, indeed, follows a Cantor bar generator during the development of the organism.

A different strategy for the production of golden and silver colouration is the "chirped" multilayer where layer thickness decreases with depth, reflecting shorter and shorter wavelengths of light so that the full spectrum can interact with the stack [144, 145]. This is the case in the silver *Chrysina chrysagyrea* and golden *Anoplognathus parvulus* beetles which exploit their colouration for camouflage in the dewy forest [146]. A similar structure has also been observed in the golden chrysalis of the butterfly *Euploea core* [144, 139]. In these cases, the structure is not periodic but it can be still considered "ordered" as the layering architecture follows a determined mathematical relation.

4.1.2 Whiteness

As discussed in Chapter 2.3, light propagating through a completely disordered structure is scattered multiple times and exits the medium in random directions, thus giving a white, diffuse colouration [33]. The three main factors that determine the efficiency of this phenomenon are:

1. the refractive index *ratio* between the propagation medium and the scattering centres;
2. the packing and density of the scatterers (or filling fraction);
3. the size and shape of the scatterers.

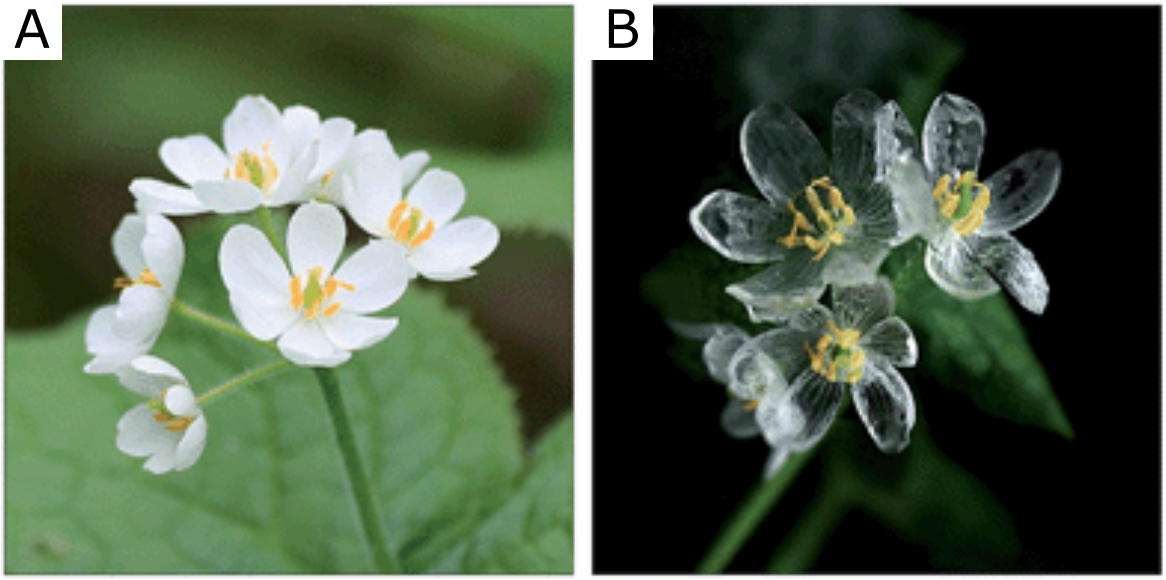

Fig. 4.2 Petals of *Diphylleia grayi* in sunlight (A) and in the rain (B). Reproduced from [147] with permission from The Royal Society of Chemistry.

The petals of the small herb *Diphylleia grayi* clearly exemplify the first point: the numerous *lacunae* in-between the cells on the petals are filled with air: the difference in refractive index between the two media causes light to be scattered, producing a white colouration [147]. However, if it rains, the air gaps fill with water, which has a refractive index very similar to the one of the cells. Therefore, the petals behave as a uniform medium and light can propagate almost undeflected, thus giving a transparent appearance (Figure 4.2).

Due to the limited range of available refractive indices in biological systems, natural scattering materials have evolved to optimise the medium's filling fraction. In the case of the white damselfly *Pseudolestes mirabilis* (Odonata) a two-dimensional random array of tightly packed waxy fibres has been observed to efficiently scatter light as a consequence of the nearly ideal packing of the elements [16].

Perhaps the most striking example of scattering optimisation is the white beetle genus *Cyphochilus* (Figure 7.1A). The scales covering the exoskeleton show a brilliant white colouration whilst only being 5-7 μm thick. This makes them the whitest natural material known to date. The discovery was first reported in 2007 [135], and it has been speculated that the white appearance helps the beetle camouflage amongst white *fungi* [14].

A number of research groups have tried to explain how the *Cyphochilus* achieves such performance given that the biological material involved has a low refractive index, which is not optimal for enhancing whiteness. In fact, the scales are made up of filaments of chitin,

a long chain polysaccharide with a refractive index around 1.55-1.56 [148]. This is much smaller than, for example, the refractive index of materials commonly used in industry to produce white paints such as titanium dioxide or zinc oxide whose refractive indices are well above 2 in the visible range [149, 150].

By comparing *Cyphochilus* scales to other white beetles whose scattering efficiency is lower (*Lepidiota stigma* and *Calothyrza margaritifera*), it can be observed that in all cases the filling fraction (*i.e.* the amount of chitin versus the amount of air) is optimised for scattering, but in *Cyphochilus* the scattering centres spacing and diameters are particularly adapted for minimising the mean free path and therefore the thickness of the scales [151].

Time-resolved measurements confirm that light is, indeed, scattered multiple times as it propagates through the scales [14]. The flux of photons through the scales is measured as a function of the time elapsed from the illumination of the sample. This shows a significant time delay as compared to the time expected for light propagating ballistically. The scattering mean free path is measured to be $\sim$1.47 μm, roughly one order of magnitude shorter than that of paper - a material of similar refractive index. A later work demonstrates that the anisotropy of the chitin rod distribution is also important in the optical response: the high filling fraction of the scales implies that some degree of angular correlation has to be introduced [152]. In fact, from SEM images it is possible to observe the anisotropy of the structure where the chitin filaments are mostly distributed with a planar orientation (for a more extended discussion see Chapter 7).

4.2 Design of the angular response

Disorder strongly affects the reflective properties of photonic structures. For example, by introducing disorder in a standard multilayer, it is possible to decrease the angular dependence of the peak wavelength. For example, in Figure 4.3C it is possible to see that the blue-shift of the peak wavelength at 40°, as compared to the central wavelength peak at 0°, for an ordered multilayer is about 90 nm while for a disordered one is roughly 50 nm. Furthermore, the width of the peak itself is changing from about 100 nm for the periodic case to more than 200 nm for the disordered one.

In nature it is possible to find a number of systems where disorder can both disrupt the otherwise sharp angular response - producing non-iridescent colours - or produce complex angular effects which could not be achieved *via* perfectly ordered structures. The following examples from the literature show the occurrence of such phenomena in biological photonic structures.

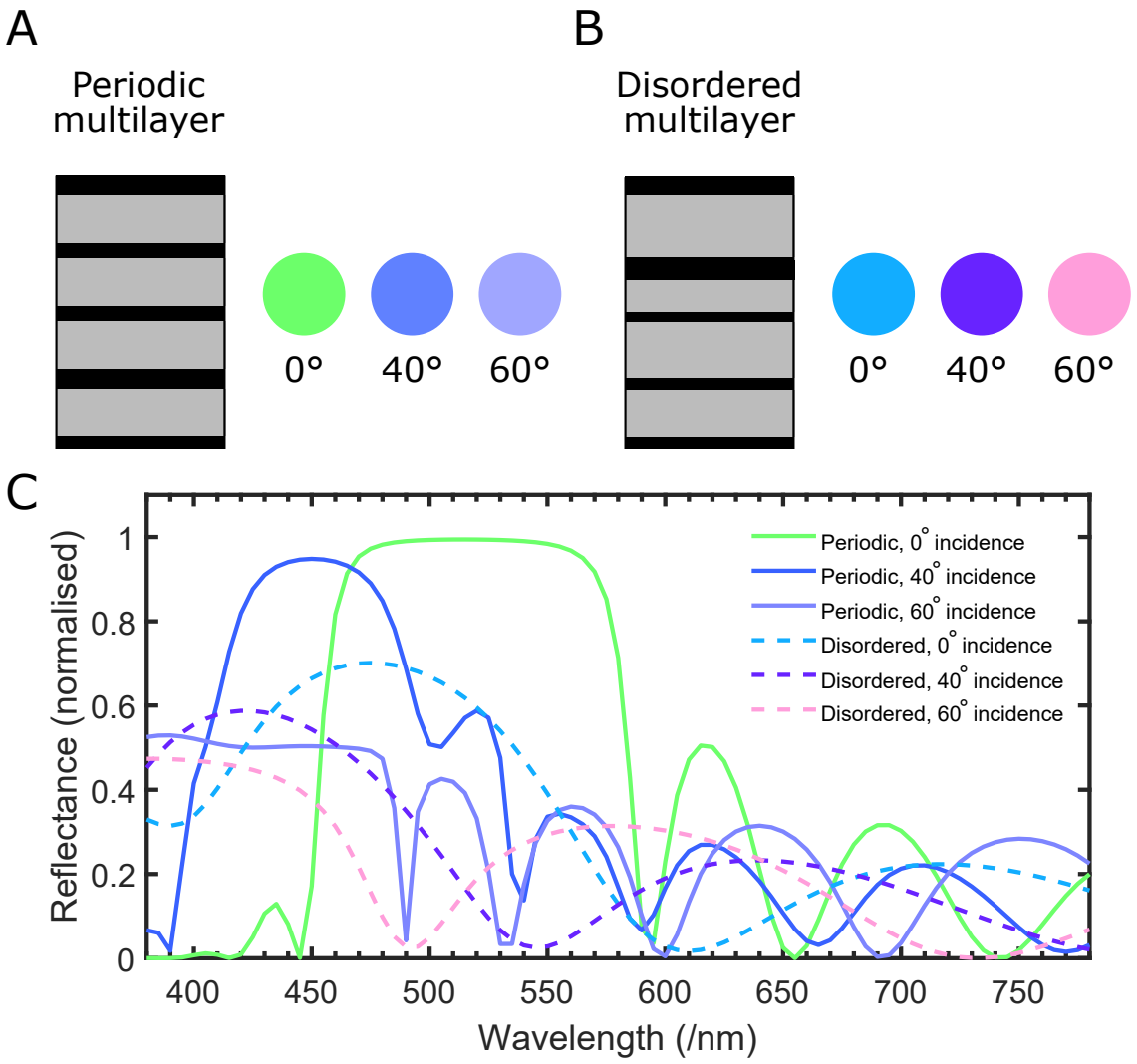

Fig. 4.3 A transfer-matrix method simulation is run for both an ordered (A, 10 layers with n equal to 1 and 1.6 and thickness 60 and 120 nm respectively) and a disordered multilayer (B, same n but aperiodic layer thickness going from 40 nm to 120 nm, 1 disorder realisation) using various angles of incidence: 0°, 40°, and 60°. In both cases the peak wavelength and width of the reflectance spectrum (C) depends on the angle. However, for the ordered multilayer the iridescence is more obvious than for the disordered system. This can be visualised by converting the spectra to RGB colours, as shown in the circle in the panel A and B.

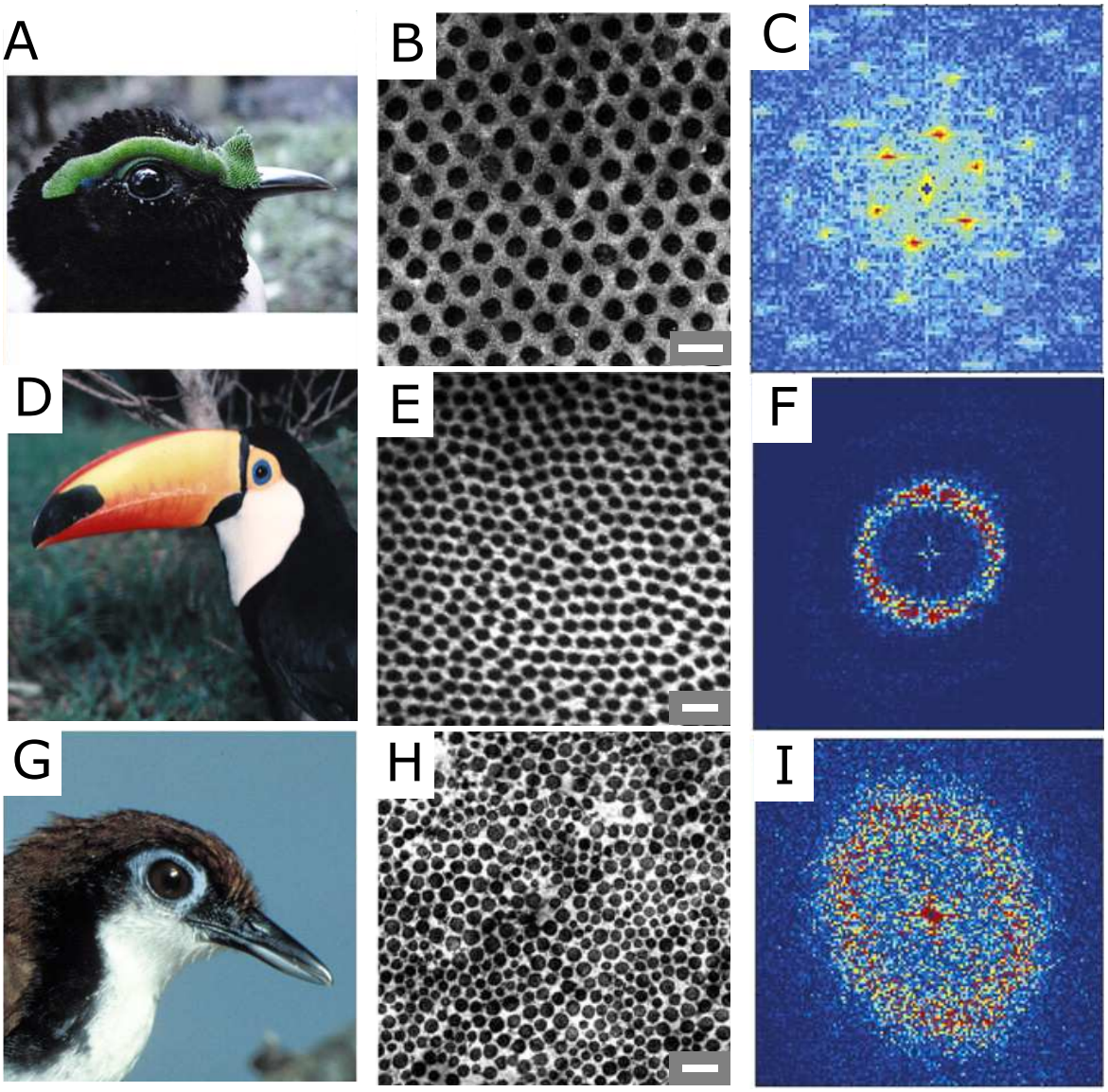

Fig. 4.4 *Philepitta castanea* photo (A). The light blue and green feathers show a hexagonal photonic structure under TEM (B). The periodicity of the pattern is apparent from the Fourier transform (C). *Ramphastos toco*: the dark blue feathers in the photo (D, around the bird's eye) contain a quasi-disordered photonic structure (E) where the spatial correlation between the scatterers gives rise to a ring-like Fourier pattern (F). The light blue colour of the eye feathers in *Gymnopithys leucapsis* (G) originates from a more disordered array (H) as shown by the weaker Fourier spectra (I). Adapted with permission from [13], The Journal of Experimental Biology. Scale bar: 200 nm.

The structural colouration of avian feathers has been known for over 100 years [153] and attributed to the quasi-random arrangement of air vacuoles in the medullary keratin [154]. In particular, two photonic arrangements are known: in the first, channel-type nanostructures that consist in elongated keratin bars run along air channels; in the second type, known as "sphere-type nanostructures", spherical air inclusions are embedded in a keratin matrix.

It has been shown that these nanostructured arrays can be arranged in highly ordered two-dimensional structures or in a completely disordered fashion [13]. This has been quantified by taking the Fourier transform of electron micrographs and small-angle X-ray scattering (SAXS) in a number of species (Figure 4.4). As expected, the most iridescent feather colours are associated with the structures that are closest to ideal periodicity. Conversely, isotropic patterns generate matte colours due to their rotational symmetry.

It is, however, more difficult to understand the behaviour of the arrays that show a ring-like pattern in Fourier space (Figure 4.4F).

Even though ring-like patterns are isotropic, they have a strong primary peak, implying the existence of a dominant length scale for structural correlation [12]. The resulting optical response is rather complex: the colour is independent of the feathers' orientation but varies with the observation angle. Furthermore, the reflected peak wavelength blue-shifts as the angle of incidence increases. This leads to the conclusion that the colour depends only on the angle between the incident beam and the detector arm, which excludes the possibility that the peak is originated by single Mie scattering (where the peak wavelength does not vary so dramatically with the angle).

Calculating the scattering cross-section of the keratin spheres shows that the peak in the reflectance is due to the collective interference of light scattered by many particles. The formal mathematical expression for this effect can be found in [12]. It is interesting how a seemingly disordered array can give rise to constructive interference due to the short-range ordering and how this is combined with an isotropic structure to obtain a non-iridescent response.

Disorder can also lead to angle-dependent colours that would not be achievable by periodic structures, as described in the following example.

Out of the myriad of structurally coloured organisms *Morpho* butterflies (Lepidoptera) are perhaps the most extensively studied. Their brilliant blue appearance came to the attention of the scientific community more than a century ago but was quantified for the first time only in 1999 [155]. Each scale covering the butterflies' wings is constituted by the repetition along extended ridges of chitin tree-like nanostructures. The brilliant blue colouration is, in the first approximation, due to the multilayer effect given by the chitin-air contrast. However, more

Fig. 4.5 Photographs of a male *Troides magellanus* butterfly. In these pictures, the illumination source is close to the observation point. One can observe that at normal incidence (A) only the yellow pigmentary colour is shown while at grazing incidence (B) the colour abruptly changes to blue. A structure is generated digitally to predict the optical response from the butterfly's scales (C). Adapted with permission from [156], The Optical Society of America.

subtle optical effects are due to the disorder of the structure (Figure 4.5). In fact, because of the random positioning of the ridges on the scales the scattered fields do not add with perfect coherence [19].

The first three-dimensional simulation of the complex *Morpho* structure showed how the gradual narrowing and offset of the single tree units contribute to the wide angular distribution of the signal [156]. However, later it was demonstrated that the placement of the trees themselves [157] as well as the randomisation of their height [158] prevents the typical multilayer-like angular dependence.

4.3 Polarisation effects

Disorder in a photonic structure can lead to the randomisation of the incident light's polarisation as a consequence of multiple scattering. For example, polarisation measurements on the white beetle *Cyphochilus insulanus* have shown that the cuticle has a low degree of polarisation and gloss, which is a desirable characteristic in a camouflaging material [159]. While this effect is roughly uniform in the three spatial dimensions for the white beetle, in the white damselfly *Pseudolestes mirabilis* the arrangement of the waxy fibres is random in two dimensions but ordered in the third (*i.e.* along the scales) [16]. Therefore, parallel and orthogonal polarisation are reflected differently, a signature which is common in two-dimensional photonic crystals but rather remarkable in disordered media.

4.4 Polycrystallinity and domains

Another example of disordered architectures which have peculiar optical properties are three-dimensional structures that show multiple domains within the crystalline lattice (Figure 4.6). In nature, polycrystallinity is fairly common: often biological photonic crystals are composed by a number of smaller crystallites [145]. Each of the crystallites can be approximated by a perfectly repeating lattice, but the domains themselves can have different sizes and orientations. Hence, a polycrystalline structure has a high degree of order within each domain but imperfect long-range periodicity, providing colour desaturation and a more angle-independent response.

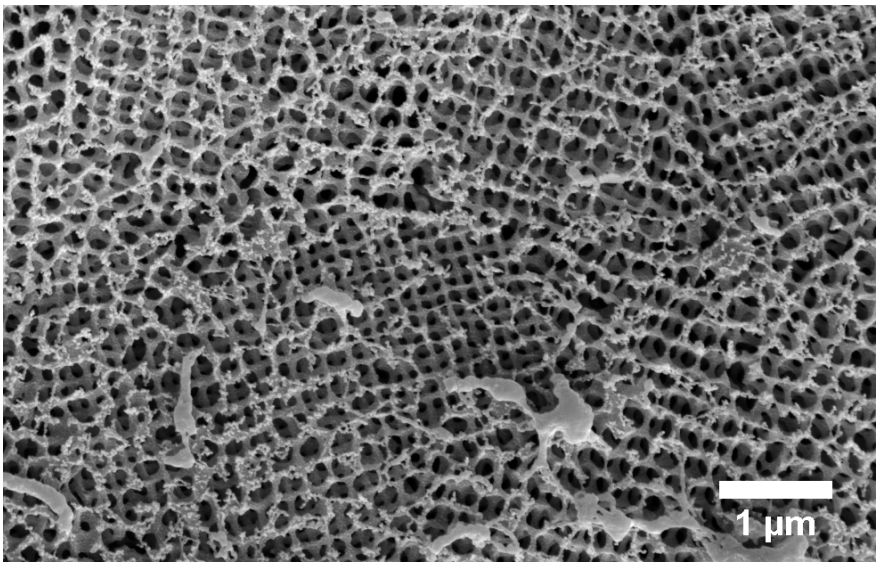

Fig. 4.6 The blue scales attached to the black cuticle of the beetle *Pachyrhynchus sarcitis* are composed by a polycrystalline three-dimensional photonic crystal, as illustrated by this SEM image.

Diamond-like three-dimensional photonic structures in nature have been observed inside the iridescent scales of the weevils *Lamprocyphus augustus* [160] and *Entimus imperialis* [161]. In both cases, micron-size domains which are differently oriented guarantee an almost angle-independent optical response.

Similarly, in some butterflies polycrystalline three-dimensional gyroids have been observed. These structures were invented by Alan Shoen, an engineer at NASA (National Aeronautics and Space Administration), in 1970. They are periodic structures of minimal surface composed of two distinct networks intertwined: one shows a six-fold geometry while the other is tetrahedral. Given the complexity and abstract nature of this crystal, the discovery of its occurrence in the cuticular structures of the lycaenid and papilionid butterflies in [162]

is truly fascinating. Later, similar structures have been found to be responsible for the optical responses of various species such as *C. rubi* [163, 164], *C. remus*, *P. sesostris* [165], and *T. opisena* [166]. As with the weevils, the crystalline structure is constituted of multiple domains with variable size and orientation. Indeed, the absence of circularly polarised reflection (which would be expected due to the inherent chirality of the gyroid network) in the wing of *C. rubi* and *T. imperialis* has been attributed to disorder [167].

4.5 Conclusion

This chapter summarises the most recent advances in the field of disordered photonics. Two main lessons can be learnt from this analysis.

Firstly, there are different "types" of disorder [168]. Depending on the spatial correlations in the photonic structure, one can observe disorder on a short- or long-range scale (or both); while depending on how the architectures form, one can define random structures as those where the final state is completely unpredictable as opposed to deterministic structures where the final state can be predicted if the initial state is known.

Secondly, disorder is not necessarily an undesirable feature in a photonic system [169]. In fact, some optical properties such as brilliant whiteness and metallic colourations utterly rely on the randomness of the photonic structure.

Chapter 5

Development of structural colours in green leaf beetles

As discussed in Chapter 1, structural colours in living organisms have been observed and analysed in a large number of species. However, it is still not known how the micro- and nano-scopic natural structures responsible of such colourations develop. Understanding the interplay between chemical composition, structural morphology, and mechanical constraints requires a range of investigative tools able to capture the different aspects of natural hierarchical architectures on multiple length scales. This Chapter[1] presents the developmental study of the most widespread strategy for structural colouration in nature: the cuticular multilayer.

The focus of this Chapter is on the exoskeletal growth of the dock leaf beetle *Gastrophysa viridula*, capturing all aspects of its formation: the macroscopic growth is tracked via synchrotron microtomography, while the submicron features are revealed by electron microscopy and light spectroscopy combined with numerical modelling, using the formalism introduced in Chapter 2.2. In particular, it is observed that the two main factors driving the formation of the colour-producing multilayers are the polymerization of melanin during the ecdysis and the change in the layer spacing during the schlerotisation of the cuticle. This understanding of the exoskeleton formation provides a unique insight into the different processes involved during metamorphosis.

[1] This work has been published as: Onelli, O. D., van de Kamp, T., Skepper, J. N., Powell, J., dos Santos Rolo, T., Baumbach, T., & Vignolini, S. (2017). Development of structural colour in leaf beetles. *Scientific Reports*, 7.

Fig. 5.1 The life cycle of the *G. viridula* from the egg (A, day 0-7) to the adult (F) via the larval stages (B, days 8-18:), pupa (C, days 18-25), after ecdysis (D, day 25), and the final cuticle expansion (from E, day 26). Scale bar: 1 cm.

5.1 Introduction

Multilayer reflectors are frequently found among arthropods and are particularly common in insects [170]. In fact, a great number of different species show structurally coloured scales [133] or *setae* [171]. The most common and best understood colour-producing mechanism by far is the multilayer reflector, which is often found in beetles (Coleoptera). These reflectors may be located at different depths within the cuticle [145, 172], which forms a multilayered exoskeleton (Appendix A) [173].

Being a natural fibre composite, the insect cuticle consists of chitin microfibrils embedded in a proteinous matrix [174, 175] which usually contains pigments such as tannins or melanin. In many iridescent insects, multilayer reflectors are generated by stratified deposition of pigments in different cuticular layers. Depending on the pigments types and contents, the refractive index of pigmented layers can vary significantly with respect to the chitin-protein matrix [148].

It has long been known that the cuticle is secreted by a single-sheet epithelium [176] whose products can vary in time during the development, giving overlying layers: the outermost epicuticle and the underlying, thicker procuticle, which can be further divided into exocuticle and endocuticle [174]. The development of the *trabeculae* (*i.e.* the columns

Description	Age (/days)	Photo	SR-μCT	TEM	Micro-graph	Spec-trum
1. Egg	0-7	5.1A				
2. Third instar larva	15-18	5.1B	5.2A,F			
3. Young pupa	18-20	5.1C	5.2B,G		5.4A	5.6A
4. Imago immediately after ecdysis	25-26	5.1D	5.2C,H	5.3A	5.4B	5.6A,B
5. Imago before cuticular expansion	26-27	5.1E	5.2D,I	5.3B	5.4C	5.6A,C
6. Imago with fully developed cuticle	30+	5.1F	5.2E,J	5.3C-F	5.4D	5.6A,D

Table 5.1 Summary of beetle's life stages considered in this study and respective figures.

connecting top and bottom sides of the elytra) has also been investigated and reported to begin from the dorsal cuticle, progress towards the ventral cuticle, and eventually merge with it [177]. In contrast, little is known about the development of the photonic structures: previous studies have concentrated on the development of butterfly scales [178–181, 166] and bird feathers barbs [182] showing the interplay of self-assembly and biologically-driven development. Even though the literature on metallic colouration in beetles is extensive, describing standard multilayer reflectors [183], circularly polarising helicoids [184], chirped broadband reflectors [145], and their taxonomic distribution [185, 186], their formation and development has never been investigated in living specimens.

5.2 Results and discussion

Adult *G. viridula* beetles are collected from the meadows by the river Cam in Cambridge, England (52°12'41.2"N, 0°07'43.4"E) and reared in the lab as described in [187].

The life cycle of *G.viridula* generally consists of the following phases: egg, three larval stages, pupa, and imago. In this Chapter, the focus is on the formation of the cuticular multilayer reflector in the hardened forewings (or elytra, see Appendix A) of the maturing adult beetle and refer to the following stages in the text: egg (1), third instar larva (2), young pupa (3), imago immediately after ecdysis (4), imago before cuticular expansion is completed (5), imago with fully developed cuticle (6). For a summary of the stages and relative imaging techniques refer to Table 5.1.

The eggs (Figure 5.1A) hatch 5-7 days after deposition. After feeding on dock leaves (*Rumex obtusifolius*) for 9-10 days, the larvae (Figure 5.1B) molt and turn into yellow pupae (Figure 5.1C) from which the imagoes emerge after 5-7 days of metamorphosis. The lifespan of the adult beetles varies between 20 and 30 days. Immediately after ecdysis, the cuticle of the imagoes is still yellow (Figure 5.1D) and even one week later, the insects' cuticles are not

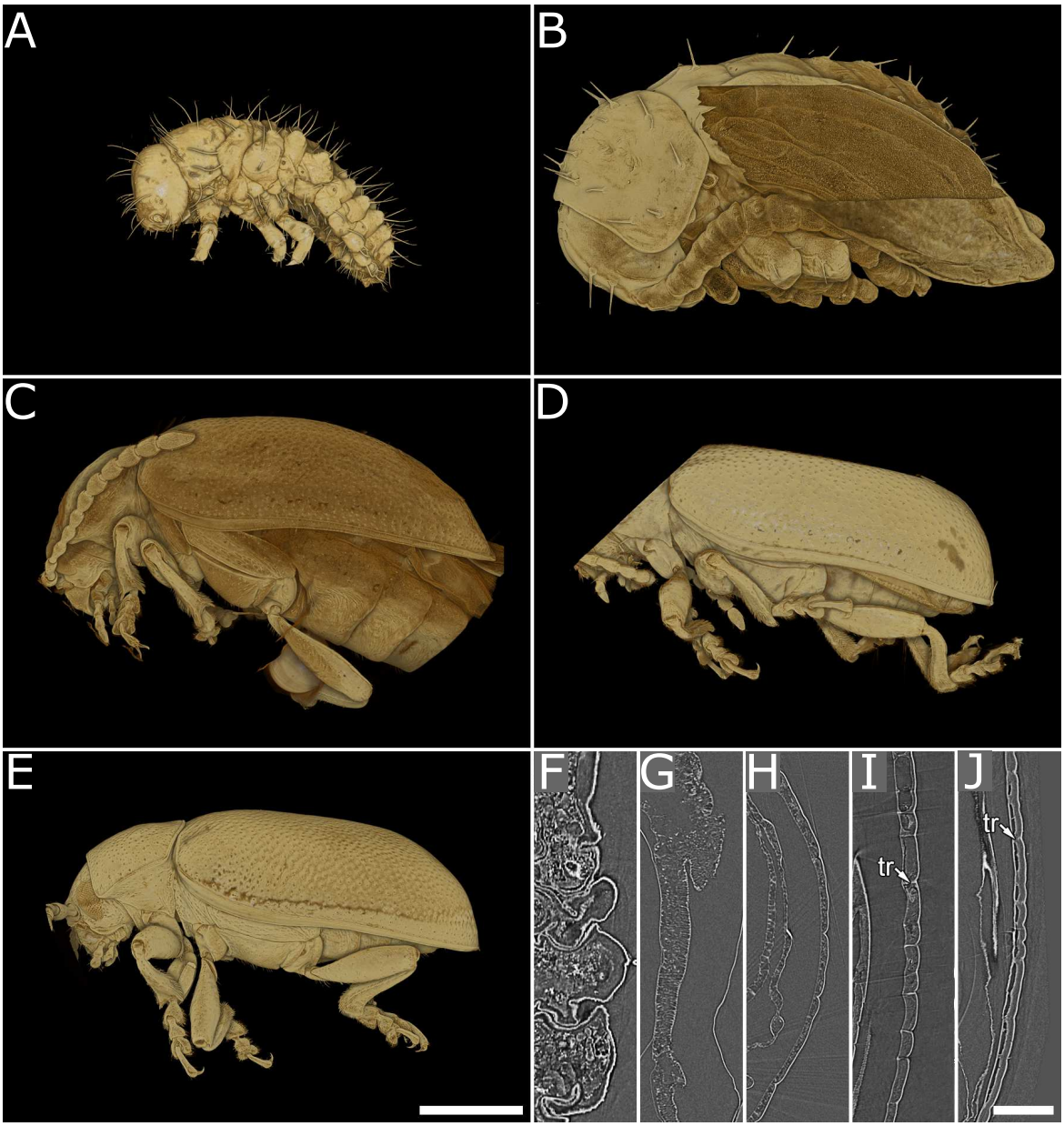

Fig. 5.2 A-E: results from SR-μCT scans showing volume renderings. F-J: cross-sections of the respective dataset. A,F: 3rd instar larva, which exhibits a soft cuticle. B,G: young pupa, pupal skin partly digitally removed to reveal the developing elytron. C,H: imago immediately after ecdysis. D,I: the young imago shows a fully-formed yet rucked up cuticle and the formation of *trabeculae* ("tr" in the figure). E,J: old imago with a fully developed cuticle. Scale bars: 1 mm. Image courtesy of Dr Thomas van de Kamp.

fully expanded (Figure 5.1E) resulting in a weaker colouration compared to those of older adults (Figure 5.1F).

In order to anatomically characterize the development of the beetles, SR-μCT scans of selected developmental stages are performed (Figure 5.2). The larvae do not exhibit wings but rather a soft, non-sclerotised cuticle (Figure 5.2A, F). The elytra begin to form in stage 3 (Figure 5.2B) and continue during stages 4 and 5 (Figure 5.2C, D). However, the cuticle in stage 4 (Figure 5.2H) is still considerably softer and thinner (1.0-1.5μm) than in the adults (4.0-4.5μm) in stages 5 and 6 (Figure 5.2G, J). In stage 4, the *trabeculae* are seen to originate dorsally (Figure 5.2H). It is only at a later stage that they start merging with the ventral cuticle (Figure 5.2I). Confirming the results in [177], *trabeculae* are seen to have completely developed and thickened in the adult (Figure 5.2J), spacing the inner and outer sections of the cuticle, which is about 4 μm thick. Finally, in the fully developed adults (Figure 5.2E) the cuticle is completely expanded (Figure 5.2J).

In order to resolve further details of the cuticular ultrastructure, the final stages of the development are imaged using TEM. In particular the specimens examined are: an individual immediately after ecdysis (stage 4), a young imago (stage 5; 5 days after emergence), and a fully developed imago (stage 6; 10 days after emergence). In stage 4 the dorsal elytral cuticle has an overall thickness of 1.0-1.5 μm (Figure 5.3A). The presumptive epicuticle appears to be formed by two thin layers with the innermost being more highly electron absorbing than the outer one (*i.e.* the first appear darker in the TEM images). The exocuticle consists of two distinguishable parts: an inner section of tightly packed layers arranged in a helicoidal fashion and outer section showing 5-7 alternating layers of varying electron densities, which constitute the multilayer reflector. At this stage, the endocuticle has not been deposited yet. The outer exocuticle in stage 5 appears thicker and more uniform (Figure 5.3B) consisting of 15-20 alternating layers. The contrast between the alternating layers of the reflector is more pronounced. In Figure 5.3 D, E it is possible to observe a helicoidal organization of the chitinous fibres in the dark-contrasted area of the inner exocuticle. Furthermore, the first endocuticlar layers have been deposited. In stage 6 the arrangement is similar to the earlier stage and only an increase in the number of endocuticular layers is observed (Figure 5.3C). As far as the architecture of the chitin fibrils in cuticle of *G. viridula* is concerned, one can distinguish two types of arrangements: pseudo-orthogonal endocuticular layers (Figure 5.3F) and a helicoidal exocuticle (Figure 5.3D,E). The pseudo-orthogonal one has been previously reported to be common in beetle endocuticle [188–190] but does not exhibit macrofibres, as present in several beetle species [175]. In the helicoid one can recognize alternating layers of different electron density due to the varying orientation of the fibres.

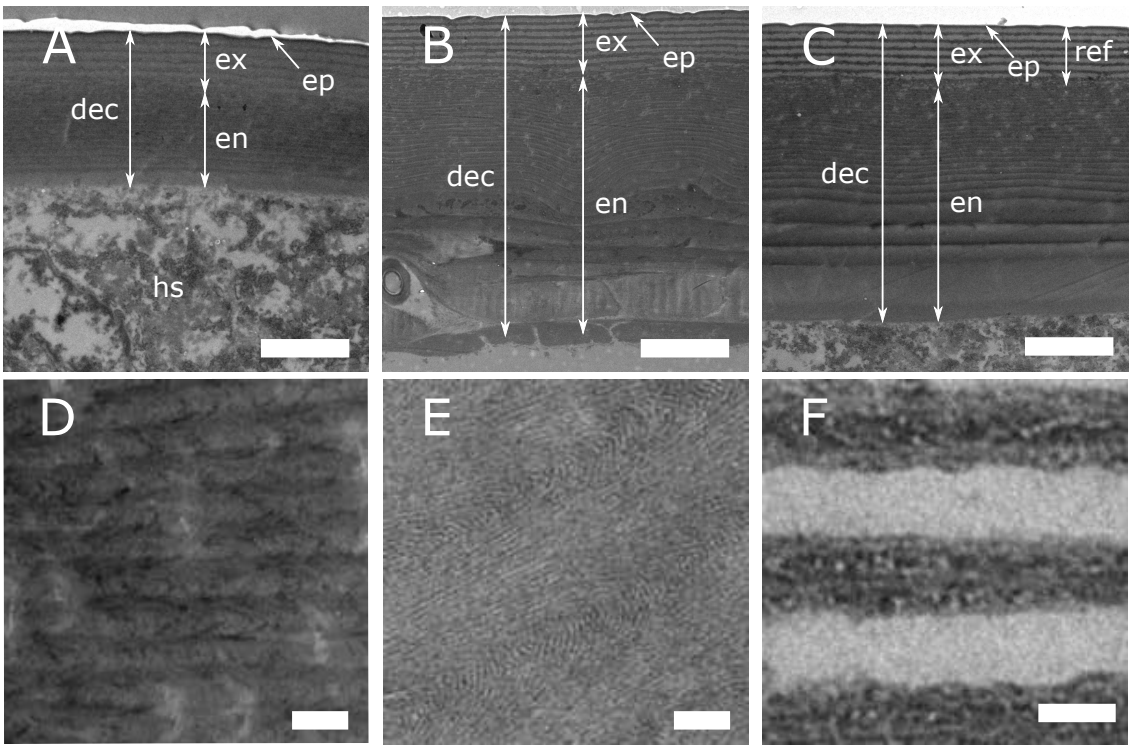

Fig. 5.3 TEM sections of the developing dorsal elytral cuticle ("dec" in the figure), which illustrate the development of the endocuticle ("en"), exocuticle ("ex"), and epicuticle ("ep"). The cuticle after ecdysis (Stage 4, A) is considerably thinner than in the later stages 5 and 6 (B, C). The hemolymph space ("hs") is visible underneath the elytra. In B, the young imago shows a more defined exocuticular multilayer reflector ("ref") and a thicker endocuticle. The old imago, C, exhibits a fully-formed cuticle. At higher magnification, it is possible to appreciate the structure of the inner exocuticle in (D-E) and the alternating fibril arrangement in the multilayer reflector in (F) for the fully formed imago. Scale bar: 2 μm for A-C, and 100 nm for D-F.

The development of the exocuticlar ultrastructure is monitored in living beetles spectroscopically. Figure 5.4A shows a micrograph in epi-illumination of the young pupal skin and the cuticle of the beetle in stage 4, 5, 6 is illustrated in Figure 5.4B, C, and D respectively. The spectrum for stages 3 to 6 is reported in Figure 5.6A. By comparing the measured optical response with the one predicted from transfer-matrix calculations [191], it is possible to quantify the variations of the cuticle in terms of its composition (Figure 5.6A).
The independent variables used in transfer-matrix method are:

1. the dimensions of the layers constituting the exocuticle;

2. their corresponding refractive indices.

To evaluate 1. for each stage of growth the thickness of the layers is extracted from the TEM sections: for each pixel in the TEM images, the grey level and position are measured using Image J (each line profile is averaged over 500 nm of cuticle) and then loaded into the Python simulation. The initial medium is assumed to be air (n_{air} = 1.0, infinite thickness) while the final medium is assumed to be the same as the last point measured (infinite thickness). The *s*- and *p*-polarisations are calculated separately and then averaged together to represent unpolarised light. The simulation runs between λ = 400 nm and λ = 800 nm in steps of 1 nm. The incident angle is varied between -37° and +37° in two-degree steps to match the numerical aperture of the microscope objective. The result from each calculation is averaged together: the Köhler illumination set-up guaranteed a uniform illumination and it is possible to perform a linear average (see Experimental Sections 3.1.1). Figure 5.5A shows the importance of performing such procedure to be able to faithfully model the experimental data. 20 of such profiles are averaged to recreate the experimental condition in which the spectra are, in fact, collected from an area which is roughly 10 μm in diameter. The individual profiles, in fact, can differ significantly as the periodicity of the multilayer is far from the ideal case. Figure 5.5B shows a comparison between the spectra obtained by simulating the single line profile and those obtained by averaging 20 profiles.

During the TEM sample preparation, the cuticle expanded (or contracted, for the adult stage) by a small amount and therefore the multilayer dimensions have been corrected to match the central reflectance peak. It is reasonable to assume that the younger stages have a greater water content and are expected to shrink after removal from the insect. In the adult insect (stage 6), the cuticle is already dead and hardened - therefore it does not shrink after removal. However, during processing for TEM a little shrinkage or swelling in the primary fix is to be expected if the effective molarity is not perfectly isotonic. The correction has been estimated independently by matching the peak wavelength for the simulated spectra to the experimental data (Table 5.2).

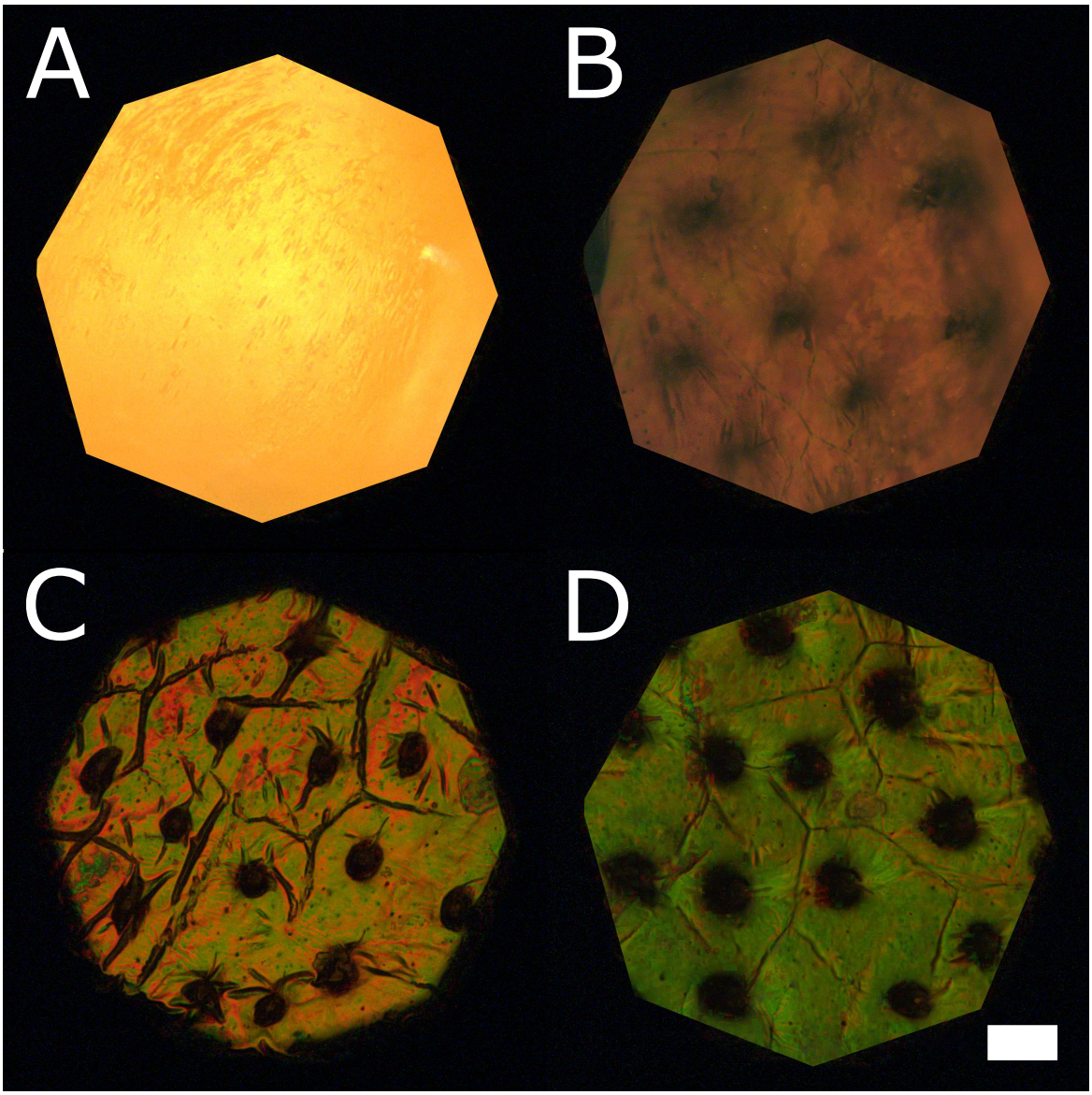

Fig. 5.4 Micrographs of the developing cuticle. A: the yellow pupal skin encasing the imago during pupation, when the cuticle is not yet formed. B: 3-4 days later the adult cuticle is starting to form and is distinguishable underneath the pupal skin. The formation of *trabeculae* is evident from the presence of dark invaginations. C: the imago has emerged but the cuticle is still not fully expanded. D: 5 days after ecdysis the cuticle has reached its final conformation. Scale bar: 1 mm.

Description	Correction
4. Imago immediately after ecdysis	- 15.0 %
5. Imago before cuticular expansion	- 9.4 %
6. Imago with fully developed cuticle	+ 5.0 %

Table 5.2 Summary of the size correction applied to the TEM images.

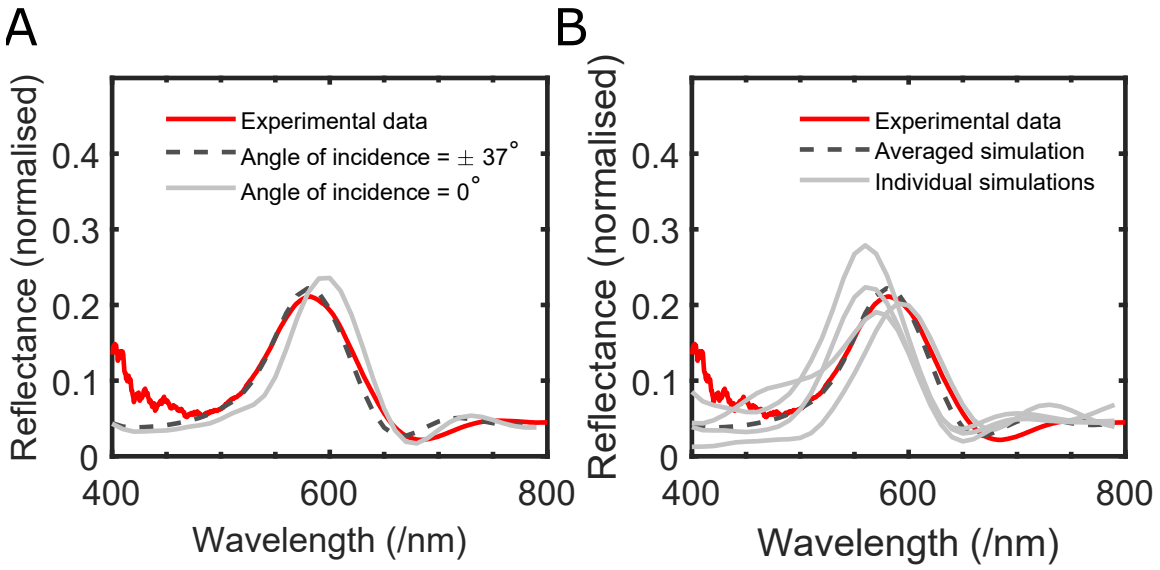

Fig. 5.5 A: the effect of taking the NA in collection of the microscope into account when simulating the response from the multilayer. The simulated signal depends strongly on the angle of the incident light. B: the layer thickness can vary substantially in different positions so that the simulated signals differ significantly. By averaging multiple simulations, one can recreate a more faithful representation of the experimental data.

The dispersion for the chitin-protein matrix refractive index n_1 used in this study for all the stages is the one measured in [192, 193]:

$$n_1 = 1.5145 + 8800/\lambda^2, \tag{5.1}$$

where λ is the wavelength of the incident light (in nm). For the melanin-contain layers the refractive index n_m is assumed to be comparable to that measured in [148]:

$$n_m = 1.648 + 23700/\lambda^2 + 0.56\exp(-\lambda/270)i. \tag{5.2}$$

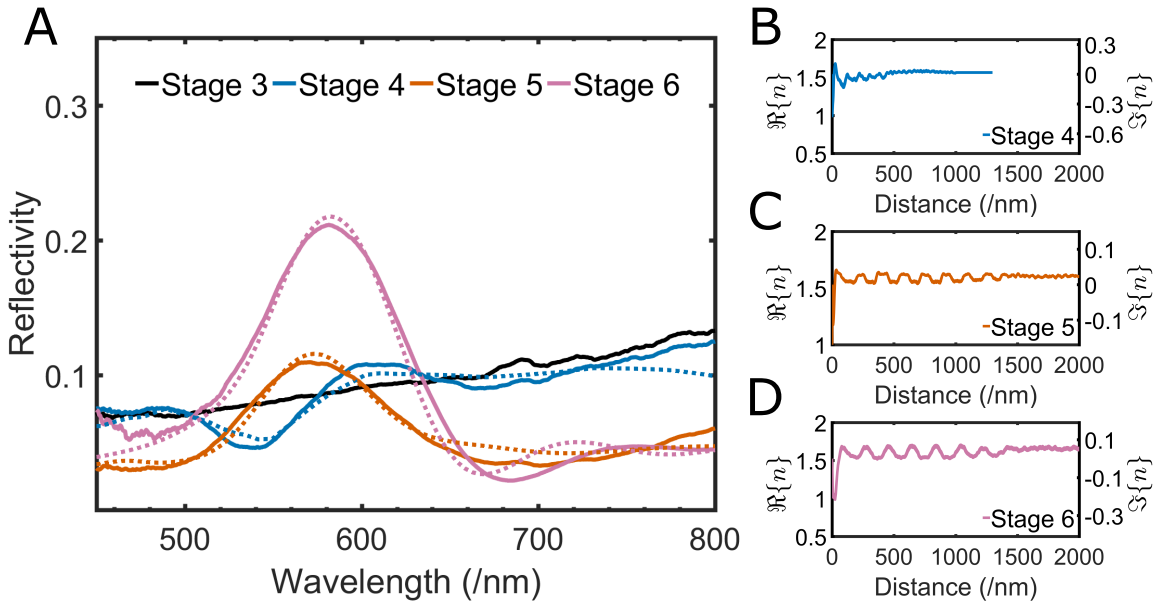

Fig. 5.6 A: the experimental spectra collected from a 10 μm spot (solid lines) compared to the spectral response as predicted by the transfer-matrix simulations (dashed lines). B-D: the real part and imaginary part of the refractive index as a function of the cuticle's depth at different stages of development of the cuticle (see legend).

For the quinone-containing layers, n_q is not known but it can be roughly estimated from the absorption spectra of quinones as reported in [194, 195]:

$$\begin{aligned} n_q = &\quad 0.1i \quad \text{for } \lambda < 510 \text{ nm} \\ = &\quad 0.009i \quad \text{for } \lambda > 589 \text{ nm} \\ = &\quad -19936643/\lambda^2 + 73331\lambda - 67 \quad \text{elsewhere.} \end{aligned} \tag{5.3}$$

The total refractive index n_2 for the pigment-containing layers is calculated using the effective medium approximation for each stage, since the ratio between the chitin-protein matrix and pigments changes during the development:

$$n_2 = n_1 f_1 + n_m f_m + n_q f_q, \tag{5.4}$$

where f_1, f_m,f_q are the relative filling fractions for the chitin-protein matrix, melanin, and quinone respectively. It follows that

$$1 = f_1 + f_m + f_q. \tag{5.5}$$

The dispersion deducted from the minimisation of the difference between the predicted and experimental reflectivity are illustrated in Figure 5.7A, B.

The young pupal skin (Figure 5.4A) does not show any evidence of structural colour as its spectrum is typical for pigment absorption (Figure 5.6A). Nevertheless, this incoherent pigmentary layer is still present immediately before the ecdysis (Figure 5.4B) and it plays a filtering role in the measured spectrum [196]. By absorbing in the 400 - 500 nm region, the pupal skin decreases the signal produced by the developing multilayer. Hence, the reflectivity in this part of the spectrum is lower than the one predicted from the modelling of the Bragg stack only (Figure 5.7C).

After ecdysis, a strong drop in reflectivity in the 530-550 nm wavelength region is observed (Figure 5.6A) which can be explained including in the calculation the presence of quinones in addition to melanin. These compounds have been shown to play a role in melanogenesis - which takes place during the schlerotisation of the cuticle, as reported in [197–199]. The presence of quinones is further confirmed by the reddish colouration observed in the microscopic image of the cuticle in stage 4 (Figure 5.4B), as expected in presence of this class of compounds [195, 194]. In particular, by fitting the measured spectra with the model the relative amount of melanin and quinones in the pigmented layers in stage 4 can be estimated to be 15% and 5%, respectively. For comparison, in Figure 5.7C it is possible to see how the predicted spectra varies when:

1. only the multilayer is contributing to the response;
2. no quinones are present;
3. the yellow pupal skin does not filter the signal;

showing that the effect of quinones must be included in order to explain the drop in the reflectance between 500 and 600 nm.

By comparing stage 4 with 5 and 6, one can also note that the multilayer is yet not fully developed at this stage: by plotting the complex refractive index as a function of the multilayer's depth, it can be observed that the contrast between the layers is low and that the distance between them is small (Figure 5.6B-D).

In stage 5 the cuticle shows a broad reflectivity peak around 580 nm (Figure 5.6A). At this stage, quinones are not present and the measured spectra agrees with the calculations using a melanin content of 57% for the pigmented layers.

Finally, when the cuticle of the old imago is fully expanded (Figure 5.4D), the peak reflectivity is considerably stronger than the one of the younger imago (Figure 5.6A). At this stage the melanisation has completed and the final percentage of melanin contained in the pigmented layers of chitin-protein matrix is estimated to be 79% (Figure 5.6D).

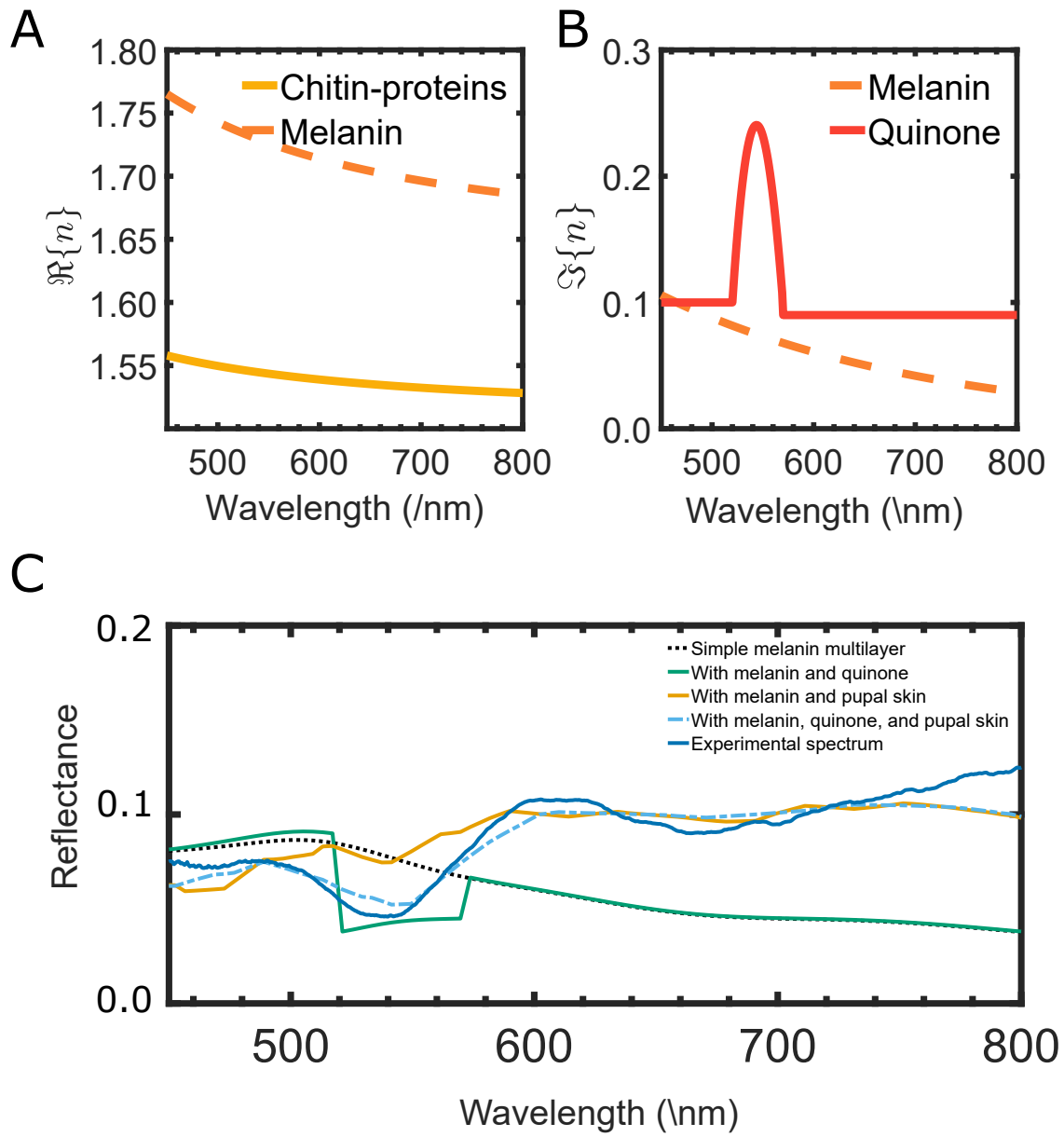

Fig. 5.7 A: the dispersion for the chitin-protein matrix and melanin-containing layers (Equation 5.1 and Equation 5.2) and for the imaginary part of the melanin-containing layers and quinone-containing ones (B, Equation 5.2 and Equation 5.3). C: the experimentally measured as compared to the predicted intensity from the numerical model (see legend).

5.3 Conclusion

The multi-scale imaging and spectroscopical study described in this Chapter allows to reveal the different processes involved in the development of the exocuticule of a structurally coloured beetle.

It is possible to conclude that the adult colouration of this species is achieved by an increase in the dimensions of the layers and by their melanisation in the outer exocuticle. Interestingly, the layer deposition and the melanisation happen in different stages. It is particularly surprising that the latter process is observed after stage 4 when the deposition of the endocuticle has already started. However, it is not possible, at this point, to observe the cuticle before stage 4 with enough resolution to discern the the different layers. This could be the subject of further investigation in the future using less invasive electron microscopy techniques (*e.g.* cryo-SEM) which are more suitable for highly aqueous samples.

It can be hypothesised that even small variations during the development can result in extreme colour differences, making these architectures suitable for quick adaptation and species diversification - possibly faster than changing highly conserved biosynthetic pathways for pigmentation, which are controlled by a complex set of enzymes and genetics [200] including different gene classes for biosynthesis and spatiotemporal positioning of pigments [201]. In comparison, altering cuticle deposition patterns appears to be a simpler approach. This supposition is further exemplified by the occurrence of numerous repeated evolutionary origins of multilayer reflectors in beetles [145] and also explains how closely related species, such as in the beetle genera *Eupholus* and *Cetonia*, can produce very different colourations. In the context of avian structural colouration it has been shown that the colouration can in fact vary even within the same generation as a consequence of nutritional [202, 203] and seasonal changes [204].

High resolution TEM images reveal that a helicoidal organization of chitin fibrils is maintained in the entire cuticle [189]. However, even if the characteristic dimensions of such helicoidal architecture do not contribute to the optical response in this case, its dimensions (of about 800 nm) might indicate that exocuticle is predisposed to the development of chiral Bragg reflectors [145]. However, it is important to consider that another main function of the exoskeleton is to provide mechanical support and thus the helicoidal disposition of the fibres could also have derived from the evolution of a mechanically strong structure.

More generally, this study sheds new insight on cuticle development: from an evolutionary point of view, it is interesting to note that pigmented-based multilayer reflectors are very common among different insects and other arthropods and therefore the mechanisms observed in this case of development might be generalized to other species, since the same materials and strategies are involved.

Chapter 6

Avian brood parasite mimics host eggs using both pigmentary and structural colour

Brood parasites deposit their eggs in other birds' nests, exploiting the hosts to care for the eggs and resulting offspring. Often, the hosts do not accept the foreign eggs and eject them from their nest, leading to the fascinating co-evolution of parallel strategies: as the parasites optimise the mimicry of the host egg to avoid rejection, the hosts evolve increasingly more complex "signatures" which are harder to forge.

An example of such an arms race is the competition between the brown-backed honeybird (*Prodotiscus regulus*) and its host, the spotted prinia (*Prinia maculosa*). The eggshells of the host are characterised by a blue, pigmentary colouration. The parasite, however, belongs to a lineage of birds that has laid only white eggs for a very long period of evolutionary time: it belongs to the order Piciformes (which also includes the woodpecker, barbet, toucan and honeyguide families), all of which nest in holes and so, as is common for hole-nesters [205], lay unmarked white eggs. Since the common ancestor of the Piciformes is estimated to have lived 62.9 million years ago [206], it is possible to infer that the ability to lay coloured eggs was lost around this time. White is the default and ancestral colour for bird eggs, since in the absence of pigment they are simply the colour of the calcite making up the shell [205].

The only known exception is the genus Prodotiscus (a member of the honeyguide family Indicatoridae, of which all 17 species are thought to be brood-parasitic), which contains two species. The green-backed honeyguide *P. zambeziae* is known to lay white or plain blue eggs to mimic the eggs of its white- or blue-egged hosts (white-eyes, *Zosterops* spp.) [207], whereas the brown-backed honeyguide *P. regulus* was recently discovered to lay pale blue eggs with fine brown spotting [208]. The question, then, arises: what mechanism does *P.*

regulus use produce blue colouration, given that laying coloured eggs appears to have been lost long ago in evolutionary time?

This chapter[1] explores the interplay between pigmentary and structural colours in *P. regulus* and in other Afrotropical species using both pigment extraction techniques and advanced imaging combined with numerical modelling.

It is found that *P. regulus* is currently able to produce the same blue pigment as *P. maculosa*. The colouration is further enhanced in brightness by a disordered structure constituted by air inclusions randomly placed in the shell's calcium carbonate matrix ($CaCO_3$).

This study constitutes the first discovery of the presence of the pigment biliverdin in the Indicatoridae family and the discovery of a photonic nanostructure within avian eggshells.

6.1 Introduction

Brood parasitism is a common behaviour in the cuckoos (Cuculiformes) and also occurs in other bird orders such as cowbirds and finches (Passeriformes), honeyguides (Piciformes), and one duck species (Anseriformes) [209]. These organisms have evolved complex strategies in order to avoid host rejection, which has in parallel improved in recognising extraneous eggs.

Perhaps the most spectacular example of this arms race is the highly-evolved mimicry between the host and parasitic eggs. The latter have successfully forged the size and shape of the host's eggshells to such accuracy that one single honeyguide species (*I. indicator*) has specialised in matching up to six different hosts [210]. Colours and patterns are also perfected to avoid rejection by the host that, at the same time, matches the cuckoo efforts by increasing the complexity of its eggshell patterns [211].

Avian vision differs from human vision as birds are more sensitive to UV wavelengths. Studies have shown that the eggs are, in fact, matching the colours in the avian vision space [212, 213].

The colours of the eggshells are typically due to two pigments: protoporphyrin (brown-red) and biliverdin (blue-green) [214]. It is not clear how the patterns are formed but it is known that the pigments are deposited on the white shell just hours before deposition and it is speculated that the patterns are due to the rotation and speed of the egg as it passes through the shell gland [215, 216].

[1] Manuscript in preparation in collaboration with Spottiswoode, C. N., Johansen V. E., Steiner L. M., Walton J., and Vignolini, S. The authors acknowledge Jessie Walton and the late Rob Martin for the discovery of the *P. regulus* population and for the samples.

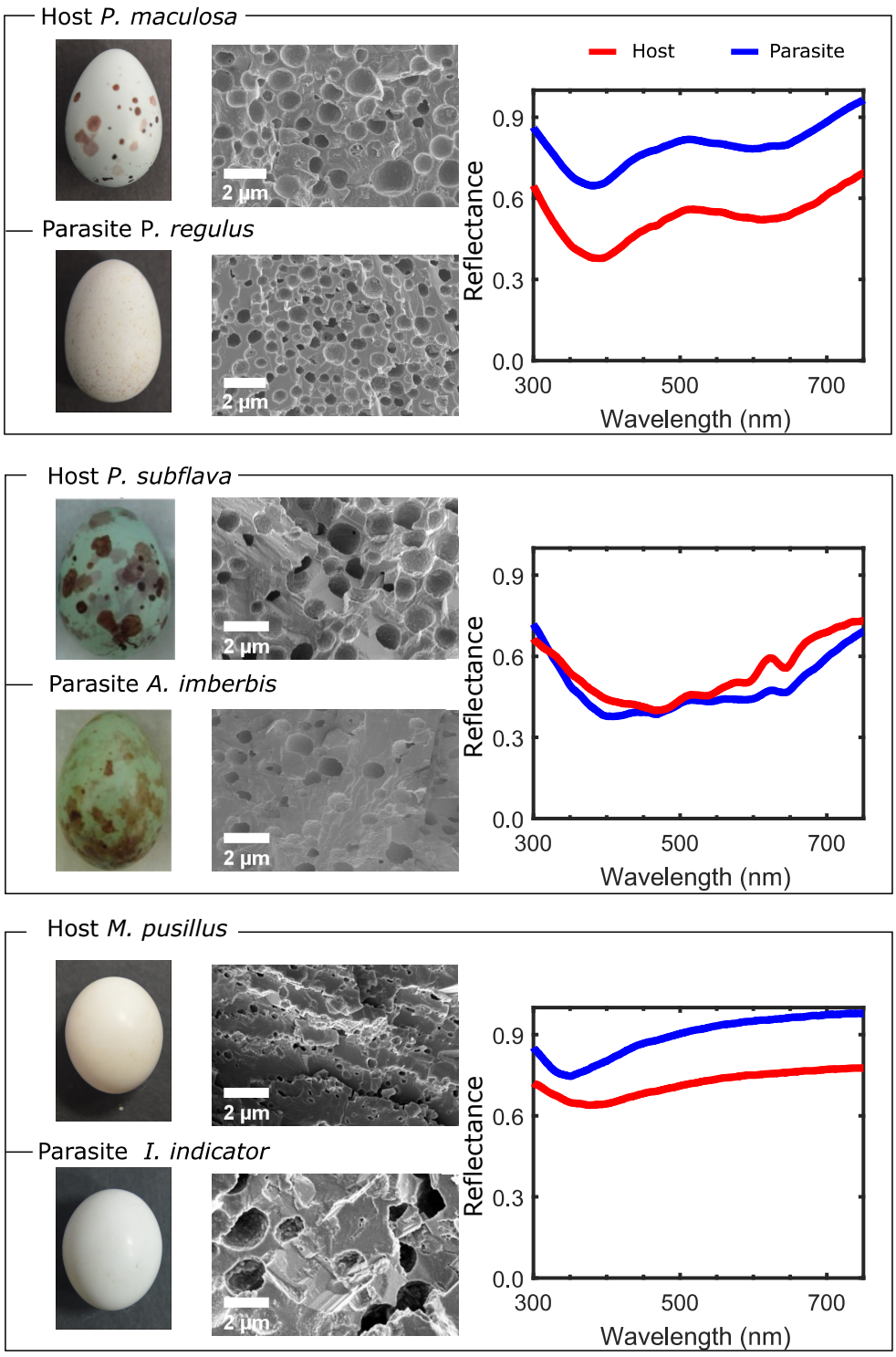

Fig. 6.1 Pairwise comparison of the host/parasite. From left to right: egg appearance, internal nanostructure as imaged *via* SEM, and UV-visible spectra. Middle two photographs courtesy of Dr Claire N Spottiswoode.

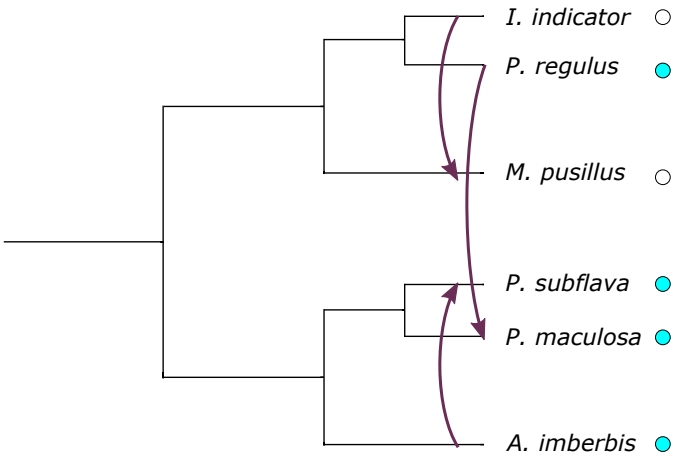

Fig. 6.2 Simplified phylogenetic tree showing only the species considered in the present study. The arrows go from the parasite to its specific victim. The coloured spots indicate the colour of the eggshells considered here.

In this chapter, the mimicry between three pairs of Afrotropical host-parasite eggshells that belong to closely related phylogenetic groups is discussed (Figure 6.1-6.2). In particular, the focus is on the brown-backed honeybird (*Prodotiscus regulus*) that lays its eggs in the nest of the spotted prinia (*Prinia maculosa*). Both eggshells show a pale blue colour which, for *P. maculosa*, is thought to be a consequence of the presence of biliverdin as this pigment is commonly found in the shells of its family (Cisticolidae) [217]. *P. regulus*, however, belongs to a family where only white eggs have been reported (Indicatoridae). This species must have therefore evolved a method to produce a blue colouration: using chemical extraction, microspectroscopy, and computational modelling it is possible to investigate the interplay between pigmentary colouration and structural colour which are found to contribute both to the optical appearance of the eggs.

For comparison, the blue eggs of the tawny-flanked prinia (*Prinia subflava*, Cisticolidae) are presented alongside those of their parasite, the cuckoo finch (*Anomalospiza imberbis*, Viduidae). Finally, two species characterised by white eggshells are analysed, the little bee eater (*Merops pusillus*, Meropidae) and its brood parasite, the greater honeyguide (*Indicator indicator*, Indicatoridae).

The colouration of the eggshells is measured with optical spectroscopy to quantify the spectral similarities and differences between the various species.

To assess whether biliverdin is present in *P. regulus* eggshells, the pigments are extracted using solvents and purified *via* HPLC (High-Performance Liquid Chromatography). The different fractions are then analysed with mass spectrometry (these procedure are performed by Lisa M Steiner).

The porous nanostructure of the eggshells is observed by SEM and FIB milling is carried out to access the full three-dimensional architecture so that the positions and sizes of the air pores can be extracted from the images. These are used for computational modelling to

predict whether the air inclusions play a role in the scattering of light and in the structural colouration (simulations done by Dr Villads E Johansen).

Species	Photo	Spectrum	Pigment extraction	SEM	FIB	Simulation
P. maculosa	6.1	6.1	✓	6.1		6.6C,D
P. regulus	6.1	6.1	✓	6.1	6.4	6.6C,E
P. subflava	6.1	6.1		6.1		
A. imberbis	6.1	6.1		6.1		
M. pusillus	6.1	6.1		6.1		
I. indicator	6.1	6.1		6.1		

Table 6.1 Summary of the techniques used for each species and relevant figures.

6.2 Results and discussion

Table 6.1 summarises the experimental and numerical methods used for each species.

Spectroscopic investigation

As shown in Figure 6.1, the surface colours and patterns of the eggshells in the host species are well-matched by those of the parasites (each spectrum in the plot is the average of >10 measurements on eggs from three or more different nests). More quantitatively, the spectra show that *A. imberbis* almost perfectly mimics the *P. subflava* eggs. Both eggs are known to contain biliverdin, whose absorption peaks around 400 nm [218]. An analogous absorption dip is seen in *P. maculosa* and *P. regulus*. Here, however, while the spectral shape is very similar for both species, the intensity is higher for the parasitic one. Finally, the comparison between the two white egg species shows a very similar spectral shape but a different intensity.

The brown spots visible on the eggshells of *P. maculosa* and *P. regulus* (Figure 6.1) can be measured individually using optical microspectroscopy. These areas show a spectrum characteristic of protoporphyrin (see later, Figure 6.7A) [219]. The difference in intensity is nonetheless present, suggesting that the brightness enhancement is not pigment-specific but affects the entire eggshell.

Chemical composition

To assess whether the difference between *P. maculosa* and *P. regulus* is due to different colouration strategies (*i.e.* pigmentary versus structural), HPLC is used to separate the

pigment content of the eggshells by fractionating the different compounds in the mixture. As these eggs are rare and difficult to collect, it is not possible to use the commonly-used method of comparing the HPLC results with a calibration standard as this would require a large amount of material. Unfortunately, this also implies that the concentration of the pigments in the shells cannot be estimated from this experiment. However, the different fractions collected from the HPLC procedure are accessible for further analysis using complementary techniques [220].

Here, mass spectrometry is used to integrate the results from the HPLC for the determination of the chemical composition of the material extracted from the eggshell. In particular, for both species the same molecular mass-to-charge ratio is measured, 583 m/z, as well as the same fragmentation pattern. These results are compatible with the mass spectrum of biliverdin meaning that the blue pigment is present in both species [220]. This is the first time such pigment is found in the family Indicatoridae. The presence of the brown pigment protoporphyrin is also confirmed by the measurement.

Anatomical study

From cross-sectional SEM imaging of the eggshells, it is possible to see that all the species considered show a large number of air inclusions in the calcium carbonate matrix that can act as scatterers (Figure 6.1,6.4). The thickness of the eggshells is found to be around 40-60 μm for all the species with the exception of *I. indicator* which shows a thicker shells ($\sim$ 100 μm) 6.3A-B. The eggshell thickness plays a role in enhancing the brightness of *I. indicator* eggshells with respect to those of its host *M. pusillus*: as the number of scatterers increases, more scattering events occur, enhancing the intensity of the spectrum. It is thus possible to conclude that the difference in reflectance between the two species is due to the different thickness.

The air pores differ from species to species in size and packing density: *P. regulus* appears to have the smallest and most densely-packed spheres, resembling the appearance of a disordered inverse opal [221]. From the SEM images, one can extract the *radii* of the spheres and their density (measured as the ratio between the area occupied by the air and the total area of the image). To automate the process, a Python package ("Blob Detection" from the *scikit-image* library) is used, as shown in Figure 6.3C,D. For each species, data is collected from tens of images relative to three or more different eggs from different nests.

According to this analysis, air fills (31$\pm$8)% of the area in *P. regulus* as compared to (19$\pm$1)% in *P. maculosa*. Packing efficiency is a key parameter in light scattering and the difference in the filling fraction between the two species is a significant indicator, supporting the hypothesis that the scattering efficiency is higher in *P. regulus* eggs.

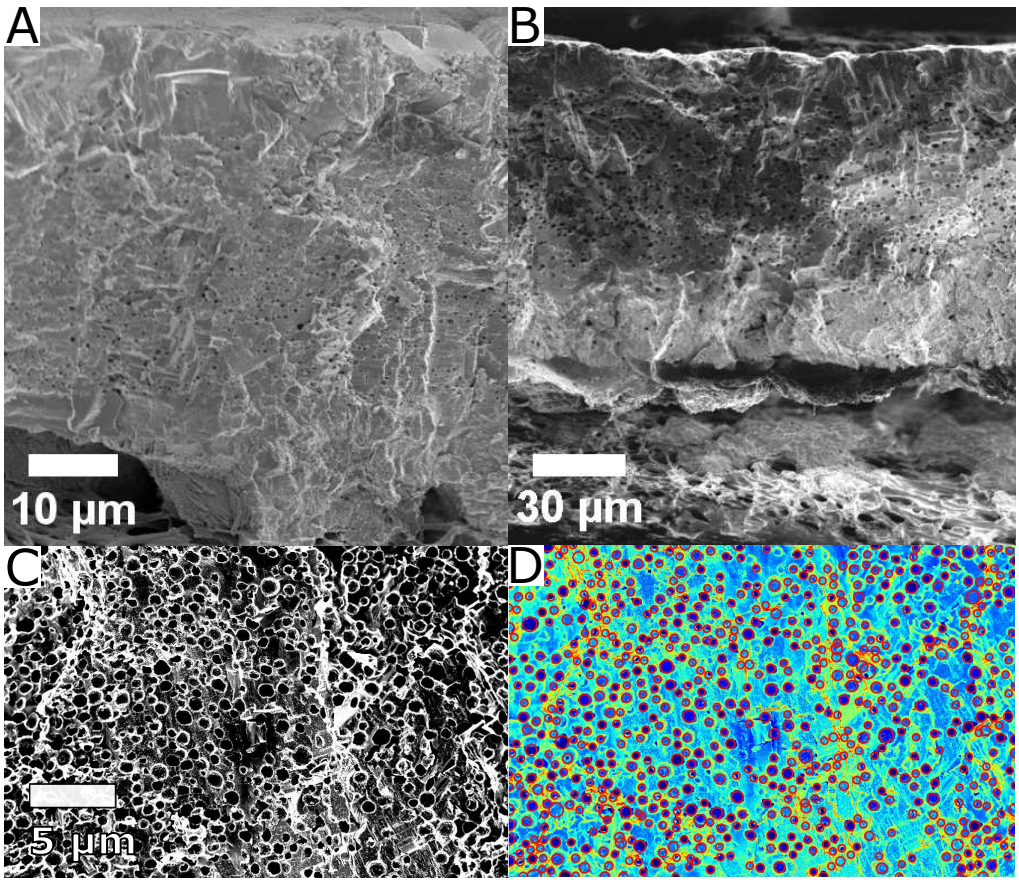

Fig. 6.3 A: *M. pusillus* eggshell in cross-section. B: cross-sectional view of *I. indicator* eggshell. Note the different scale bar. C: SEM image showing the cross-section of a *P. regulus* egg after thresholding. D: the effect of the "Blob Detection" algorithm using the Laplacian of Gaussian approach (the red circles indicate the air pores as detected).

The size of the scattering elements with respect to the incident wavelength is also a crucial variable for determining the scattering efficiency of a material. Measuring the diameters of the air inclusions from SEM images is, however, affected by various sources of error. The first effect leads to an underestimation of the sizes: the particles are sectioned at random so that the measured diameter is not necessarily the maximum one (*i.e.* the cut can expose the equatorial plane in some cases and positions close to the poles in others). However, there are two more source of artefacts which lead to overestimating the sizes: a random section is more likely to show the larger particles rather than the small ones; in addition, the cross-sections are not always perfectly orthogonal to the shells surface. Hence, FIB milling is carried out to measure directly the particles' *radii* and compare them to the results from the SEM analysis.

FIB milling consists of slicing and removing thin sections from the sample in order to expose sequential sections of the volume which are imaged using an SEM. The slice

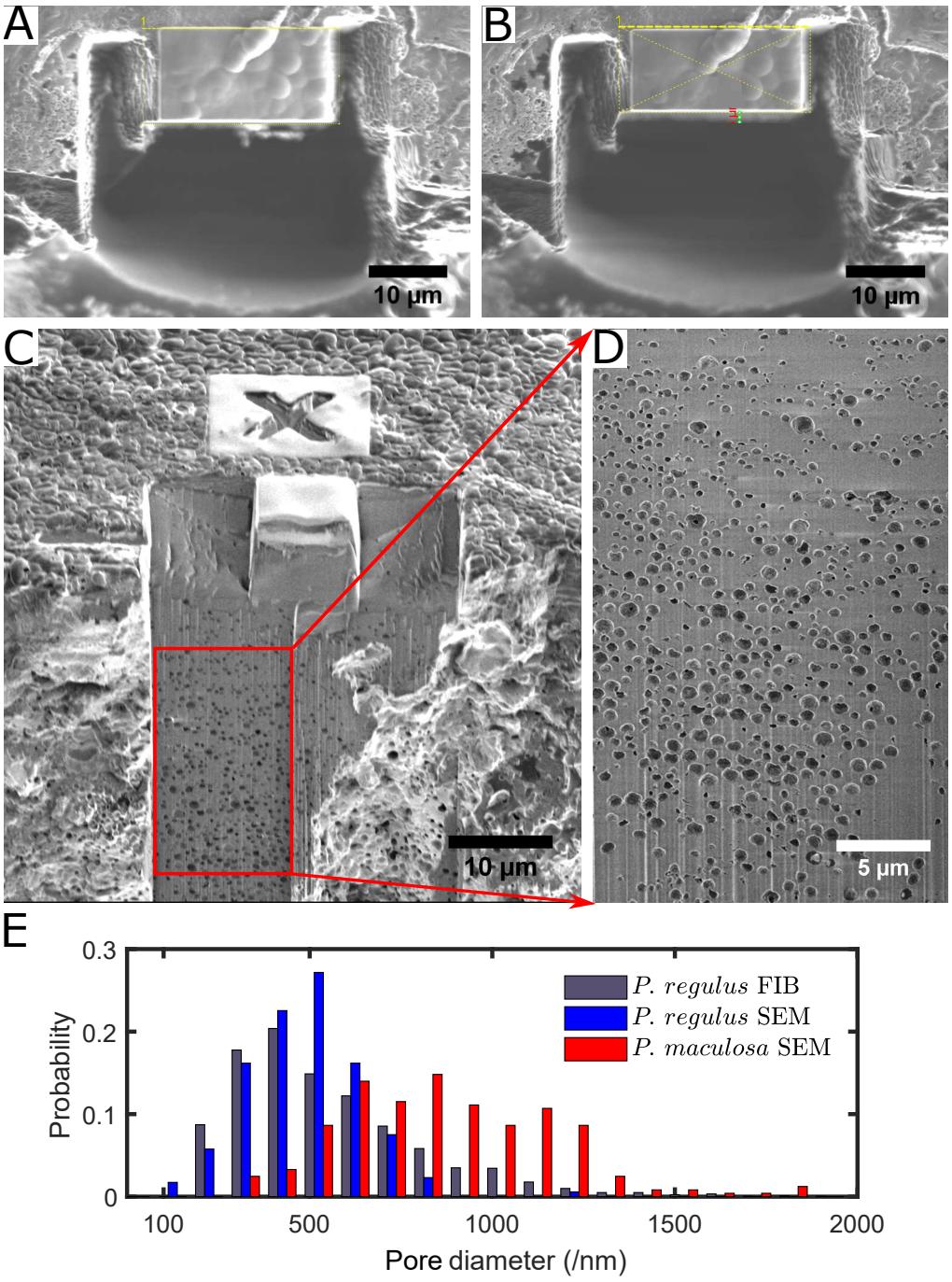

Fig. 6.4 A: top-view of the FIB milling site (*P. regulus*). B: the same site imaged after the slicing. C: the milling site as imaged during the slicing. The area indicated by the red rectangle is the section of the image used for data extraction. The X sign is a fiducial mark used to align the images during post-processing. D: a sample image after post-processing. E: histogram showing the difference between the air pores size in *P. regulus* and *P. maculosa* as measured from SEM and FIB images.

thickness can be measured by comparing the sample thickness before and after the procedure and dividing by the number of slices (Figure 6.4A,B). Here, the slice thickness is 42 nm (for more details see Experimental Section 3.2).

As illustrated in Figure 6.4C, a fiducial mark is placed near the region of interest to provide a static reference for the re-alignment of the images during post-processing. In this way, one can correct the alignment error due to the drift of the electron (or ion) beam which substantially affects long-exposure experiments (in this case, the images are acquired over 12 hours).

Figure 6.4C-D show how the two-dimensional images are obtained from the region of interest. From these, it is possible to perform a three-dimensional volume reconstruction after post-processing, as described in Experimental Section 3.2. A rendering of the obtained volume is displayed in Figure 6.5.

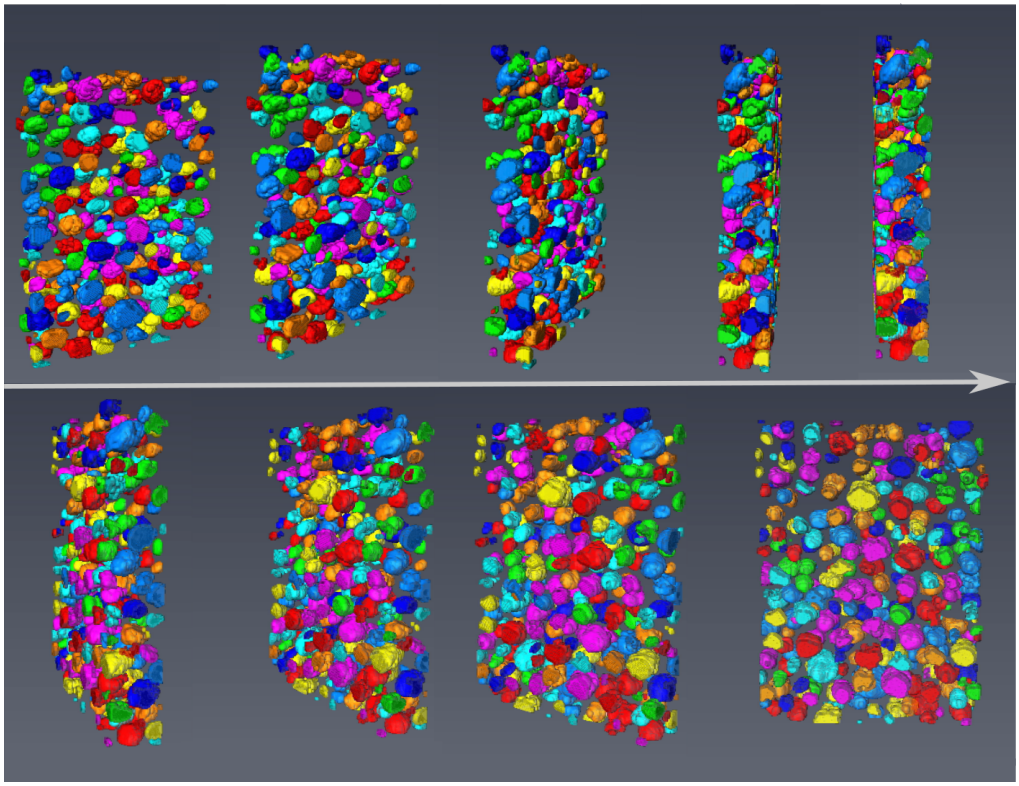

Fig. 6.5 The three-dimensional reconstruction of the air inclusions as carried out using Avizo (the volume is rotated around its vertical axis in the image sequence). The particles are labelled using different colours. Only a quarter of the total volume extracted from FIB milling is shown for clarity.

From the volume reconstruction one can measure the *radii* of the spheroids and the coordinates of their centre-of-mass. By comparing the *radii* extrapolated from this procedure

with those measured from the SEM images, it is possible to observe that the SEM protocol overestimates the diameters by ∼20% (Figure 6.4E. Sample size: 243 for "*P. maculosa* SEM", 173 for "*P. regulus* SEM", and 1801 for "*P. regulus* FIB"). It is thus reasonable to assume that the measurements regarding *P. maculosa* are affected in a similar way. In fact, the mismatch between measures carried out on two-dimensional images versus actual three-dimensional ones is a phenomenon known in the literature [222].

Numerical simulation

As the topology of the samples is known, a computational model based on the scattering from the ensemble can be built to test whether the two eggshells scatter light differently. Figure 6.6A shows the average scattering efficiency for the scatterers considered individually and for the scatterers considered as an ensemble, both are normalised to the projected area of the particle (in the case of the ensemble this also includes shadowing effects and crosstalk). From the results one infers that the scattering from the eggshells cannot be modelled as the sum of the contribution from single scatterers but the whole structure needs to be taken into account in order to include any effects due to having an ensemble of densely packed scatterers, such as shadowing and interference. The code used for modelling is the Multiple Sphere T Matrix simulation (or MSTM), a Fortran-90 code by Dan Mackowski based on [223].

Running a MSTM simulation on one 20x20x20 μm^3 cube filled with artificially-generated air inclusions resembling the respective sizes and arrangement in *P. maculosa* and *P. regulus* shows that the parasite eggshells scatter light more efficiently than the host (Figure 6.6C-E). As the eggshells are similar in thickness, this implies that a *P. regulus* shell reflects more light as compared to a *P. maculosa* shell, a result which agrees with the experimentally measured spectra in Figure 6.1.

Surface effects

To further confirm that the enhanced reflectance of *P. regulus* is only due to multiple scattering, the surface of the eggs is analysed. Surface effects and glossiness (or mirror-like shine) in avian eggshells has been studied in various species that exhibit extremely smooth shells [224]. In order to exclude that the difference in scattering response of *P. regulus* and *P. maculosa* eggshells is due to surface effects the following experiments are conducted:

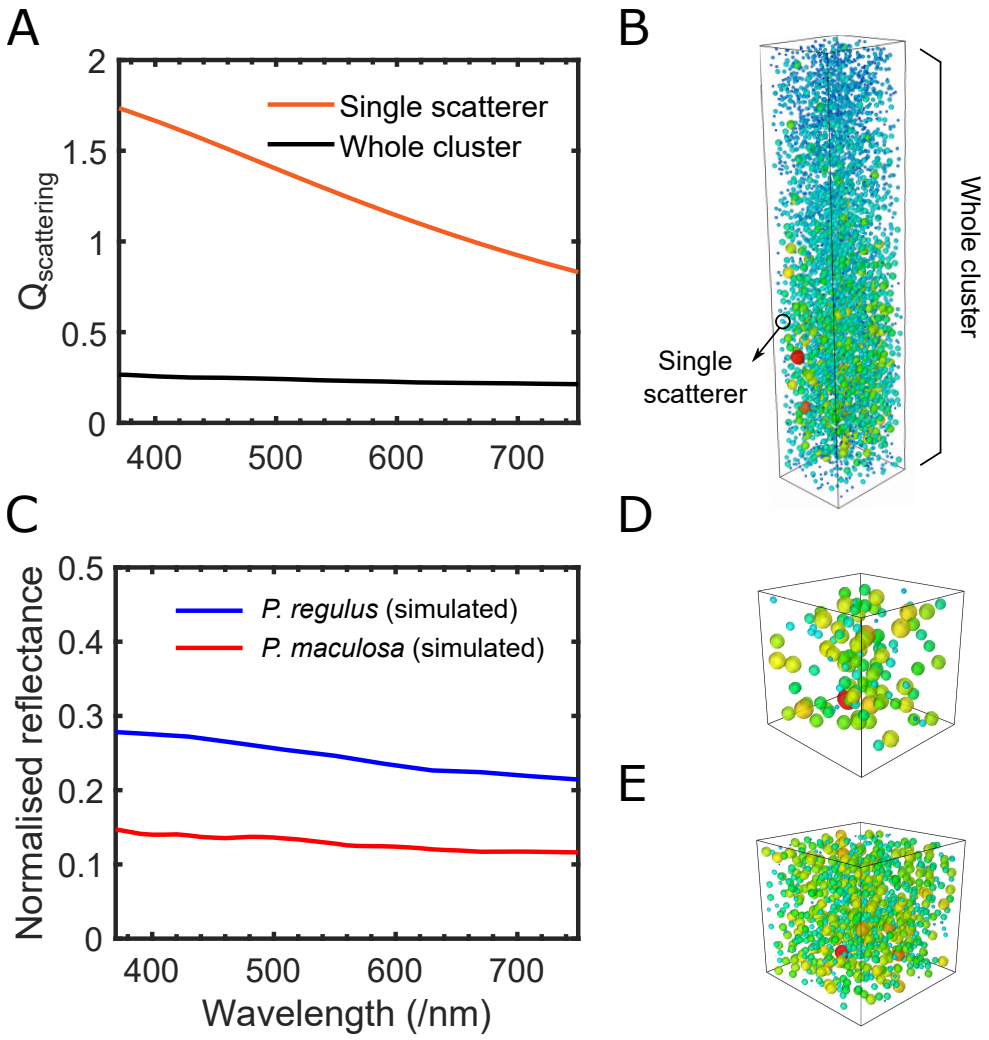

Fig. 6.6 A: the simulated average scattering efficiency ($Q_{scattering}$) from the whole cluster of scatterers as reconstructed from the FIB volume compared to the average scattering from the single particles. B: the cluster used for the simulation in A (*P. regulus*, from FIB milling). C: the comparison between the simulated reflectance for the two birds supports the experimental data. D: the artificially-generated cluster used for the modelling in C of *P. maculosa*. E: the artificially-generated cluster used for the modelling in C of *P. regulus*. Image courtesy of Dr Villads Johansen.

1. A replica of the shell's surface is obtained using polydimethylsiloxane (PDMS) to fabricate a cast of the surface (a method commonly used in the field of plant photonics [225]): Sylgard 184 silicon elastomer and its curing agent (Sigma-Aldrich) are stirred together (10:1 ratio) and poured over the eggshell. The mixture is left to harden for 24 hours at room temperature. Spectra from the replica of the eggshell and from a solid block of PDMS of comparable thickness are collected *via* optical microspectroscopy. As shown in Figure 6.7B, the surface roughness does not enhance the signal at any specific wavelength.

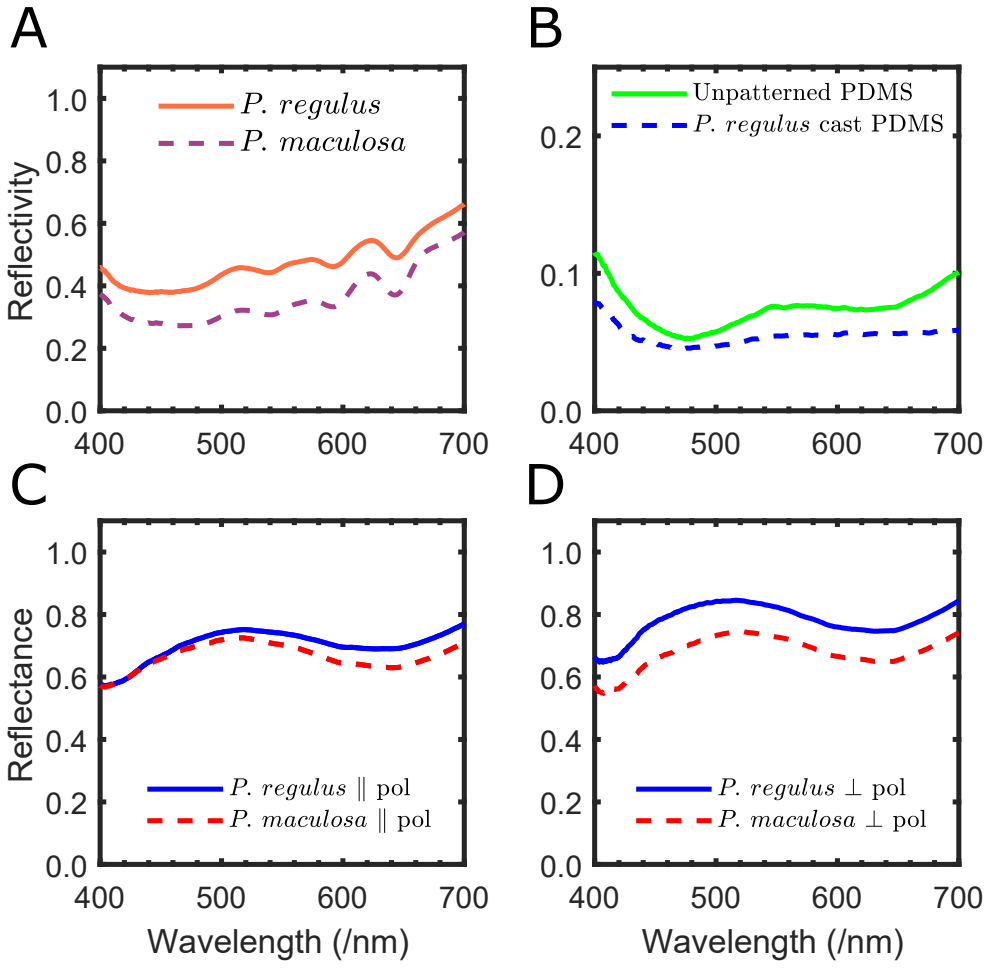

Fig. 6.7 A: measurement of the spectrum of the brown spots on the eggshells showing the presence of protoporphyrin. B: A PDMS cast of the surface of parasitic eggs does not show evidence of enhanced intensity with respect to a solid piece of PDMS. C-D: linear- and cross-polarisation measurement of the eggshells showing that the scattered light is more significantly enhanced (C) than the specular component (D).

2. Polarisation-dependent response: if the enhanced reflection from *P. regulus* is due to gloss and/or wax, the parallel polarisation channel would show a difference in the spectra of the two species while the difference would disappear in the cross-polarisation configuration. Conversely, if the enhanced brightness is due to scattering, this difference would appear in the cross-polarisation set-up but not in the parallel polarisation one. A linear polariser mounted on a rotation mount (Zeiss, 427710-9000) is placed in the illumination light of the microscope set-up described in the Experimental Section 3.1.1, while a second linear polariser (Thorlabs, WP25M-UB) is mounted in the collection path. Thus, by rotating the first polariser with respect to the other, one can acquire spectra in cross- and parallel-polarisation.

   As presented in Figure 6.7C-D, the difference between the two species is noticeably smaller in the parallel polarisation channel than in the crossed one.

The results of both experiments described above exclude the possibility that the intensity enhancement is due to an effect from a superficial nanostructure. Thus, the brightness of the *P. regulus* eggs is due solely to the increased density of air inclusions in the shells and to their size.

6.3 Conclusion

This chapter looks at the interplay between pigmentary and structural colour in the eggshells of three pairs of African avian species related to each other by brood parasitism. In particular, pigment purification by HPLC and analysis *via* mass spectrometry demonstrates that the blue pigment biliverdin is present in *P. regulus* eggshells. This is the first time this pigment is found in the Indicatoridae family suggesting that this species might have either developed or inherited from an ancient ancestor a mechanism to produce blue eggs as a response to the increased evolutionary pressure.

Furthermore, the inner structure of the eggshells is analysed in detail using advanced electron microscopy techniques showing the presence of air inclusions whose sizes are compatible with the wavelength of visible light. Disordered structures in the cross-section of the shells have never been reported before, as previous studies have focused on the surface patterning of the eggshells.

As a result of FIB tomography, the complete architecture of the eggshell is revealed, enabling the in-depth study of the light transport properties in the shells. A computational model representative of the air pores in *P. maculosa* and *P. regulus* eggshells explains why these differ in reflected intensity: both the efficient packing and smaller size of the inclusions

enhance the reflectance in *P. regulus*, which might be a biologically advantageous effect as it minimises the thickness needed to obtain a brilliant appearance. The spectral shape is however very similar, as a consequence of the presence of biliverdin.

This study brings together different branches of science, from behavioural ecology to chemistry and photonics, with multiple implications. On one hand, it successfully explains the mechanism behind the colouration of the eggshells. On the other, it opens various questions for future research: what is the biological role of the air inclusions? And, more specifically, is there an evolutionary advantage in having brighter eggshells? One hypothesis is that brighter eggs appear "healthier" to birds and thus elicit more parental care from the hosts, as suggested in various studies [226]. Another possibility is that the enhanced scattering reduces the amount of pigment necessary to achieve the same colouration, which may be advantageous if biliverdin pigment is limiting or its deposition involves some other costs to the mother or the embryo. At the present moment, the experimental limitations described above do not allow the measurement of the biliverdin concentration but it might be possible to address this hypothesis in the future. In addition, one could produce artificial eggs with pores of different sizes (*i.e.* eggs with different scattering strength) and test whether they are more or less likely to be rejected by the host species.

Lastly, it is not clear how the air inclusions form during the development of the eggs and what mechanism controls their size and spatial distribution: one can speculate that air is trapped inside during the formation of the shell and that the inclusions do not have the time to coalesce into larger ones. Another possible explanation is that small amounts of other organic compounds (*i.e.* lipids, protein, etc.) are responsible for the formation of the air inclusions during the biomineralisation of the eggshell - a phenomenon which has been shown to occur in analogous artificial systems [227]. In [228], a number of avian species from various continents show the presence of similar pores in the eggshells but no studies have yet addressed their role and formation, leaving space for further investigation. For example, the development of the eggshell could be tracked using techniques similar to those described in the previous Chapter in order to gain understanding of the materials and processes involved in the formation of the air inclusions. In addition, the structural role of the pores could be studied *via* mechanical and thermal testing to explore whether the optical effect is just a by-product of a structure which is, in fact, optimised for mechanical stability or for efficient management of external heat.

Chapter 7

The white beetle *Cyphochilus* - an inspiration and template for novel materials

The scales of the beetle *Cyphochilus* are the whitest natural material found in nature. This is due to the size and architecture of their scattering elements which have evolved to achieve the optimal combination of scattering parameters. The refractive index of the beetle's cuticle, however, is relatively low due to the constraints dictated by the materials available to living organisms.

By retaining the three-dimensional structure of the white beetle and substituting the constituent material with a higher refractive index medium, it is theoretically possible to break into the strong scattering regime and even achieve Anderson localisation.

In this chapter, two techniques to achieve such inversion are presented; both have been used in the past to produce highly-ordered photonic crystals [229] and rely on infiltrating the porous network of the beetle with strongly scattering materials such as titania (TiO_2), zinc oxide (ZnO), and silicon (Si).

The specimens prepared are then characterised by optical spectroscopy and electron microscopy with the assistance of focussed ion milling. Finally, the preliminary measurement of the scattering mean free path using the speckle autocorrelation function is discussed in relation to the samples fabricated.

7.1 Introduction

As introduced in Chapter 4, the scales of the white beetle *Cyphochilus* are the most scattering low-refractive index material known to date with a mean free path of (1.47 ± 0.07) μm [14]. The scales are made of chitin and cover the entirety of the beetle exoskeleton. The scales can be easily detached for analysis using a pair of tweezers. Each scale is roughly 20-30 μm wide and 100 μm long (Figure 7.1A,B). Their thickness has been measured to be between 5 and 10 μm [14]. By sectioning an individual scale using a scalpel and imaging the exposed cross-section with an electron microscope it is possible to see that, underneath the smooth surface that encases the scale, chitin is arranged in a complex and interconnected network of rods and voids, as illustrated in Figure 7.1C. The rod length, (1.1±0.4) mm, as well as their diameter, (330±160) nm, varies greatly from strut to strut. The overall filling fraction is (45±6)% [20][1].

The whiteness of the *Cyphochilus* beetle compared to other materials is striking both in terms of its intensity and wavelength-independence (with the exception of wavelengths around 400 nm where the reflectance is lowered by the presence of absorbing pigments). Figure 7.1D shows a direct juxtaposition of the reflectance spectra from various materials. The spectra are collected by optical microspectroscopy using a large numerical aperture (NA = 0.95): as light is scattered in a random direction when impinging on a disordered medium, it would not be collected by a microscope objective with a smaller angular range (see also Experimental Section 3.1.2).

The spectra are normalised using a white standard diffuser (LabSphere USRS-99-010) that scatters >99% of light. The diffuser is made of Spectralon®, a porous thermoplastic resin. Its angular performance has been tested to be Lambertian (that is, angularly isotropic [230]). The scattering in this material is thus engineered to provide a point of reference for other white materials but it is not in itself the most efficient scatterer: it is a few millimetres thick so that its scattering performance derives not only from the strength of each scattering event but is improved by having a large thickness so that multiple scattering events can occur.

Another example where it is the thickness that is responsible for the white appearance is the case of polar bear hairs (*Ursus maritumus*, hair borrowed from the Scott Polar Research Institute, Cambridge). The single hair is very close to being transparent as it is clear from its reflectance (Figure 7.1D). However, polar bears appear white to the naked eye as a consequence of having multiple layers of hairs superimposed on top of each other [231–233].

[1]Related publication: Wilts B. D., Sheng X., Holler M., Diaz A., GuizarSicairos M., Raabe J., Hoppe R., Liu S. H., Langford R., Onelli O. D., Chen D., Torquato S., Steiner U., Schroer C. G., Vignolini S., and Sepe A. (2017) Evolutionary optimized photonic network structure in white beetle wing scales. *Advanced Materials.*

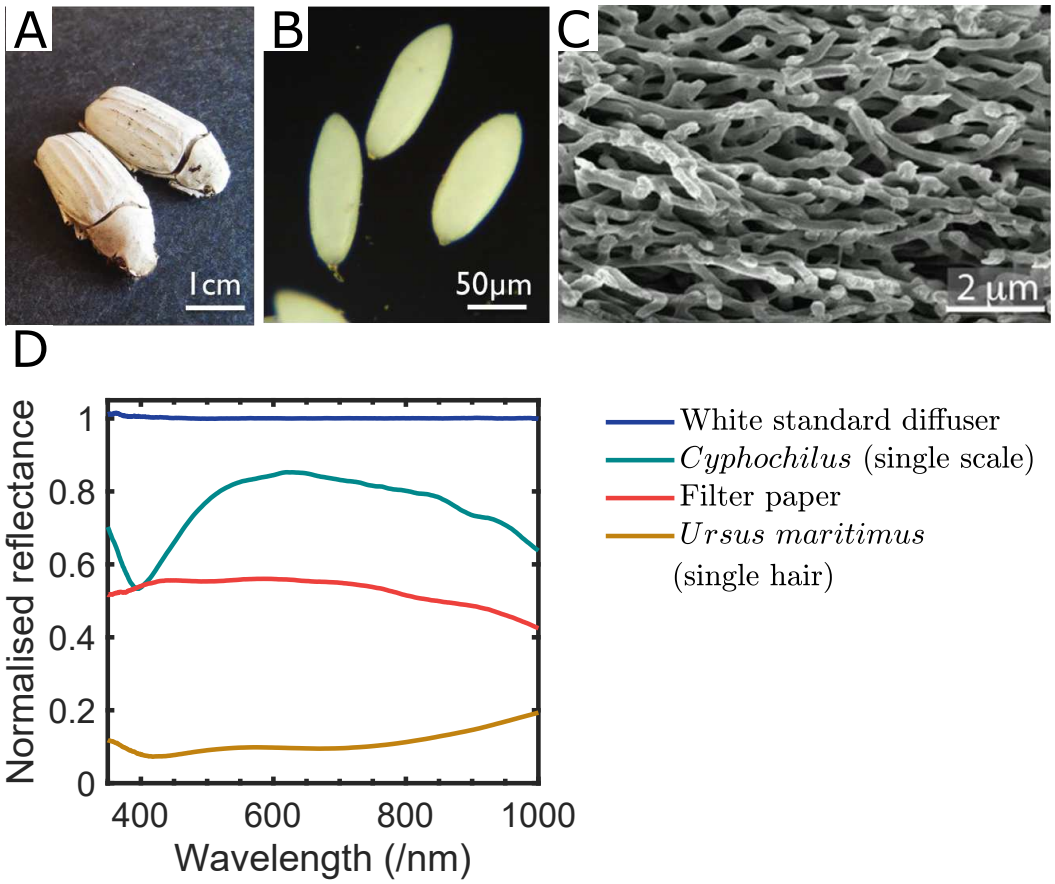

Fig. 7.1 A: photograph of two *Cyphochilus* specimens. B: dark-field micrographs of *Cyphochilus* scales (detached and mounted on a glass slide). C: the inner architecture of the scale shows an interconnected array of chitin filaments (SEM image adapted from [14] under CC-BY license). D: a comparison between a number of common white materials and the white beetle (NA in collection = 0.95).

Common white paper is also a random medium where the cellulose fibres are arranged in a disordered fashion producing scattering and thus whiteness. Figure 7.1D shows that the reflectance of standard filter paper (Whatman® Grade 1) is also lower than that of the beetle even though the thickness of the sheet is around 100 μm and the refractive index of cellulose is comparable to that of chitin. This is due to the fact that the cellulose fibres are not optimised for light scattering in terms of their size and spatial distribution [56], while the *Cyphochilus* scales are highly specialised.

To get an insight into whether evolution has in fact selected the best combination of scattering parameters (such as filling fraction, refractive index, etc.) to produce the whitest material possible, one can run computational simulations varying each parameter in turn and compare the predicted reflectance with the one measured from the beetle cuticle. To do so,

however, it is necessary to know the full three-dimensional structure of the random network with sub-micron resolution.

Due to the softness of the chitin network, this cannot be achieved by FIB milling which significantly affects the structure (see later discussion and Figure 7.3). Hence, advanced x-ray techniques have been used in [20] to image the structure. A custom set-up is used to overcome the resolution and field of view limitations of conventional x-ray tomography. In particular, a ptychographic technique is used to retrieve the data from the volume. Ptychography is based on scanning the sample using adjacent probes whose spots overlap significantly. The redundancy in the diffraction pattern can be then used to improve the reconstruction algorithm both in speed and in resolution [234–236]. In addition, the experiment is carried out at 92 K to prevent sample deformation.

Once the structure is known, it is possible to test numerically various parameters, as summarised in Figure 7.2. This is achieved using a Finite-Difference Time-Domain (FDTD) simulation, a technique also known as "Yee's method" after its inventor [237]. FDTD modelling relies on a grid-based approach: the structure of interest is divided into smaller regions (or "elements" - the simplest meshing consists of dividing the structure into small cubes). Maxwell's equations are solved at each element's boundary and propagated through the whole volume to obtain the complete solution. This method is extremely versatile and robust, providing a prediction of a medium's response in both time and frequency domains.

The first scattering parameter explored is the structure anisotropy and, in particular, the relationship between the network's orientation and its reflectance. As mentioned in Chapter 4, the white beetle structure is highly anisotropic, with the rods oriented mostly in-plane. This is further confirmed by the simulation where the reflectance differs by $\sim$20% for the two orientations (Figure 7.2A). In particular, the most reflective direction is the most biologically relevant (*i.e.* out-of-plane). This is an indication that the anisotropy in the system could be an evolutionary-favourable trait.

A further simulation also indicates the importance of the anisotropy: upon stretching (that is, making the structure more isotropic) the reflectance does not improve significantly. In other words, the beetle configuration guarantees a highly visible whiteness whilst using minimal thickness. In principle, the anisotropy can also be increased by compressing the structure but this leads to a decrease in intensity as a consequence of the reduced thickness and optical crowding [14] (Figure 7.2B).

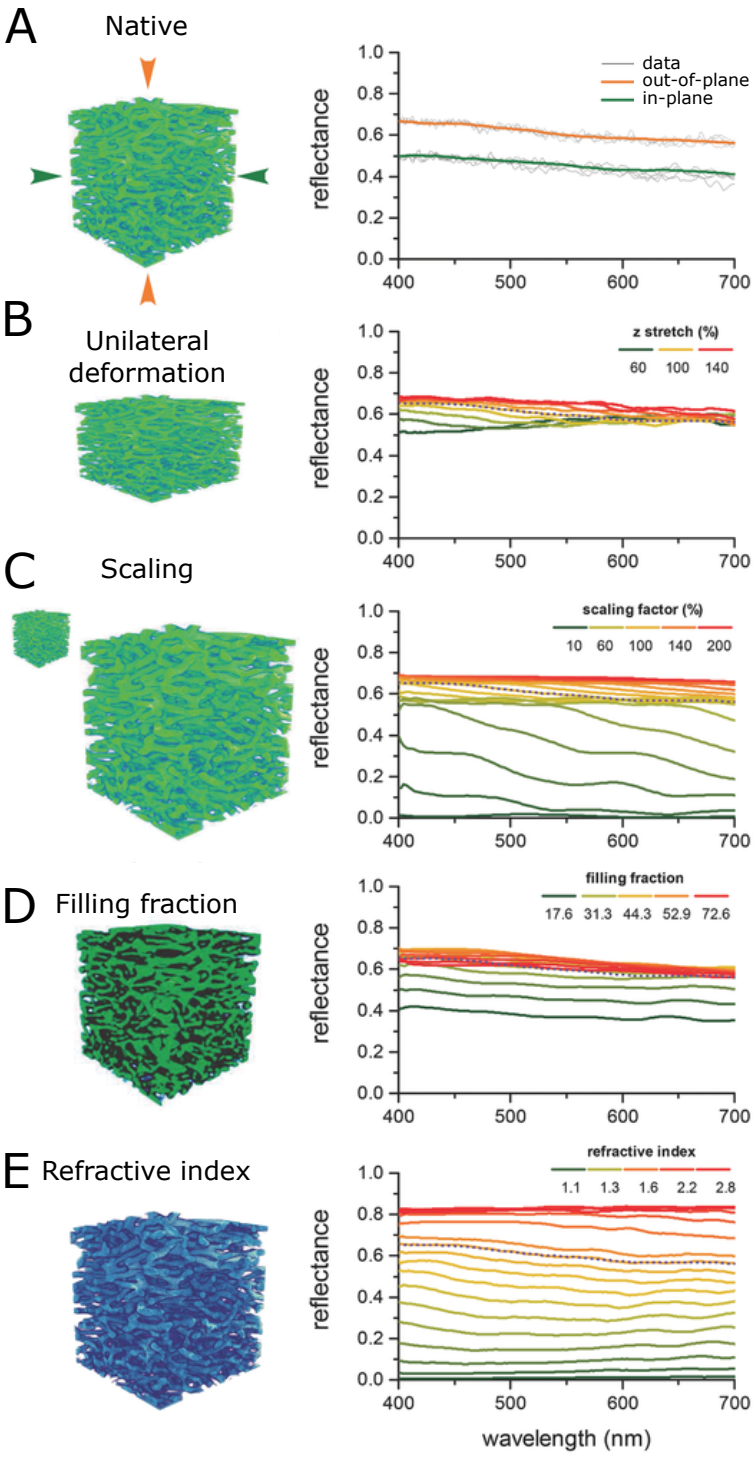

Fig. 7.2 Reproduced from [20] with permission from Wiley (2017). A-E: FDTD-simulated optical response for the *Cyphochilus* structure as a function of illumination direction (A), deformation (B), scaling (C), change of filling fraction (D), and refractive index (E).

Likewise, scaling up or down the structure does not promote strong scattering (Figure 7.2C). In fact, the reflectance decreases sharply when the thickness decreases, to the point that the scale would become transparent. However, scaling up the network does not improve significantly its performance either. Thus the beetle achieves the strongest whiteness whilst constraining thickness and amount of material used.

Similarly to the previous cases, increasing the filling fraction does not strongly affect the reflectance (Figure 7.2D). This observation suggests that the beetle cuticle is minimising the material used whilst achieving the strongest response - which would not be possible with a lower filling fraction.

The refractive index, however, is seen to strongly affect the scattering properties of the *Cyphochilus* beetle (Figure 7.2E). As expected, a low refractive index is not desirable for strong whiteness. In contrast, a high refractive index is optimal for enhancing white coatings. However, due to the limited availability of high refractive index materials in living organisms, the beetle is constrained in this direction: chitin's refractive index does not exceed 1.55-1.60 (depending on the wavelength) [148].

Artificially, however, it is in principle possible to substitute the chitin component of the network with a higher refractive index material such as titania or silicon whilst retaining the optimised architecture of the beetle.

In this chapter, two approaches based on the use of the *Cyphochilus* beetle as a template for producing strongly scattering high-refractive index materials are introduced. The first relies on coating the chitin rods with a thin layer of TiO_2 and then removing the original polymer, while the second consists in a double-inversion process to produce silicon-based structures. The samples fabricated using these two methods are then characterised microscopically and spectrally to assess the effect of the enhancement in reflectance. A direct estimation of the change in scattering mean free path is, however, more difficult and a few techniques are discussed at the end of the chapter.

7.2 Results and discussion

The first step towards either the thin-shell titania coating or the double-inversion of the beetle network methods is exposing its inner structure. In other words, the smooth chitin surface that encases the random structure needs to be removed to access the interior in order to deposit other dielectric materials in the air gaps.

Initially, FIB milling is used to separate the upper surface from the random network. Multiple cuts using a low ion current allow the selective removal of the upper surface. Figure 7.3A shows a scale where the process has been carried out by cutting five rectangular sections

from the surfaces using the current and voltage parameters described in Experimental Section 3.2. The porous structure has, however, been partially damaged in the process: FIB milling is not a suitable technique for this material due to the high degree of porosity of the latter (Figure 7.3B). In addition to the beam damage, the process is slow - taking up to a few hours to open each scale - and expensive.

Better results are obtaining using a plasma etcher to selectively remove the upper chitin lamina [238]. It is found that a mixture of 20% Oxygen (O_2) and 80% Argon (Ar) is effective in the removal of the upper membrane if applied for 9-10 minutes. An example of a scale open using plasma etching is shown in Figure 7.4B (see Appendix C for the experimental details).

Plasma etching offers a number of advantages as compared to FIB milling: it is a fast technique that allows the opening of hundreds of scales at the same time. It is not as locally accurate as FIB cutting but it is less invasive and it does not damage the sample. Once the scales are open it is possible to infiltrate them using various materials.

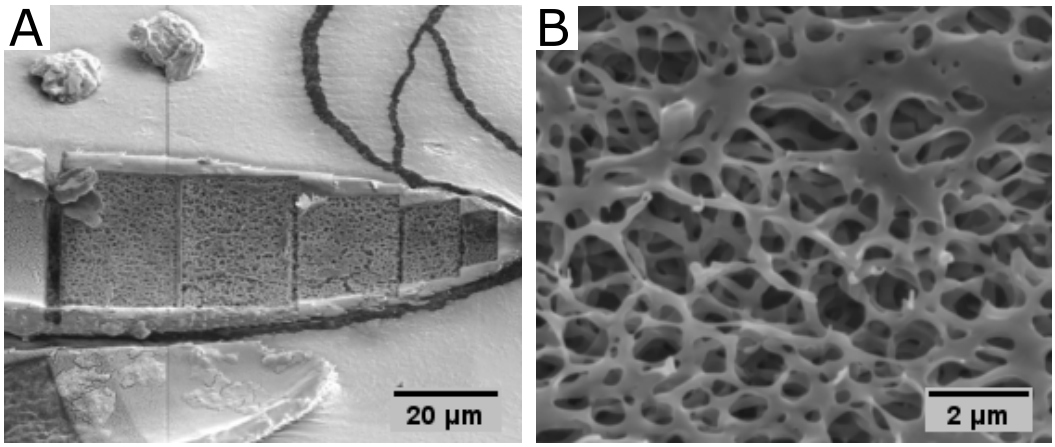

Fig. 7.3 A: a *Cyphochilus* beetle scale where the inner structure has been opened by performing 5 rectangular sections *via* FIB milling. B: enlargement of an exposed area showing the damage caused by the ion beam.

In order to obtain a TiO_2 replica of the structure, the open scales are covered with a TiO_2 layer. Then, the chitin component can be removed by calcination (*i.e.* by heating up the samples in a controlled atmosphere). The process is summarised in Figure 7.4A. This method is based on [229] where a TiO_2 thin shell (about 10-20 nm in thickness) is formed by atomic layer deposition (ALD) on polymeric templates obtained by direct laser writing (DLW) lithography. The polymer is then removed by heating the sample up to 480°C. The polymer removal causes shrinkage of the TiO_2 network which thus formed a ultra-low density network. The resulting structure is then coated with a layer of amorphous silicon of the desired thickness [229, 239].

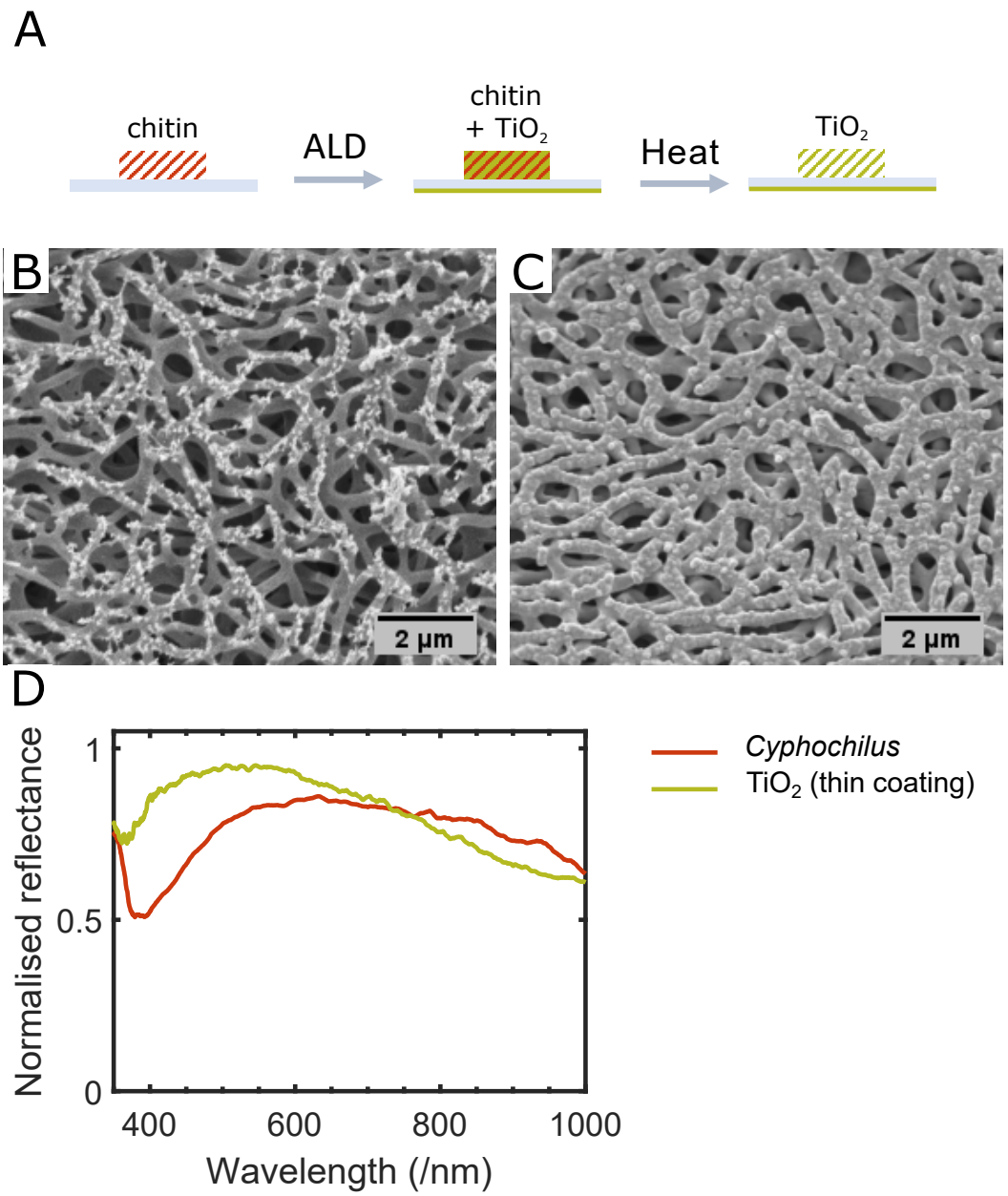

Fig. 7.4 A: schematics of the thin shell coating process where the chitin structure is first coated with a thin layer of TiO_2 and then heated to remove the initial polymer. B: top-view of a scale opened using plasma etching. Some debris is present on the surface. C: the same scale after TiO_2 deposition and calcination. D: reflectance of the samples before and after the thin coating procedure (collection NA = 0.95).

In the case of the *Cyphochilus* scales, 16 nm of TiO_2 are deposited on the chitin network (for the specific parameters see Appendix C). The procedure produces a uniform thin layer of titania, as shown in Figure 7.4B,C.

After calcination at 480°C, however, the structure is not seen to shrink as expected. Even when the heat treatment is prolonged to more than ten hours, the structure is not observed to change. This result is surprising if one considers that the thermal gravimetric analysis (TGA) of chitin fibres shows the onset of decomposition at 158°C and degradation of up to 50% of the starting material at 353°C [240]. However, a plausible explanation is that the chitin fibres degrade rather than melt at high temperatures. This is in contrast to the behaviour of photo-resists whose thermoplastic properties lead to shrinkage during the annealing phase [241].

As a consequence of the lack of shrinkage, it is not possible to continue the procedure as presented in [229] because the resulting structure would have a very high filling fraction and thicker features than those needed for enhanced scattering in the visible range. The samples produced are, however, uniform in coating and reproducible - showing the possibility of fabricating a porous random network of titania. Therefore their optical response is further investigated using optical microspectroscopy: in Figure 7.4D it is possible to see that the titanium dioxide-based sample has a higher reflectance than the original *Cyphochilus* scale. The enhancement is greater for the shorter wavelengths (400-600 nm) while at longer wavelengths the signal decreases, most probably due to dispersion of the titania refractive index which varies from 2.68 for wavelengths around 400 nm to 2.31 at 1000 nm [149].

It can be concluded that the thin titania shell is a viable approach but it requires further exploration in order to be optimised for chitin templates and to be extended with the use of silicon as the final material for applications in the infrared.

As the titania shell method does not yield the desired results, a double-inversion process is attempted (summarised in Figure 7.5A). The first report of this kind of double-inversion method is in the context of photonic crystals where a "woodpile" structure produced by DLW is inverted twice to obtain a replica in silicon (high quality hydrogenated amorphous silicon, a-Si:H) [242].

Similarly, open *Cyphochilus* scales are opened to expose the random network for infiltration. The first step is to deposit a thick layer of zinc oxide (ZnO) until the air gaps in the structure are filled. TiO_2 can also be equivalently used but the slow deposition rate for this set-up would prolong the process.

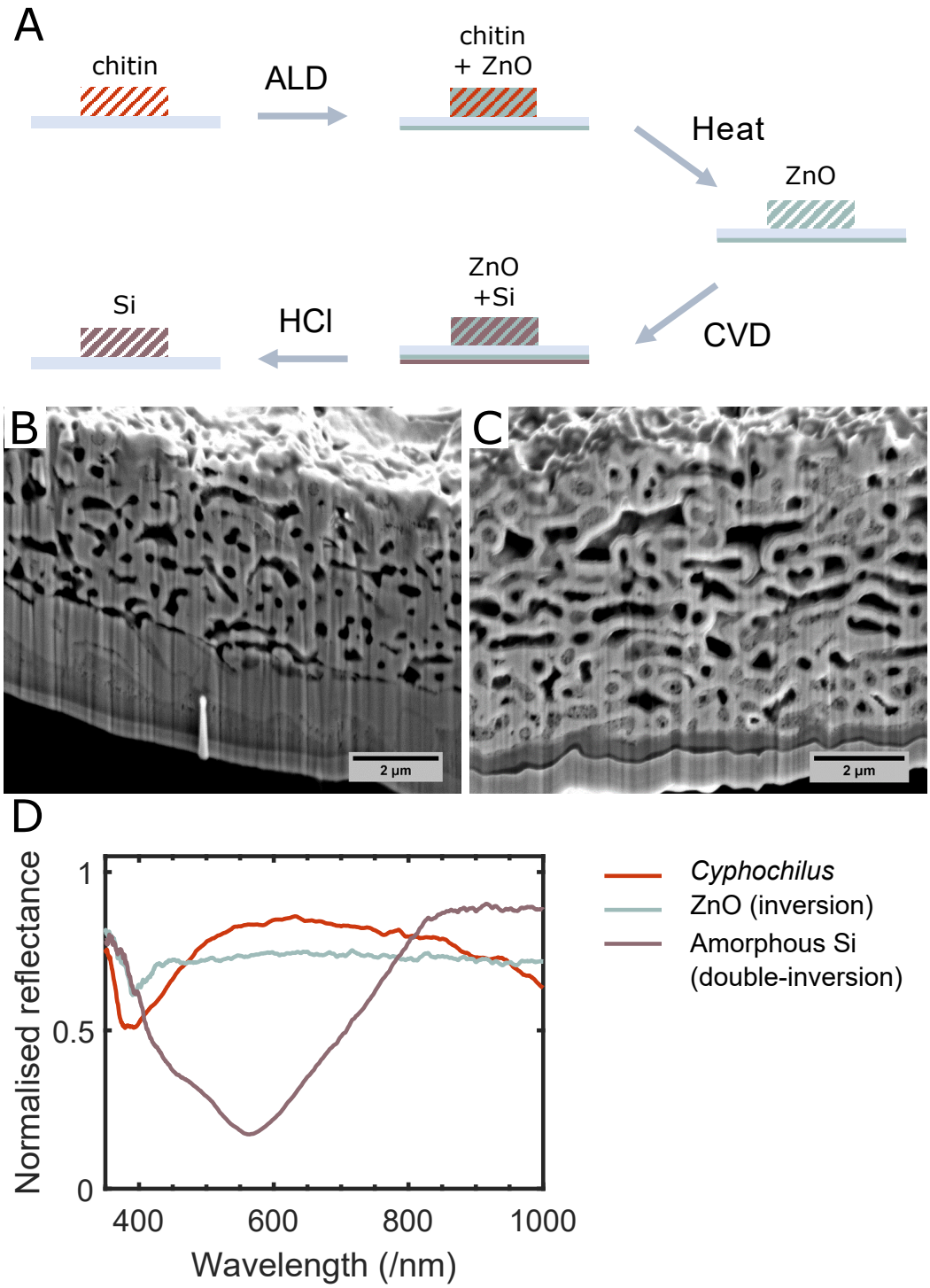

Fig. 7.5 A: schematics of the double-inversion process whose chitin network is first infiltrated with ZnO and then with Si. B: cross-section of a scale after the ZnO deposition and heat treatment. C: the amorphous silicon starts to diffuse through the ZnO network (dark grey areas *versus* light grey areas). D: the reflectance of the samples at different stages of preparation (collection NA = 0.95).

As mentioned earlier, the gaps vary greatly in size and therefore a coating of at least 800 nm is needed to ensure that even the larger spaces are filled. This is achieved, however, at the expense of overfilling the smaller gaps so that, by the end of the procedure, the structure is covered by a ZnO layer on the top surface as well as underneath the sample holder (a calcium fluoride slab, CaF_2). This shortcoming can be remedied by removing the superfluous layer *via* plasma etching. The etching is carried out in a step-wise fashion, incrementing the plasma time until inspection by SEM confirms that the upper layer has been removed (typically over 6-8 hours).

At this point the original chitin framework can be removed by heat treatment (420°C for 4 hours). In Figure 7.5B it is possible to see that the ZnO has indeed filled the air gaps and, by removing the chitin, the structure obtained is the inverse of the original - as shown by FIB/SEM inspection. In fact, in this case it is beneficial that the chitin does not shrink at high temperature as, in this way, the photonic network features are preserved in size.

The scattering from this ZnO structure is not optimal: the filling fraction is now about 55% (*i.e.* the inverse of the beetle's) which can lead to optical crowding, especially for materials that have high refractive indexes such as ZnO ($n \sim 1.93$ for visible wavelengths [150]). It is nonetheless interesting to see that the optical response is almost perfectly flat (*i.e.* wavelength-independent) for this inverse structure (Figure 7.5D) as consequence of the weak dispersion of the zinc oxide's refractive index.

The next step is the deposition of silicon using chemical vapour deposition (CVD). The silicon phase should completely fill the space that is originally occupied by the chitin so that the silicon thin film should be at least 400-450 nm in thickness. This implies that a thin layer of excess silicon will cover the structure and its substrate after the procedure. The upper layer can again be removed by careful plasma etching in conjunction with SEM inspection. The bottom layer is removed together with the ZnO inverse structure *via* wet etching with hydrochloric acid (HCl, added drop-wise).

The optical characterisation of the structure shows a wide absorption dip in the wavelength region between 400 and 800 nm (Figure 7.5D), as expected for amorphous silicon [243]. More interestingly, the reflectance for longer wavelengths is well above 90%, confirming that this materials has promising applications in the infrared wavelengths.

In Chapter 2.3.1, the scattering mean free path, l_s, has been introduced as a parameter for the evaluation and comparison of the performance of white materials. Three main techniques for the measurement of l_s are discussed: the integrating sphere, the speckles autocorrelation, and the backscattering cone. In the case of the *Cyphochilus* scales it is extremely challenging to evaluate l_s for a number of reasons.

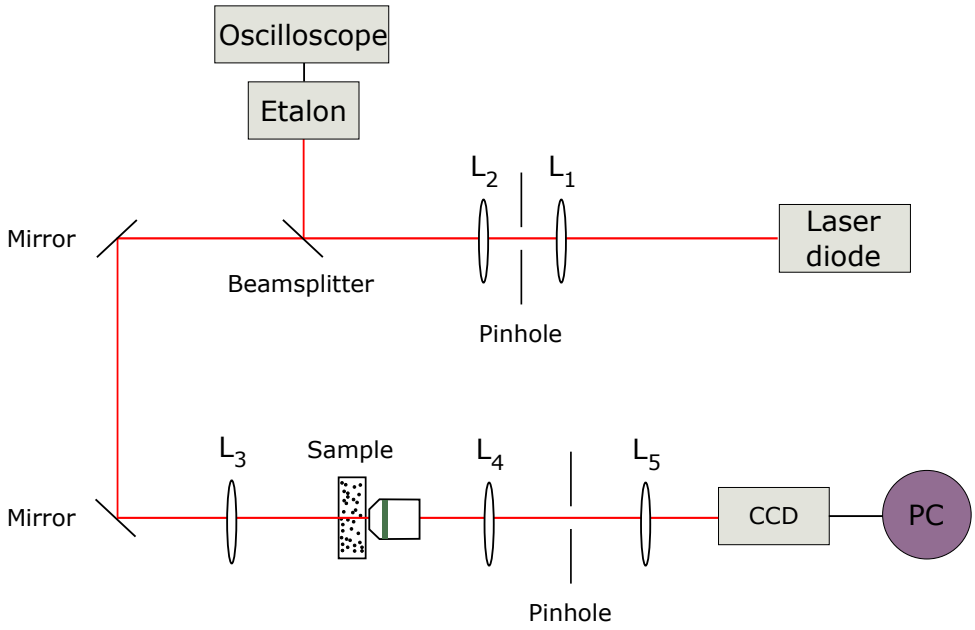

Fig. 7.6 Block diagram representing the set-up for the speckles autocorrelation experiment. The laser beam is first expanded by lenses L_1 and L_2 (the pinhole acts as a spatial filter for cleaning the beam) and then focused on the sample using lens L_3. A microscope objective with a large NA is used to collect the speckles at the other end of the sample. Lens L_4 and the second pinhole act as a Fourier-space filter. Finally, lens L_5 focuses the speckle pattern on the CCD which is connect to a computer. The laser frequency is tuned by changing the temperature of emission and measured by the oscilloscope *via* an etalon (or Fabry–Pérot interferometer).

First of all, the scales are available only in their native thickness, meaning that integrating spheres measurements of the scattering mean free path are not possible as these require having specimens of different thickness to perform a linear fit.

The backscattering cone approach also poses serious challenges as the scattering mean free path is expected to be very short. In fact, the scales are thin compared to the scattering mean free path implying that only a small number of scattering events occurs in each scale. The enhancement of the intensity in the backscatter direction is the result of the interference of multiple light paths and it is therefore not very noticeable if constituted only by very few scattering events. In addition, the single scales are just tens of micron wide and thus it is necessary to use a very small illumination beam for the experiment. This implies that the probability of having long scattering paths is very small and therefore the peak of the cone will not be as sharp as predicted in the ideal case making it difficult to detect.

As a consequence, the autocorrelation method is chosen to carry out the analysis. It is difficult to measure the signal from a single scale due to its small lateral dimensions, but this can be overcome by mounting the scale on a non-scattering transparent surface (*e.g.* a glass

sample holder) and slide the sample in front of the illumination path: when a speckle pattern is detected, the scale is in focus. Conversely, when the laser beam is illuminating the glass slide, no pattern will be seen as light propagates ballistically though glass.

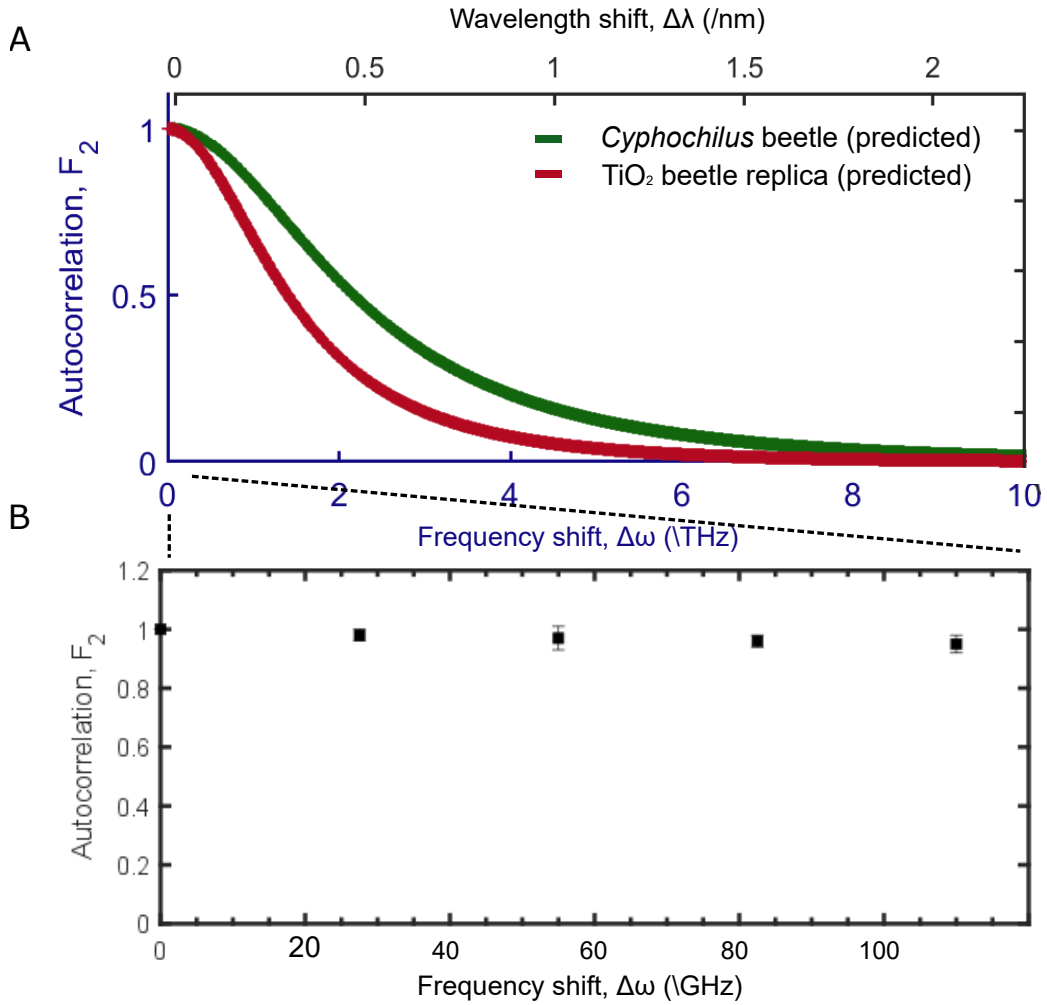

Fig. 7.7 A: simulated autocorrelation function for the *Cyphochilus* beetle and the TiO_2-coated replica as a function of frequency shift (bottom x-axis) and wavelength (upper x-axis). The thickness of the sample is assumed to be 8 μm and its refractive index 1.56 for the beetle and 2.4 for TiO_2, the model is based on Equation 2.54. B: experimentally measured autocorrelation function for the titania shell beetle replica. F_2 is fairly constant over the probed range. Hence, it is not possible to obtain an estimation of l_s.

Figure 7.6 shows a set-up for the analysis of the correlation between speckles patterns. The light source is a laser diode whose frequency can be finely tuned (see later discussion). The beam is expanded and spatially filtered (*i.e.* cleaned of artefacts) by a lens-pinhole system (L_1 and L_2 in Figure 7.6). Then, a 50:50 beam splitter divides the beam path into two branches. One branch is used to monitor the output frequency of the laser by analysing

the light beam with an etalon (also known as Fabry–Pérot interferometer) which acts as an optical resonator. The signal transmitted through the etalon varies periodically as a function of the laser's wavelength and can be measured with an oscilloscope to detect the periodic oscillations and thus infer the laser's frequency.

The second branch of the light path is aligned so that to illuminate the sample at normal incidence *via* the adjustment of the two mirrors. Lens L_3 focuses the beam on the specimen and a microscope objective with a large NA collects the transmitted information. The signal is filtered in Fourier space by a pinhole mounted in the Fourier plane of lens L_4. Finally, the speckle pattern is focused on the CCD and transmitted to a computer which collects the images.

The autocorrelation method consists of recording images of the speckle pattern for a sample as the laser frequency changes. Each pattern must be associated to the exact same sample position or the result will not be accurate. Once multiple images are collected (typically, more than one image is collected for each frequency to reduce errors), it is possible to analyse them and plot their correlation as a function of the frequency shift (Figure 7.7B).

As predicted by Equation 2.54, the correlation function F_2 decays very slowly with the frequency shift, due to three factors: the short scattering mean free path, the small thickness, and the low refractive index. In practice, the computational simulation shows that the required frequency range spans several terahertz. This implies that, in order to be able to correctly interpolate the function F_2, it is necessary to utilise a laser whose wavelength is tuneable in steps of about 0.01 nm whilst covering a range of 1-2 nm in total.

This frequency requirement is hard to meet using currently available lasers. On one hand, most super-continuum laser sources are characterised by wavelength steps about 1 nm which would not be able to resolve the first part of the curve in Figure 7.7A. On the other hand, tuneable laser diodes usually have much finer steps ($\sim$GHz) but are not able to sweep such a large frequency range. As shown by the experimental data in Figure 7.7B, a laser with step size equivalent to 27.5GHz is only able to probe the very first part of the curve which is not sufficient to extrapolate l_s. A possible solution would be to use a laser for telecommunications, as this type of device has the required wavelenght span and step-size [244].

7.3 Conclusion

This chapter revolves around two main concepts: the extraordinary scattering properties of the white beetle *Cyphochilus* and the methods to use its scales as a template for the fabrication of novel materials.

The genus of *Cyphochilus* beetles is shown in the literature to be the whitest low refractive index material: compared to similar materials the optical response is intense and wavelength-independent. As the bettles exploit their colouration to camouflage amongst white *fungii* [14], such strong scattering optimisation might be the result of the evolutionary pressure that leads towards obtaining the whitest coating for camouflage whilst using the minimum amount of material, as demonstrated by FDTD simulations. However, it could also be argued that the structural requirements for minimal material usage are driving the evolution of the *Cyphochilus* and the enhanced whiteness is a by-product of such process. As fossil evidence is absent for these white beetles, it is not possible to perform a direct evolutionary investigation. Nonetheless, it would be possible to perform a similar simulation study of the mechanical stability of the chitinous network when subjected to analogous changes (*e.g.* unilateral deformation, scaling, etc) and assess whether the structure is, in fact, mechanically optimised.

In particular, as the beetle has limited access to high refractive index-materials, it is the nanostructure of the scales that strongly enhances the scattering. The recent advances in the field of x-ray microscopy have made it possible to observe the full three-dimensional arrangement of the fibres and understand what features are the most important towards the optical properties of the white beetles.

By combining the optimised architecture and shape of the scattering elements in the *Cyphochilus* beetle with highly scattering materials one can improve upon the beetle's performance. This can be achieved by using both single- and double-inversion techniques. The two techniques described in this chapter lead to the production of titania- and silicon-based replicas of the random chitin network. In both cases, the procedures are complex and involve a number of steps that will require further optimisation in the future. However, the preliminary results presented here show the proof that such techniques are viable towards the production strongly scattering materials and constitute a possible route to the realisation of Anderson localisation in a three-dimensional volume.

In addition, it has to be pointed out that the characterisation of such strongly scattering specimens compels the research in this field to the boundary of the available experimental techniques. Due to the microscopic dimensions and short mean free path of the scales, the current methodologies are not suitable and further studies in this direction are needed - especially in terms of range and sensitivity of tuneable lasers for carrying out measurements of the scattering mean free path.

Another limitation of the method presented here is that the use of the white beetle as a template, whilst suitable for testing theoretical concepts in the field of multiple light scattering, is not a viable fabrication route for industrial applications. In the next chapter, a

scalable method for producing *Cyphochilus*-inspired white materials starting from cellulose, the most abundant natural polymer on the planet [245], is described.

Chapter 8

Anomalous diffusion of light in white beetle-inspired cellulose nanofibril membranes

The understanding of the interaction between light and complex, random structures is key for designing and tailoring the optical appearance and performance of many materials that surround us, ranging from everyday consumer products, such as those for personal care, paints and paper, to light diffusers used in LED-lamps and solar cells. This chapter aims to demonstrate that light transport in membranes of pure cellulose nanofibrils (CNF) can be controlled to achieve bright whiteness in structures only a few microns thick[1]. This is in contrast to other materials, such as paper, which require hundreds of microns to achieve a comparable appearance. The diffusion of light in the CNF membranes is shown to become anomalous by tuning the porosity and morphological features. Considering also their strong mechanical properties and biocompatibility, white coatings are proposed as a new application for cellulose nanofibrils[2].

8.1 Introduction

Whiteness is achieved when light is elastically scattered multiple times in random media, as explained in Chapter 2.3. In general terms, the higher the number and the strength of the

[1]This work has been accepted for publication as: Onelli', O. D., Toivonen', M. S., Jacucci, G., Lovikka, V., Rojas, O. J., Ikkala, O., and Vignolini, S. Anomalous Diffusion-Assisted Brightness in White Cellulose Nanofibril Membranes. Advanced Materials (2018). 'These authors have contributed equally to this work.

[2]Patent filed: Vignolini, S., Toivonen, M. S., Onelli, O. D., and Ikkala, O. Highly scattering porous material based on fibrillar, elongates, or disk-like particles.

scattering events, the brighter the material appears [246]. This simple principle explains why many commercially available white products, such as paints and sun creams, are typically formulated with high refractive index nanoparticles (*e.g.* TiO_2) as scattering enhancers [247]. The use of such promoters improves the scattering efficiency of the material, and therefore reduces the volume required to obtain fully opaque white coatings. However, the widespread use of TiO_2 particles as scattering enhancers, for example in food, cosmetics, and paper, has recently raised serious health and environmental concerns [248, 249]. Therefore, there is a real need to improve scattering efficiency using more sustainable and biocompatible materials [56, 39].

In the previous chapter it has been shown how scattering is optimized in the white beetle *Cyphochilus* by the intricate design of the morphology and the spatial arrangement of the scattering elements [135, 151, 14]. Dense random networks of nanofibres allow efficient packing and represent a particularly convenient strategy to optimize brightness in thin coatings due to the intrinsic polydispersity and anisotropy of the scattering elements. Fibrillar nanomaterials, such as cellulose nanofibrils (CNF), are therefore promising candidates due to their inherent morphology. Furthermore, their excellent mechanical performance, wide availability, renewability, and biocompatibility provide additional benefits of choosing such fibres [250–254]. However, paradoxically, research on the optical properties of CNF-based materials has focused on the optimization of their transparency [255, 256]. Therefore, the possibilities of using CNF to construct an efficient scattering medium have not been explored, although recently their potential for high-haze diffusive optical elements for optoelectronic applications has been recognized [257].

A scalable and versatile approach for light management in CNF membranes is presented here. By inducing appropriate porosity and tuning the size distribution of the CNF in the membranes, it is possible to modify their nanostructure and easily produce membranes with completely different optical appearance: from thick, highly transparent membranes to thin, bright white ones. The produced membranes are mechanically stable as they retain the amorphous domains and hemicelluloses of natural cellulose fibres, in contrast to films based on cellulose nanocrystals which are significantly more brittle [56, 258]. Finally, it is observed that light transport in strongly scattering CNF membranes unexpectedly undergoes anomalous diffusive behaviour.

8.2 Material fabrication

The membranes are prepared by Matti S. Toivonen (Aalto University). Membranes with different scattering properties are obtained by fractionating a CNF dispersion with a wide

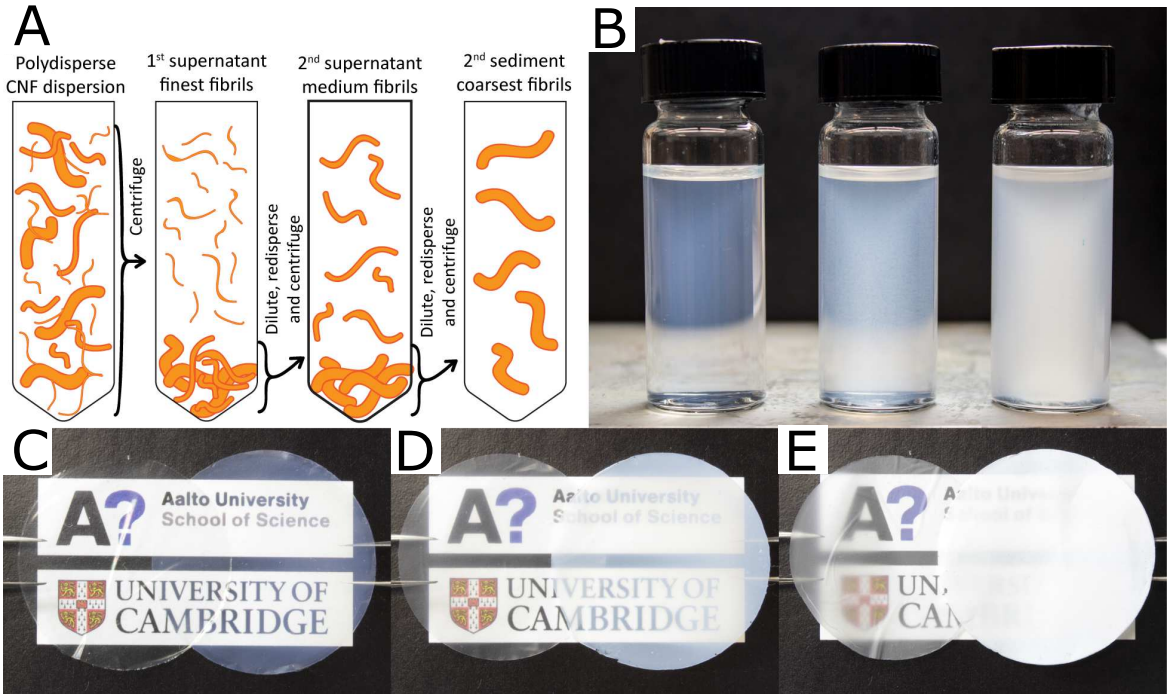

Fig. 8.1 A: schematic diagram of the differential procedure to separate the various CNF fractions. B: the turbidity of the solutions increases with the increasing size of the fibrils from the finest (leftmost) to the coarsest (rightmost). The concentration is the same in all images (0.9 g/L). C-E: the membranes that are dried directly from water (on the left in each photograph) appear transparent as they lack the porosity of the membranes dried from octane (on the right) whose opacity increases with the fibrils' size going from the finest (C) to the coarsest (E). Images courtesy of Matti S. Toivonen.

distribution of fibril diameters *via* a sequential centrifugation procedure, as schematically illustrated in Figure 8.1A. The finest fibrils (*i.e.* smallest diameters) are first isolated from the original CNF dispersion by repeated centrifugation, collection of the supernatant, dilution, and homogenization. Subsequently, the same procedure is repeated at a lower centrifugal speed in order to isolate a dispersion of slightly thicker fibrils, which is referred to as "medium fibrils" in the rest of the text. Finally, the sediment is collected, diluted and homogenized. The fibrils in this last dispersion are referred to as "coarsest fibrils" in the following discussion. The presented sequential centrifugation process results in the three dispersions of fibrils (Figure 8.1B).

For a fixed concentration, the turbidity of the dispersions correlates with the expected average fibril size. The distribution of the fibril diameters for the three dispersions are estimated by Atomic-Force Microscopy (AFM, Figure 8.2) By measuring the diameters of more than 500 fibrils of each dispersion, it becomes apparent that their distributions follow, in first approximation, a log-normal statistics with a long tail, especially for the coarsest

fibrils. The mean (and respective standard deviation) of the log-normal distributions of the fibril diameters in the three dispersions are 4.2 (2.7), 5.6 (3.2), and 19.5 (13.2) nm, going from the finest to the coarsest fibrils.

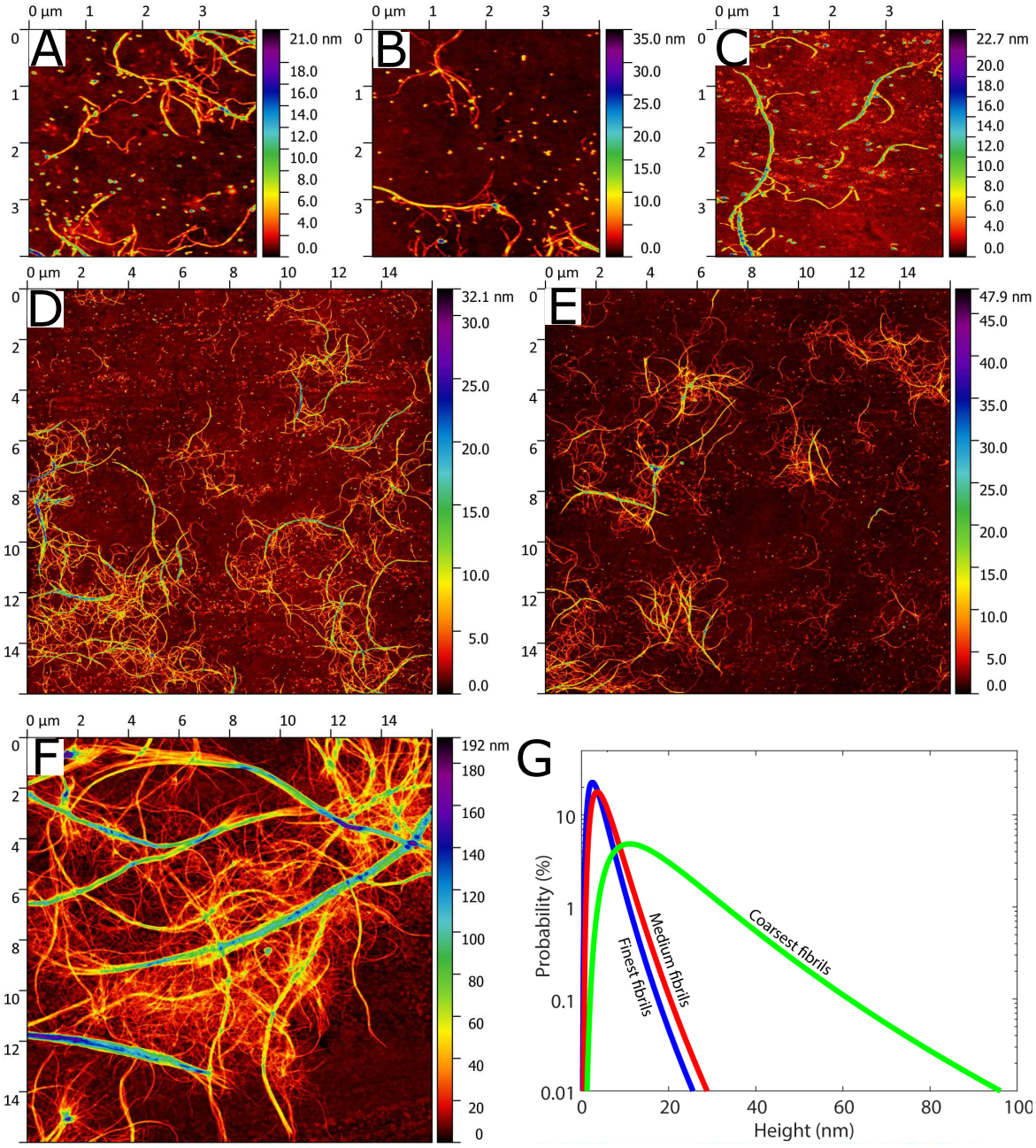

Fig. 8.2 AFM micrographs. A-C: finest fibril. D-E: medium fibrils. F: coarsest fibrils. G: the fibrils populations vary considerably in size and polydispersity. Measurements by Matti S. Toivonen and Ville Lovikka. Images courtesy of Matti S. Toivonen.

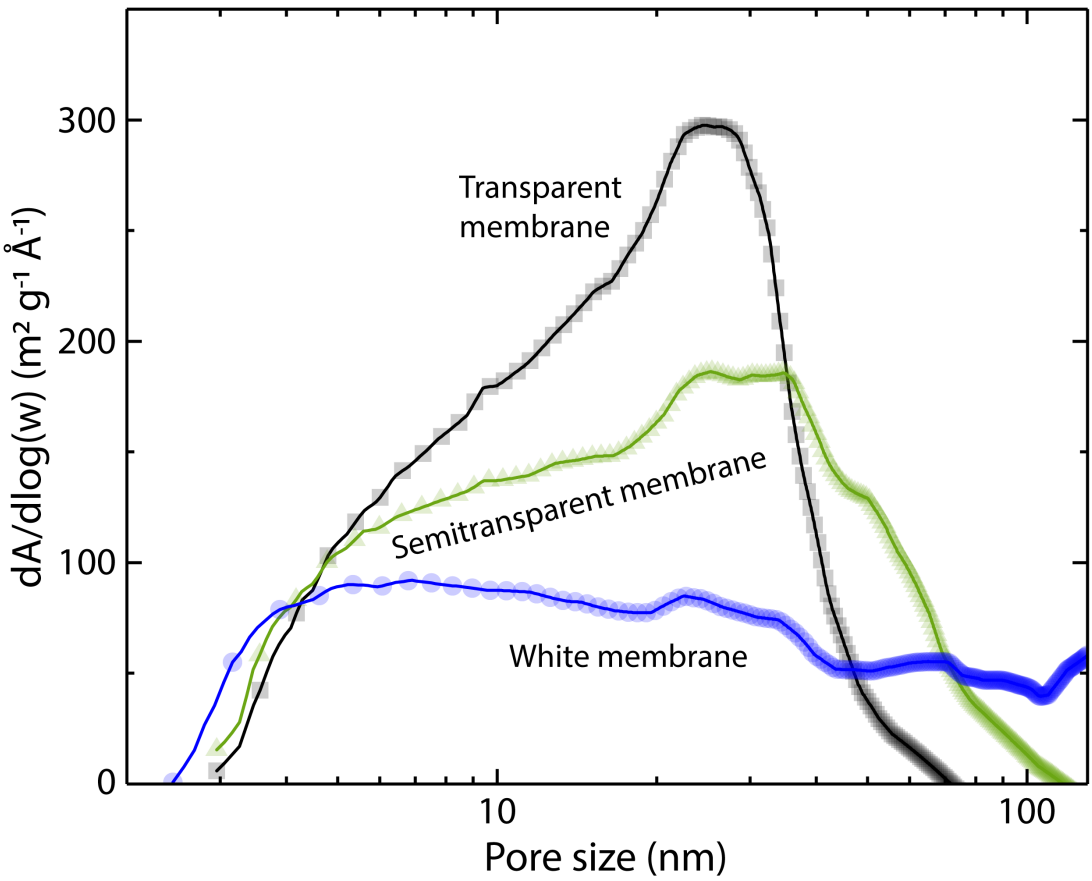

Fig. 8.3 The width of the pores varies greatly between the transparent and white membranes. The model assumes cylindrical pores. Measurements by Matti S. Toivonen and Ville Lovikka. Images courtesy of Matti S. Toivonen.

Porous membranes from the fractioned CNF dispersions are then prepared as described in an earlier work [259]. In summary, the dispersion is vacuum filtered into a wet gel cake, followed by solvent exchange from water to 2-propanol, and further to octane, after which the gel cake is slowly dried in ambient conditions. Photographs of the resulting porous membranes of equal thickness ($\sim$10 μm) prepared from the dispersions of the finest, medium, and coarsest fibrils are shown in Figure 8.1C-E (right). The membranes prepared from the finest, medium, and coarsest fibrils are referred to as the "transparent", "semi-transparent", and "white" porous membranes, respectively.

The solvent exchange step is crucial for the porosity, and the consequent whiteness. For comparison, dense CNF films prepared from an equal volume of the corresponding dispersions which have been dried directly from water without the solvent-exchange process are displayed in Figure 8.1C-E (left). The thicknesses of the dense, water-dried films are approximately half of those of the porous, octane-dried membranes, while the masses and

lateral dimensions of the samples are nearly the same, indicating that the density of the films dried from water is approximately double of the porous membranes dried from octane.

The reason for the densification of the CNF films upon drying from water is the combination of the capillary pressure of the evaporating water and the disruption of the hydrogen bonding network at the intersections of fibrils by water [260, 261]. When the solvent is exchanged to octane, the hydrogen bonding network between the fibrils is no longer disrupted by the solvent and the fibrils can be considered physically cross-linked, thus allowing the microstructure to resist the capillary pressure without collapsing [259, 262, 263].

The densities of the porous membranes are comparable and in the range (0.81 ± 0.16) kg/m^3. However, the porosity characterization by nitrogen physisorption revealed a different distribution of pore sizes. The transparent membranes show the highest specific surface area (190 ± 4) m^2/g and smallest pores, followed by the semi-transparent membranes with a lower specific surface area (175 ± 6) m^2/g and slightly larger pores, while the white membranes show the lowest specific surface area (122 ± 3) m^2/g and the largest pores. The pore size distributions are shown in Figure 8.3.

8.3 Results and discussion

Total reflection spectra for the three types of membranes at a thickness of approximately 9 μm are reported in Figure 8.4A. The white membrane – which is only 9 μm thick - notably exhibits a high broadband reflectivity (60-80%) for most of the visible range, reaching up to 90% for the shorter wavelengths, with a wide-angular scattering distribution (Figure 8.4D). To fully characterize light transport in such systems, the total transmittance is measured as a function of the sample thickness (Figure 8.4B). Figure 8.4C shows that the light transport in the transparent membrane can be described by diffusion approximation theory, with a scattering mean free path of about (13.5$\pm$0.5) μm (still twice better than the value used for commercial paper which is approximately 25 μm [14]).

Surprisingly, the diffusion approximation, which generally describes the behaviour of the majority of scattering materials, fails to describe the data obtained for the other two membranes. Therefore, to explain the experimental results the extended formalism has been adopted, describing light transport in super-diffusive and sub-diffusing systems as presented in Chapter 2.3.

In Equation 2.51, α is the parameter that describes the diffusion behaviour and A is a constant which depends on the scattering mean free path, the extrapolation length and the absorption (the latter is negligible for cellulosic fibres [264]). The data for the transparent samples is nicely fitted with $\alpha = 2$ (*i.e.* normal diffusion), while those for the two other

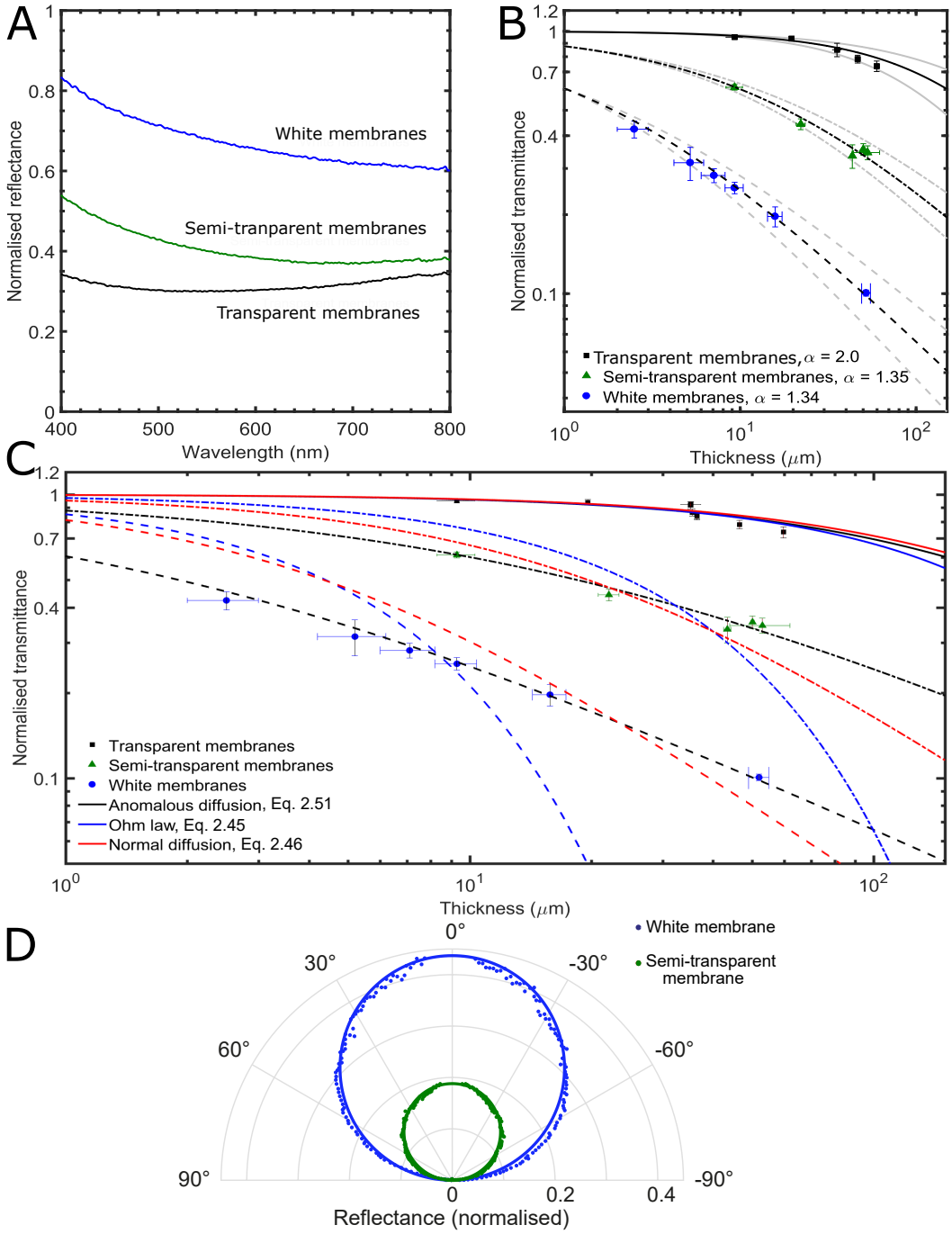

Fig. 8.4 A: total reflection of the membranes versus incident wavelength. B: total transmission versus thickness fitted according to Equation 2.51 (black lines - the grey lines represent the confidence interval). C: fits using two alternative approaches do not satisfactorily describe the transmission through the white and semi-transparent membranes. D (by Gianni Jacucci): angle-resolved reflectance.

membranes α is smaller than two. More specifically, $\alpha = 1.35 \pm 0.10$ and $A = 0.14 \pm 0.01$ for the semi-transparent membrane, and $\alpha = 1.34 \pm 0.15$ and $A = 0.65 \pm 0.10$ for the white one. Details of the values found are presented in Table 8.1 and Table 8.2. The fit is based on a non-linear least-squares fit where each data point is weighted by its standard deviation in x and y (Python open source code: curve_fit from *scipy.optimize* library). The curves are forced to pass through (0,1). That is, the transmittance for a slab of zero thickness is unity.

Table 8.1 Parameters used for the normal diffusion fitting, Equation 2.46

Membrane appearance	Parameter A (μm)	Standard deviation in A (μm)
Transparent	0.004	0.0005
Semi-transparent	0.050	0.006
White	0.231	0.035

Table 8.2 Parameters used for the Ohm law fitting, Equation 2.45

Membrane appearance	Absorption length l_A	St. dev. in l_A	Extrapolation length z_e	St. dev. in z_e
Transparent	262.6	26.9	214.1	21.9
Semi-transparent	37.2	7.6	30.3	6.2
White	6.7	3.1	5.4	2.5

To further understand the anomalous diffusive behaviour of the samples and the unusual scaling law, the morphology of the membranes is analysed by SEM (Figure 8.5) and nitrogen physisorption (Figure 8.3). The typical anisotropy (*i.e.* the transversely isotropic in-plane orientation of fibrils) of CNF–based materials is observed for all membranes when comparing the top-view SEM images and the cross-section exposed by either uniaxial tensile fracture [262, 265].

The SEM images reported in Figure 8.5A-B show that the transparent membranes are composed of a homogeneous network of fine fibrils inter-spaced by small air voids. The pore size distribution clearly peaks around 30 nm (Figure 8.3), whereas the average diameter of the fibrils is approximately 4 nm (Figure 8.2C). From the morphological analysis and scattering cross-section calculations (Figure 8.6) it is possible to infer that the scattering in this case is mainly caused by the presence of the small air pores as the fibril size is too small to produce significant scattering in this system.

In contrast, in the case of the semi-transparent membranes, the SEM images show a certain number of significantly larger pores (Figure 8.5C-D). This is confirmed by the broader

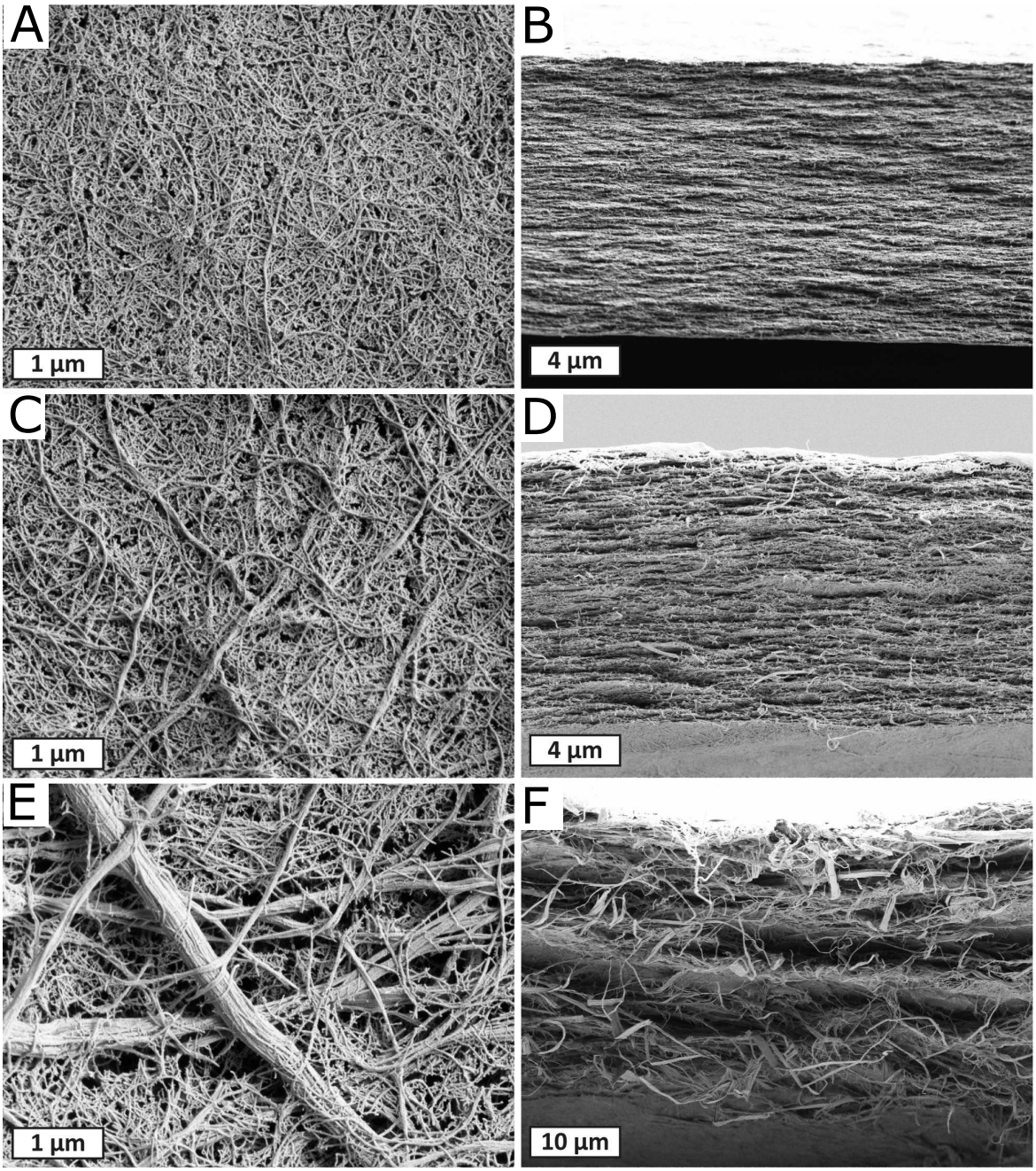

Fig. 8.5 A-C:SEM micrographs of top surfaces of membranes. D-F: their corresponding cross-sectional fracture surfaces. Transparent (A,B), semi-transparent (C,D), and white membranes (E,F), respectively. Arguably, the layered structure could be an artefact induced during the samples' fracture [260].

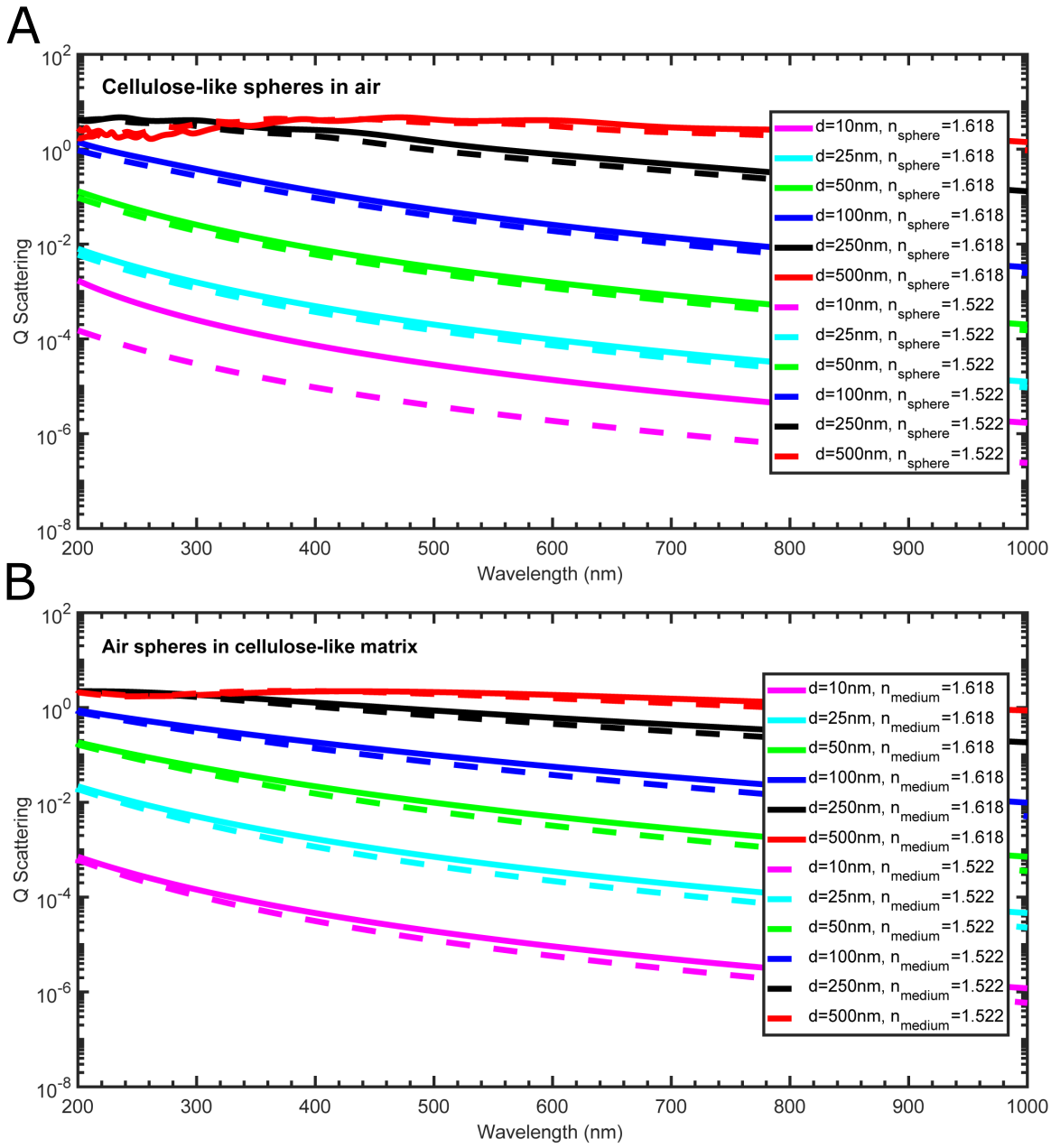

Fig. 8.6 A: scattering efficiency, $Q_{scattering}$, as a function of wavelength for cellulose spheres in air. B: $Q_{scattering}$ for air spheres in a cellulose matrix. As expected from Mie theory, particles with diameters, d, around 200-500 nm are stronger scatterers. Interestingly, the scattering strength for the air inclusions is similar to the one of cellulose spheres. Calculations performed using MiePlot by Philip Lavern.

distribution of pore sizes, extending up to 100 nm, as observed by nitrogen physisorption (Figure 8.3).

Similarly, in the SEM images of white membranes (Figure 8.5E-F), several anisotropic large pores (up to hundreds of nanometres) are recognizable, as confirmed by the porosity measurements. In this case, the main fraction of the volume is occupied by the network of fine fibrils inter-spaced by small pores. However, individual thicker fibrils (100-500 nm) are also sparsely embedded in this matrix in less dense regions.

Therefore one can speculate that the anomalous light transport for the semi-transparent and white membranes is induced by the combination of the anisotropy of the scatterers (*i.e.* in-plane orientation of fibrils and pores), and the rather wide distribution of sizes of both pores and fibrils, which consequently leads to a sparse spatial distribution of the stronger scatterers.

To provide even stronger evidence that the observed anomalous diffusion of light is not merely due to artefacts introduced in the sample preparation (*e.g.* due to the dependence of the morphological features on sample thickness), a speckle statistic experiment is performed [73]. The speckle patterns produced by laser light transmitted through the investigated samples is imaged and recorded at more than 2000 separate locations. Two polarisers are mounted in crossed configuration in order to suppress the contribution from the light that propagates ballistically through the sample (Figure 8.7A).

To better understand the data, the response of white CNF membranes is compared to standard filter paper (which is known to be a conventional diffuser with $\alpha = 2$ and scattering mean free path ≈ 25 μm [14]). When light is transmitted through a standard diffusing sample, the individual speckles (or grains) vary between different sample locations but on average the radius and intensity of the whole pattern is roughly constant as the light transport properties are the same across the specimen. For anomalous sample, instead, the difference in speckle patterns between different sample locations is greater as the light paths can differ significantly depending on the local characteristics of the specimen [65]. This behaviour has also been confirmed by Monte Carlo simulations [65].

As expected for anomalous diffusion, the speckle statistics differ greatly for common paper as compare to a white membrane (Figure 8.7B,C). The high degree of spatial and intensity variability between the different disorder realizations further confirms the anomalous diffusive behaviour of the system. For the standard diffusive samples the *radii* and intensities of the speckle patterns are fairly constant at different positions, while for the white CNF membranes a broad distribution of values is observed.

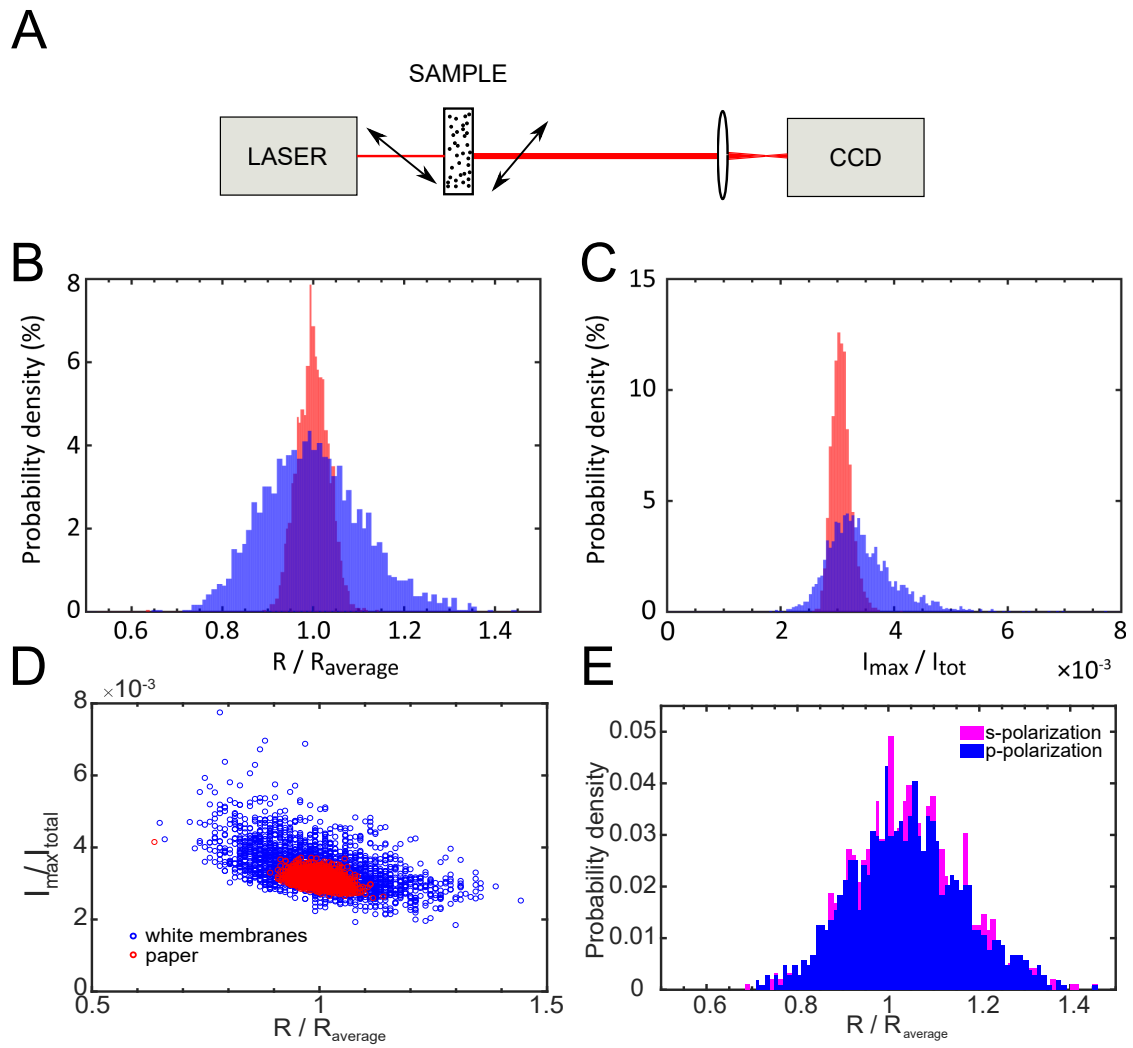

Fig. 8.7 A: the samples are illuminated from the front with a collimated laser beam (NKT SuperK EXTREME tuned to 635 nm *via* a SuperK VARIA) and the image of the output speckled pattern is recorded by a CCD (IDS UI-3580LE) after being demagnified by lens L_1. The sample is placed on a motorized stage (Thorlabs Z825B) so that each image is collected for a different disorder realization. More than 2000 images are acquired for each sample. The sample is mounted between crossed polarisers P_1 and P_2 (Thorlabs LPVISE100-A) in order to extinguish any residual ballistic light. B: distribution of the *radii*, R, of the speckle images normalized to their average $R_{average}$. C: distribution of the intensity, calculated as the ratio between the maximum intensity I_{max} and the total image intensity I_{tot}. For filter paper both histograms show a narrow distribution, as expected for a normally diffusive medium. In contrast, the population is considerably wider for the white CNF membranes, as expected for anomalous transport [65]. D: study of the correlation between intensity and radius of the individual patterns. E: the speckle statistics is not affected by the incident polarisation.

It is also possible to evaluate the correlation between the different speckle patterns. In Figure 8.7D the coordinates of each data point correspond to the normalised *radius* and intensity for a single pattern. For common paper, the data tend to cluster around the point (1,1) as the pattern dimensions and intensity are very similar. In contrast, for the white membranes, one can observe that the data is spread in both dimensions as a consequence of the variability of the speckles. A clear trend emerges in which the brightest patterns are associated with the smallest *radii* and *vice versa* the larger speckle spots are linked to the less intense images. This is to be expected: as the laser intensity is constant, patterns that are more spread tend to redistribute the intensity over a larger area so they the maximum intensity is, on average, lower than that of pattern where the speckles are spatially concentrated.

Therefore, it reasonable to speculate that the observed anomalous diffusion response in white and semi-transparent CNF samples is due to three main factors:

1. the inhomogeneity in scattering strength due to the polydispersity of the fibrils (assuming that each fibril can be considered a single scattering centre);

2. the inhomogeneity in the spatial distribution of fibrils, which could introduce longer steps between scattering events;

3. the anisotropy of the system due to in-plane orientation of the fibrils and anisotropic pores [262, 265], which implies that light propagation and scattering proceed differently when occurring across the plane or parallel to the plane of the membrane (at this stage, further structural characterisation, *e.g.* by TEM tomography, was not possible due to the high porosity of the material).

It can be excluded that the intrinsic birefringence of cellulose (*i.e.* refractive index of 1.539-1.596 along the fibre and 1.519-1.538 in the transverse direction [266, 267]) contributes strongly to this effect, as this would generate only negligible differences in the scattering cross-section (see the calculations in Figure 8.6 and the measured transmittance of s- and p-polarized light in Figure 8.7E).

8.4 Conclusion

This chapter reports a white beetle-inspired cellulose-based system in which it is possible to manipulate light transport by simply tuning the morphology and the distribution of the CNF fibrils in porous membranes. A transition from standard to anomalous diffusion is observed in the disordered photonic nanostructures when larger anisotropy in the fibril distribution is introduced. Even though further optimization by fine-tuning of the porosity

and of the diameter distribution of the fibrils could lead to even thinner and brighter white membranes, already extremely high scattering efficiency is obtained in only few microns thickness [56, 135]. In addition, the membranes are stable over several months of exposure to air and flexible.

In the future, further investigation of the three-dimensional structure of the cellulose membranes could be carried out using, for example, cryo-TEM and cryo-SEM in order to preserve the structure during imaging. Furthermore, a back-scattering cone study of the light transport could be used to enhance the understanding of the anomalous behaviour of this material. In fact, as long light paths contribute to the "tails" of the cone and short ones to the peak, it could be possible to extrapolate information about the light paths population and how this latter differs in the various membranes.

In conclusion, this work showcases the potential of using CNF and anomalous diffusion to produce next-generation efficient bright sustainable and biocompatible white materials.

Chapter 9

Conclusions, future directions, and perspectives

The maturity of field of natural photonics is evident from the increasing number of publications around this topic: a large number of structurally coloured species have been investigated, proving insight both into the biological aspects of structural colour and inspiration for new optical materials. However, these studies have often neglected two aspects of this field.

Firstly, the intrinsic multidisciplinarity of the topic implies that researchers from different areas need to collaborate to achieve overarching conclusions. In particular, the joint effort of the biological, chemical, and physical community is required to fully investigate the photonic structures found in nature and their role. Unfortunately, it is often the case that lack of expertise in a certain domain results in publications where one aspect of the investigation is heavily predominant at the expense of the other.

Secondly, the research in the field of photonics has historically concentrated mainly on periodic structures. This is probably due to past limitations in imaging and computational techniques in addition to a cultural preference for order as opposed to disorder. However, nowadays the interest is increasingly shifting to complex media, demonstrating the full potential of these structures.

This thesis hopes to reconcile both aspects by bringing together physical and biological considerations without neglecting the role of disorder which, in fact, plays a key role in a few of the systems explored.

9.1 Developmental considerations

From a fundamental point of view, it is of interest to understand how structural colours form during the growth of an organism. The two main hypothesis are that either the structures self-assemble or that they come together under the push of biologically-driven processes. The study of the development of the multilayer in the green beetle *G. viridula* presented in Chapter 5 leans towards the second hypothesis as no evidence of a self-assembly process was observed: the layers are deposited in a stratified fashion and only later the hardening of the cuticle and the polymerisation of the pigments lead to the full optical response. This, of course, does not exclude that other types of photonic structures might form by self-assembly. For example, chiral reflectors are known in a number of beetle species: these systems do not rely on the presence of pigments to produce colour, suggesting that a different mechanism might be involved. Hence, further studies are needed to explore a larger number of organisms and architectures to gain a global understanding of the developmental processes involved and potentially offer inspiration for improving the production methods of artificial nanomaterials.

9.2 Evolutionary races

Biological populations are under the constant pressure of evolutionary needs. In the case of the green beetle *G. viridula*, the development of the multilayer involves only a few, relatively simple, steps. This leads to the idea that the organism could easily adapt, for example to a different environment, by varying the thickness of the layers or the proportion of their chemical contents. It can be speculated that this would be more easily achieved than changing the chemical pathways and the pigments produced.

However, the case of the parasitic bird *P. regulus* described in Chapter 6 seems to suggest the opposite: this bird is under a strong evolutionary pressure to produce blue-coloured eggs to match his hosts'. Given that this could be equally achieved either by structural colouration or by pigmentation, it is interesting to see how the second has prevailed.

Finally, the white beetle *Cyphochilus* is an example of an organism where structural colouration is not only present but also fully optimised and perfected, as demonstrated in Chapter 7. Achieving such strong scattering using a low refractive index medium is a remarkable achievement, outpacing all human-made materials.

9.3 Bio-inspiration

Nature can be a great source of inspiration for artificial photonics, not only in their shapes and architectures but also in the choice of biocompatible materials.

Using bio-photonics structures as a template can used to demonstrate concepts, such as Anderson localisation, which have eluded the scientific community for decades (see Chapter 7). Even though the process is delicate and requires further optimisation, the experiment shows the potential of this approach.

At the same time, learning from nature's designs and fabrication routes, one can produce biocompatible materials in a scalable and reliable way. Chapter 8 shows an example of this methodology: a random network of cellulose fibres is produced *via* a fractionation process, yielding strongly white membranes that can be used for a variety of applications (from paints to consumer goods), showing how by understanding and optimising light transport in complex materials one can achieve better performances. In fact, the system presented could be further improved by refining the fibres diameters and filling fraction based on computational simulations.

References

[1] E Hecht. *Optics*. Addison Wesley, San Francisco, 4th edition, 2002. pp. 1-10.

[2] IC Cuthill, WL Allen, K Arbuckle, B Caspers, G Chaplin, ME Hauber, GE Hill, NG Jablonski, CD Jiggins, A Kelber, et al. The biology of color. *Science*, 357(6350):eaan0221, 2017.

[3] HH Thoen, MJ How, T-H Chiou, and J Marshall. A different form of color vision in mantis shrimp. *Science*, 343(6169):411–413, 2014.

[4] DR Norris, PP Marra, R Montgomerie, TK Kyser, and LM Ratcliffe. Reproductive effort, molting latitude, and feather color in a migratory songbird. *Science*, 306(5705):2249–2250, 2004.

[5] R Mehta and RJ Zhu. Blue or red? exploring the effect of color on cognitive task performances. *Science*, 323(5918):1226–1229, 2009.

[6] DW Lee. *Nature's palette: the science of plant color*. University Of Chicago Press, Chicago, 1st edition, 2007. p. 61-63.

[7] J Baumberg. Extruding opals: Self-assembling active soft nanophotonics on the kilometre scale. In *Integrated Photonics Research, Silicon and Nanophotonics*, page IWB1. Optical Society of America, 2011.

[8] AR Parker. 515 million years of structural colour. *Journal of Optics A: Pure and Applied Optics*, 2(6):R15, 2000.

[9] Y Sun, FD Fracchia, TW Calvert, and MS Drew. Deriving spectra from colors and rendering light interference. *IEEE Computer Graphics and Applications*, 19(4):61–67, 1999.

[10] P Vukusic and J R Sambles. Photonic structures in biology. *Nature*, 424(6950):852, 2003.

[11] J Zi, X Yu, Y Li, X Hu, C Xu, X Wang, X Liu, and R Fu. Coloration strategies in peacock feathers. *Proceedings of the National Academy of Sciences*, 100(22):12576–12578, 2003.

[12] H Noh, S F Liew, V Saranathan, S G J Mochrie, R O Prum, ER Dufresne, and H Cao. Structural Color: How Noniridescent Colors Are Generated by Quasi-ordered Structures of Bird Feathers (Adv. Mater. 26-27/2010). *Advanced Materials*, 22(26-27), 2010.

[13] RO Prum and R Torres. Structural colouration of avian skin: convergent evolution of coherently scattering dermal collagen arrays. *Journal of Experimental Biology*, 206(14):2409–2429, 2003.

[14] M Burresi, L Cortese, L Pattelli, M Kolle, P Vukusic, DS Wiersma, U Steiner, and S Vignolini. Bright-White Beetle Scales Optimise Multiple Scattering of Light. *Scientific Reports*, 4, 2014.

[15] A Saito, T Shibuya, M Yonezawa, M Akai-Kasayaa, and Y Kuwahara. Simulation analysis on the optical role of the number of randomly arranged nano-trees on the morpho butterfly's scale. In *Proceedings of SPIE*, volume 8686, pages 86860J–1, 2013.

[16] MR Nixon, AG Orr, and P Vukusic. Covert linear polarization signatures from brilliant white two-dimensional disordered wing structures of the phoenix damselfly. *Journal of The Royal Society Interface*, 14(130):20170036, 2017.

[17] HB de Aguiar, S Gigan, and S Brasselet. Polarization recovery through scattering media. *Science Advances*, 3(9):e1600743, 2017.

[18] S Vignolini, E Moyroud, BJ Glover, and U Steiner. Analysing photonic structures in plants. *Journal of The Royal Society Interface*, 10(87):20130394, 2013.

[19] S Kinoshita and S Yoshioka. Structural colors in nature: the role of regularity and irregularity in the structure. *ChemPhysChem*, 6(8):1442–1459, 2005.

[20] BD Wilts, X Sheng, M Holler, A Diaz, Ma Guizar-Sicairos, J Raabe, R Hoppe, S-H Liu, R Langford, OD Onelli, D Chen, S Torquato, U Steiner, CG Schroer, S Vignolini, and A Sepe. Evolutionary-optimized photonic network structure in white beetle wing scales. *Advanced Materials*, page 1702057, 2017.

[21] M Born. *Principles of Optics*. Cambridge University Press, Cambridge, 7th edition, 1999. p. 76.

[22] P Yeh. *Optical waves in layered media*. John Wiley & Sons inc., Hoboken, reprint edition, 2005. p. 2.

[23] E Hecht. *Optics*. Addison Wesley, San Francisco, 4th edition, 2002. pp. 46-47.

[24] P Yeh. *Optical waves in layered media*. John Wiley & Sons inc., Hoboken, reprint edition, 2005. pp. 58-59.

[25] E Hecht. *Optics*. Addison Wesley, San Francisco, 4th edition, 2002. pp. 113-116.

[26] P Yeh. *Optical waves in layered media*. John Wiley & Sons inc., Hoboken, reprint edition, 2005. P. 102-110.

[27] S Byrnes. Multilayer optical calculations. *arXiv e-prints*, 2016. DOI: arXiv:1603.02720v2.

[28] S Kinoshita, S Yoshioka, and J Miyazaki. Physics of structural colors. *Reports on Progress in Physics*, 71(7):076401, 2008.

[29] MF Land. The physics and biology of animal reflectors. *Progress in biophysics and molecular biology*, 24:75–106, 1972.

[30] HL Leertouwer, BD Wilts, and DG Stavenga. Refractive index and dispersion of butterfly chitin and bird keratin measured by polarizing interference microscopy. *Optics Express*, 19(24):24061, 2011.

[31] DG Stavenga, HL Leertouwer, and BD Wilts. Quantifying the refractive index dispersion of a pigmented biological tissue using jamin–lebedeff interference microscopy. *Light: Science & Applications*, 2(9):e100, 2013.

[32] DW Lee. *Nature's palette: the science of plant color*. University Of Chicago Press, Chicago, 1st edition, 2007. p. 39.

[33] DS Wiersma. Disordered photonics. *Nature Photonics*, 7(3):188–196, 2013.

[34] EH Zhou, A Shibukawa, J Brake, H Ruan, and C Yang. Glare suppression by coherence gated negation. *Optica*, 3(10):1107, 2016.

[35] A Daniel, L Liberman, and Y Silberberg. Wavefront shaping for glare reduction. *Optica*, 3(10):1104, 2016.

[36] F Scheffold and ID Block. Rapid high resolution imaging of diffusive properties in turbid media. *Optics express*, 20(1):192–200, 2012.

[37] J Bertolotti. Non-invasive imaging: Peeking through the curtain. *Nature Photonics*, 8(10):751, 2014.

[38] R Kumble and RM Hochstrasser. Disorder-induced exciton scattering in the light-harvesting systems of purple bacteria: Influence on the anisotropy of emission and band-band transitions. *The Journal of chemical physics*, 109(2):855–865, 1998.

[39] J Syurik, RH Siddique, A Dollmann, G Gomard, M Schneider, M Worgull, G Wiegand, and H Hölscher. Bio-inspired, large scale, highly-scattering films for nanoparticle-alternative white surfaces. *Scientific Reports*, 7, 2017.

[40] R Sapienza. *Photonic nano materials: anisotropic transport and optical Bloch oscillations*. PhD thesis, Université Pierre et Marie Curie-Paris VI, 2005. pp.16-18. Open source: https://tel.archives-ouvertes.fr/tel-00009751/document.

[41] P Sheng. *Introduction to Wave Scattering, Localization, and Mesoscopic Phenomena*. Elsevier, 1995. pp.2-3.

[42] P Sheng. *Introduction to Wave Scattering, Localization, and Mesoscopic Phenomena*. Elsevier, 1995. p.189.

[43] A Einstein. *Investigations on the Theory of the Brownian Movement*. Courier Corporation, 1956.

[44] S Vignolini. *Sub-wavelength probing and modification of complex photonic structures*, volume 15. Firenze University Press, 2010. pp.13-15.

[45] S Chen, A Maksimchuk, and D Umstadter. Experimental observation of relativistic nonlinear thomson scattering. *Nature*, 396(6712):653–655, 1998.

[46] JW Strutt. Lviii. on the scattering of light by small particles. *Philosophical Magazine*, 41(275):447–454, 1871.

[47] JW Strutt. Xv. on the light from the sky, its polarization and colour. *The London, Edinburgh, and Dublin Philosophical Magazine and Journal of Science*, 41(271):107–120, 1871.

[48] G Mie. Beiträge zur optik trüber medien, speziell kolloidaler metallösungen. *Annalen der physik*, 330(3):377–445, 1908.

[49] H Moyes Nussenveig. *The theory of the rainbow*. WH Freeman, 1977.

[50] P Bouguer. *Essai d'optique sur la gradation de la lumiére*. chez Claude Jombert, ruë S. Jacques, au coin de la ruë des Mathurins, á l'Image Notre-Dame, 1729.

[51] JF Galisteo-López, M Ibisate, R Sapienza, LS Froufe-Pérez, Á Blanco, and C López. Self-assembled photonic structures. *Advanced Materials*, 23(1):30–69, 2011.

[52] MP van Albada, BA van Tiggelen, A Lagendijk, and A Tip. Speed of propagation of classical waves in strongly scattering media. *Physical review letters*, 66(24):3132, 1991.

[53] JX Zhu, D J Pine, and DA Weitz. Internal reflection of diffusive light in random media. *Physical Review A*, 44(6):3948, 1991.

[54] D Contini, F Martelli, and G Zaccanti. Photon migration through a turbid slab described by a model based on diffusion approximation I Theory. *Applied Optics*, 36(19):4587, 1997.

[55] PD Garcia Fernandez. *From Photonic Crystals to Photonic Glasses through disorder*. PhD thesis, Universidad Autónoma de Madrid, 2008. p.12. Open source: https://repositorio.uam.es/handle/10486/101.

[56] S Caixeiro, M Peruzzo, OD Onelli, S Vignolini, and R Sapienza. Disordered cellulose-based nanostructures for enhanced light scattering. *ACS Applied Materials & Interfaces*, 9(9):7885–7890, 2017.

[57] J Klafter and IM Sokolov. Anomalous diffusion spreads its wings. *Physics world*, 18(8):29, 2005.

[58] P Nelson. *Biological physics*. WH Freeman New York, 2004. pp.98–130.

[59] R Metzler and J Klafter. The random walk's guide to anomalous diffusion: a fractional dynamics approach. *Physics reports*, 339(1):1–77, 2000.

[60] R Inglis and C Taylor. Numerical approximation of levy flight, 2011. URL: https://math.stackexchange.com/questions/52869/numerical-approximation-of-levy-flight, last accessed 2017-07-20.

[61] BV Gnedenko and AN Kolmogorov. Limit distributions for sums of independent. *American Journal of Mathematics*, 105, 1954.

[62] H Hinrichsen. Non-equilibrium phase transitions with long-range interactions. *Journal of Statistical Mechanics: Theory and Experiment*, 2007(07):P07006, 2007.

[63] DW Sims, EJ Southall, NE Humphries, GC Hays, CJA Bradshaw, JW Pitchford, A James, MZ Ahmed, AS Brierley, MA Hindell, et al. Scaling laws of marine predator search behaviour. *Nature*, 451(7182):1098, 2008.

[64] M Weiss, M Elsner, F Kartberg, and T Nilsson. Anomalous subdiffusion is a measure for cytoplasmic crowding in living cells. *Biophysical journal*, 87(5):3518–3524, 2004.

[65] P Barthelemy, J Bertolotti, and DS Wiersma. A lévy flight for light. *Nature*, 453(7194):495, 2008.

[66] J Bertolotti, K Vynck, L Pattelli, P Barthelemy, S Lepri, and D S Wiersma. Engineering disorder in superdiffusive levy glasses. *Advanced Functional Materials*, 20(6):965–968, 2010.

[67] TG Dewey, MM Novak, A Davis, and A Marshak. Levy kinetics in slab geometry: scaling of transmission probability. In *Fractal Frontiers*, 1997. pp.63–72.

[68] P Lévy. *Théorie de l'addition des variables aléatoires / par Paul Lévy ; préf. de Émile Borel.* Collection des monographies des probabilités ; fasc. 1. Gauthier-Villars, Paris, 2. ed. edition, 1954.

[69] CW Groth, AR Akhmerov, and CWJ Beenakker. Transmission probability through a lévy glass and comparison with a lévy walk. *Physical Review E*, 85(2):021138, 2012.

[70] P Buonsante, R Burioni, and A Vezzani. Transport and scaling in quenched two-and three-dimensional lévy quasicrystals. *Physical Review E*, 84(2):021105, 2011.

[71] T Svensson, K Vynck, E Adolfsson, A Farina, A Pifferi, and DS Wiersma. Light diffusion in quenched disorder: Role of step correlations. *Physical Review E*, 89(2):022141, 2014.

[72] P Barthelemy, J Bertolotti, K Vynck, S Lepri, and DS Wiersma. Role of quenching on superdiffusive transport in two-dimensional random media. *Physical Review E*, 82(1):011101, 2010.

[73] K Vynck, J Bertolotti, P Barthelemy, and DS Wiersma. Superdiffusion of light in lévy glasses. *Optical Properties of Photonic Structures: Interplay of Order and Disorder*, page 227, 2012.

[74] H Subramanian, P Pradhan, YL Kim, and V Backman. Penetration depth of low-coherence enhanced backscattered light in subdiffusion regime. *Physical Review E*, 75(4):041914, 2007.

[75] PW Anderson. Absence of diffusion in certain random lattices. *Physical review*, 109(5):1492, 1958.

[76] A Lagendijk, B Van Tiggelen, and DS Wiersma. Fifty years of anderson localization. *Physics Today*, 62(8):24–29, 2009.

[77] R Dalichaouch, JP Armstrong, et al. Microwave localization by two-dimensional random scattering. *Nature*, 354(6348):53, 1991.

[78] S John. Strong localization of photons in certain disordered dielectric superlattices. *Physical review letters*, 58(23):2486, 1987.

[79] S John. Localization of light. *Physics Today*, 44(5):32–40, 1991.

[80] PW Anderson. The question of classical localization a theory of white paint? *Philosophical Magazine B*, 52(3):505–509, 1985.

[81] DS Wiersma, P Bartolini, A Lagendijk, and R Righini. Localization of light in a disordered medium. *Nature*, 390(6661):671, 1997.

[82] MK Gunde and ZC Orel. Absorption and scattering of light by pigment particles in solar-absorbing paints. *Applied optics*, 39(4):622–628, 2000.

[83] F Scheffold, R Lenke, R Tweer, and G Maret. Localization or classical diffusion of light? *Nature*, 398(6724):206, 1999.

[84] T Sperling, W Buehrer, CM Aegerter, and G Maret. Direct determination of the transition to localization of light in three dimensions. *Nature Photonics*, 7(1):48–52, 2013.

[85] G Maret, T Sperling, W Bührer, A Lubatsch, R Frank, and CM Aegerter. Inelastic scattering puts in question recent claims of anderson localization of light. *Nature Photonics*, 7(12):934–935, 2013.

[86] SE Skipetrov and IM Sokolov. Absence of anderson localization of light in a random ensemble of point scatterers. *Physical review letters*, 112(2):023905, 2014.

[87] F Helmchen and W Denk. Deep tissue two-photon microscopy. *Nature methods*, 2(12):932–940, 2005.

[88] K Busch, CM Soukoulis, and EN Economou. Transport and scattering mean free paths of classical waves. *Physical Review B*, 50(1):93, 1994.

[89] LI Goldfischer. Autocorrelation function and power spectral density of laser-produced speckle patterns. *Journal of the Optical Society of America*, 55(3):247–253, 1965.

[90] E Hecht. *Optics*. Addison Wesley, San Francisco, 4th edition, 2002. pp. 602–603.

[91] A Mashaal, Hand Goldstein, D Feuermann, and JM Gordon. First direct measurement of the spatial coherence of sunlight. *Optics letters*, 37(17):3516–3518, 2012.

[92] J Bertolotti. Multiple scattering: Unravelling the tangle. *Nature Physics*, 11(8):622, 2015.

[93] J Bertolotti, EG van Putten, C Blum, A Lagendijk, WL Vos, and AP Mosk. Non-invasive imaging through opaque scattering layers. *Nature*, 491(7423):232–234, 2012.

[94] A Labeyrie. Attainment of diffraction limited resolution in large telescopes by fourier analysing speckle patterns in star images. *Astron. Astrophys*, 6(1):85–87, 1970.

[95] MP Van Albada, JF De Boer, and A Lagendijk. Observation of long-range intensity correlation in the transport of coherent light through a random medium. *Physical review letters*, 64(23):2787, 1990.

[96] AZ Genack, N Garcia, and W Polkosnik. Long-range intensity correlation in random media. *Physical review letters*, 65(17):2129, 1990.

[97] N Fayard, A Cazé, R Pierrat, and R Carminati. Intensity correlations between reflected and transmitted speckle patterns. *Physical Review A*, 92(3):033827, 2015.

[98] A Z Genack. Optical transmission in disordered media. *Physical review letters*, 58(20):2043, 1987.

[99] BZ Spivak and A Y Zyuzin. Fluctuations of coherent light transmission through disordered media. *Solid state communications*, 65(5):311–313, 1988.

[100] AU Zyuzin and BZ Spivak. Langevin description of mesoscopic fluctuations in disordered media. *Soviet Physics, JETP*, 66(3):560–566, 1987.

[101] B Shapiro. Large intensity fluctuations for wave propagation in random media. *Physical review letters*, 57(17):2168, 1986.

[102] R Pnini and B Shapiro. Fluctuations in transmission of waves through disordered slabs. *Physical Review B*, 39(10):6986, 1989.

[103] N Curry, P Bondareff, M Leclercq, NF Van Hulst, R Sapienza, S Gigan, and S Grésillon. Direct determination of diffusion properties of random media from speckle contrast. *Optics letters*, 36(17):3332–3334, 2011.

[104] R Sapienza. *Photonic nano materials: anisotropic transport and optical Bloch oscillations*. PhD thesis, Université Pierre et Marie Curie-Paris VI, 2005. pp.23–24. Open source: https://tel.archives-ouvertes.fr/tel-00009751/document.

[105] DS Wiersma. *Light in strongly scattering and amplifying random media*. Phd, University of Amsterdam, 11/1995 1995. pp. 36–39. Open source: http://cops.nano-cops.com/sites/default/files/wiersma.pdf.

[106] OL Muskens, AF Koenderink, and WL Vos. Broadband coherent backscattering spectroscopy of the interplay between order and disorder in three-dimensional opal photonic crystals. *Physical Review B*, 83(15):155101, 2011.

[107] MP Van Albada and A Lagendijk. Observation of weak localization of light in a random medium. *Physical review letters*, 55(24):2692, 1985.

[108] P-E Wolf and G Maret. Weak localization and coherent backscattering of photons in disordered media. *Physical review letters*, 55(24):2696, 1985.

[109] M Burresi, V Radhalakshmi, R Savo, J Bertolotti, K Vynck, and DS Wiersma. Weak localization of light in superdiffusive random systems. *Physical review letters*, 108(11):110604, 2012.

[110] FL Pedrotti. *Introduction to optics.* Pearson/Addison Wesley ; Pearson Education, San Francisco, Calif. : London, 3rd ed. edition, 2007. pp. 163-169.

[111] Y Kuga and A Ishimaru. Retroreflectance from a dense distribution of spherical particles. *JOSA A*, 1(8):831–835, 1984.

[112] L Tsang and A Ishimaru. Backscattering enhancement of random discrete scatterers. *Journal of the Optical Society of America A*, 1(8):836–839, 1984.

[113] E Akkermans and G Montambaux. *Mesoscopic physics of electrons and photons*. Cambridge university press, 2007. pp.343–376.

[114] OL Muskens and A Lagendijk. Broadband enhanced backscattering spectroscopy of strongly scattering media. *Optics express*, 16(2):1222–1231, 2008.

[115] JJ Baumberg, OL Pursiainen, and P Spahn. Resonant optical scattering in nanoparticle-doped polymer photonic crystals. *Physical Review B*, 80(20):201103, 2009.

[116] GJ Black, DB Campbell, and PD Nicholson. Icy galilean satellites: Modeling radar reflectivities as a coherent backscatter effect. *Icarus*, 151(2):167–180, 2001.

[117] E Hecht. *Optics*. Addison Wesley, San Francisco, 4th edition, 2002. p. 215.

[118] P Elterman. Integrating cavity spectroscopy. *Applied Optics*, 9(9):2140, 1970.

[119] KF Carr. Integrating sphere theory and applications Part II: Integrating sphere applications. *Surface Coatings International*, 80(10):485, 1970.

[120] KF Carr. Integrating sphere theory and applications Part I: Integrating sphere theory and design. *Surface Coatings International*, 80(8):380, 1997.

[121] M De Graef. *Introduction to Conventional Transmission Electron Microscopy*. Cambridge University Press, 2003.

[122] IM Watt. *The Principles and Practice of Electron Microscopy*. Cambridge University Press, 1997. pp. 1-29.

[123] L Reimer. *Scanning electron microscopy : physics of image formation and microanalysis.* Springer series in optical sciences ; v.45. Springer, Berlin, 2nd ed. edition, 1998.

[124] DB Williams and CB Carter. The transmission electron microscope. In *Transmission electron microscopy*, pages 3–17. Springer, 1996.

[125] L Reimer. *Scanning electron microscopy : physics of image formation and microanalysis.* Springer series in optical sciences ; v.45. Springer, Berlin, 2nd ed. edition, 1998.

[126] G Knott, H Marchman, D Wall, and B Lich. Serial section scanning electron microscopy of adult brain tissue using focused ion beam milling. *Journal of Neuroscience*, 28(12):2959–2964, 2008.

[127] LA Giannuzzi and FA Stevie. A review of focused ion beam milling techniques for tem specimen preparation. *Micron*, 30(3):197–204, 1999.

[128] S Reyntjens and R Puers. A review of focused ion beam applications in microsystem technology. *Journal of micromechanics and microengineering*, 11(4):287, 2001.

[129] B Kientz, P Vukusic, S Luke, and E Rosenfeld. Iridescence of a Marine Bacterium and Classification of Prokaryotic Structural Colors. *Applied and Environmental Microbiology*, 78(7):2092, 2012.

[130] R Gordon, D Losic, MA Tiffany, SS Nagy, and FAS Sterrenburg. The Glass Menagerie: diatoms for novel applications in nanotechnology. *Trends in Biotechnology*, 27(2):116, 2009.

[131] DJ Kemp, ME Herberstein, and GF Grether. Unraveling the true complexity of costly color signaling. *Behavioral Ecology*, 23(2):233–236, 2011.

[132] A Loyau, D Gomez, B Moureau, M Théry, and NS Hart. Iridescent structurally based coloration of eyespots correlates with mating success in the peacock. *Behavioral Ecology*, 18(6):1123, 2007.

[133] BD Wilts, K Michielsen, J Kuipers, H De Raedt, and DG Stavenga. Brilliant camouflage: photonic crystals in the diamond weevil, *Entimus imperialis*. *Proceedings of the Royal Society B: Biological Sciences*, 279(1738):2524, 2012.

[134] P Vukusic, JR Sambles, CR Lawrence, and RJ Wootton. Quantified interference and diffraction in single Morpho butterfly scales. *Proceedings of the Royal Society B: Biological Sciences*, 266(1427):1403, 1999.

[135] P Vukusic, B Hallam, and J Noyes. Brilliant Whiteness in Ultrathin Beetle Scales. *Science*, 315(5810):348, 2007.

[136] J Vinther, DEG Briggs, J Clarke, G Mayr, and RO Prum. Structural coloration in a fossil feather. *Biology Letters*, 6(1):128, 2009.

[137] ME McNamara, DEG Briggs, PJ Orr, H Noh, and H Cao. The original colours of fossil beetles. *Proceedings of the Royal Society B: Biological Sciences*, 279(1731):1114, 2011.

[138] V Coffey. Where life meets light: Bio-inspired photonics. *Optics and Photonics News*, 26(4):24–31, 2015.

[139] JA Bossard, L Lin, and DH Werner. Evolving random fractal Cantor superlattices for the infrared using a genetic algorithm. *Journal of The Royal Society Interface*, 13(116):20160186, 2016.

[140] KD Feller, TM Jordan, D Wilby, and NW Roberts. Selection of the intrinsic polarization properties of animal optical materials creates enhanced structural reflectivity and camouflage. *Philosophical Transactions of the Royal Society B*, 372(1724):20160336, 2017.

[141] EJ Denton. Review lecture: on the organization of reflecting surfaces in some marine animals. *Philosophical Transactions of the Royal Society of London B: Biological Sciences*, 258(824):285–313, 1970.

[142] EJ Denton and MF Land. Mechanism of reflexion in silvery layers of fish and cephalopods. *Proceedings of the Royal Society of London B: Biological Sciences*, 178(1050):43–61, 1971.

[143] DR McKenzie, Y Yin, and WD McFall. Silvery fish skin as an example of a chaotic reflector. In *Proceedings of the Royal Society of London A: Mathematical, Physical and Engineering Sciences*, volume 451, pages 579–584. The Royal Society, 1995.

[144] AR Parker. A geological history of reflecting optics. *Journal of the Royal Society Interface*, 2(2):1–17, 2005.

[145] AE Seago, P Brady, J-P Vigneron, and TD Schultz. Gold bugs and beyond: a review of iridescence and structural colour mechanisms in beetles (coleoptera). *Journal of the Royal Society Interface*, 6:S165–S184, 2009.

[146] C Campos-Fernández, DE Azofeifa, M Hernández-Jiménez, A Ruiz-Ruiz, and WE Vargas. Visible light reflection spectra from cuticle layered materials. *Optical Materials Express*, 1(1):85–100, 2011.

[147] J Yong, F Chen, Q Yang, G Du, and C Shan. Bioinspired transparent underwater superoleophobic and anti-oil surfaces. *Journal of Materials Chemistry A*, 3(18):9379, 2015.

[148] DG Stavenga, HL Leertouwer, T Hariyama, HA De Raedt, and BD Wilts. Sexual Dichromatism of the Damselfly *Calopteryx japonica* Caused by a Melanin-Chitin Multilayer in the Male Wing Veins. *PloS one*, 7(11):e49743, 2012.

[149] T Siefke, S Kroker, K Pfeiffer, O Puffky, K Dietrich, D Franta, I Ohlídal, A Szeghalmi, E-B Kley, and A Tünnermann. Materials pushing the application limits of wire grid polarizers further into the deep ultraviolet spectral range. *Advanced Optical Materials*, 4(11):1780–1786, 2016.

[150] WL Bond. Measurement of the refractive indices of several crystals. *Journal of Applied Physics*, 36(5):1674–1677, 1965.

[151] SM Luke, BT Hallam, and P Vukusic. Structural optimization for broadband scattering in several ultra-thin white beetle scales. *Applied optics*, 49(22):4246–4254, 2010.

[152] L Cortese, L Pattelli, F Utel, and S Vignolini. Anisotropic Light Transport in White Beetle Scales. *Advanced Optical Materials*, 3(10):1337, 2015.

[153] CW Mason. Structural colors in feathers. i. *The Journal of Physical Chemistry*, 27(3):201–251, 1923.

[154] RO Prum, GE Hill, and KJ McGraw. Anatomy, physics, and evolution of avian structural colors. In *Bird Coloration*, volume 1. Harvard University Press, Cambridge, 2006.

[155] P Vukusic, JR Sambles, CR Lawrence, and RJ Wootton. Quantified interference and diffraction in single morpho butterfly scales. *Proceedings of the Royal Society of London B: Biological Sciences*, 266(1427):1403–1411, 1999.

[156] RT Lee and GS Smith. Detailed electromagnetic simulation for the structural color of butterfly wings. *Applied Optics*, 48(21):4177–4190, 2009.

[157] A Saito, M Yonezawa, J Murase, S Juodkazis, V Mizeikis, M Akai-Kasaya, and Y Kuwahara. Numerical analysis on the optical role of nano-randomness on the morpho butterfly's scale. *Journal of nanoscience and nanotechnology*, 11(4):2785–2792, 2011.

[158] VE Johansen. Optical role of randomness for structured surfaces. *Applied optics*, 53(11):2405–2415, 2014.

[159] C Äkerlind, H Arwin, T Hallberg, and J Landin. Scattering and polarization properties of the scarab beetle Cyphochilus insulanus cuticle. *Applied Optics*, 54(19):6037, 2015.

[160] JW Galusha, LR Richey, JS Gardner, JN Cha, and MH Bartl. Discovery of a diamond-based photonic crystal structure in beetle scales. *Physical Review E*, 77(5):050904, 2008.

[161] BD Wilts, K Michielsen, and J Kuipers. Brilliant camouflage: photonic crystals in the diamond weevil, Entimus imperialis. *Proceedings of the Royal Society B: Biological Sciences*, 279(1738):2524, 2012.

[162] K Michielsen and DG Stavenga. Gyroid cuticular structures in butterfly wing scales: biological photonic crystals. *Journal of The Royal Society Interface*, 5(18):85, 2008.

[163] K Michielsen and H De Raedt. Reflectivity of the gyroid biophotonic crystals in the ventral wing scales of the Green Hairstreak butterfly, Callophrys rubi. *Journal of The Royal Society Interface*, 7(46):765, 2009.

[164] GE Schröder-Turk, S Wickham, H Averdunk, F Brink, JD Fitz Gerald, L Poladian, MCJ Large, and ST Hyde. The chiral structure of porous chitin within the wing-scales of Callophrys rubi. *Journal of Structural Biology*, 174(2):290, 2011.

[165] BD Wilts, K Michielsen, and H De Raedt. Iridescence and spectral filtering of the gyroid-type photonic crystals in Parides sesostris wing scales. *Interface Focus*, 2(5):681, 2011.

[166] BD Wilts, BA Zubiri, MA Klatt, B Butz, MG Fischer, ST Kelly, E Spiecker, U Steiner, and GE Schröder-Turk. Butterfly gyroid nanostructures as a time-frozen glimpse of intracellular membrane development. *Science Advances*, 3(4):e1603119, 2017.

[167] M Saba, BD Wilts, J Hielscher, and GE Schröder-Turk. Absence of Circular Polarisation in Reflections of Butterfly Wing Scales with Chiral Gyroid Structure. *Materials Today: Proceedings*, 1:193, 2014.

[168] H Kleinert. *Gauge fields in condensed matter / by Hagen Kleinert.* World Scientific, Singapore ; London, 1989.

[169] J Bertolotti. Designing disorder. *Nature Photonics*, 12(2):59, 2018.

[170] V Saranathan, AE Seago, A Sandy, and S Narayanan. Structural diversity of arthropod biophotonic nanostructures spans amphiphilic phase-space. *Nano Letters*, 15(6):3735, 2015.

[171] TM Trzeciak and P Vukusic. Photonic crystal fiber in the polychaete worm *Pherusa* sp. *Phys. Rev. E*, 80:061908, 2009.

[172] SM Pasteels, O Deparis, SR Mouchet, DM Windsor, and J Billen. Structural and physical evidence for an endocuticular gold reflector in the tortoise beetle, Charidotella ambita. *Arthropod Structure & Development*, 45(6):509, 2016.

[173] N Kristensen. *Morphology, Physiology, and Development*, volume 2. De Gruyter, Berlin, 2003.

[174] AC Neville. *Biology of the Arthropod Cuticle*. Springer-Verlag Berlin, Heidelberg, 1975.

[175] T van de Kamp, A Riedel, and H Greven. Micromorphology of the elytral cuticle of beetles, with an emphasis on weevils (Coleoptera: Curculionoidea). *Arthropod Structure & Development*, 45(1):14, 2016.

[176] L Picken. *The Organization of cells and other organisms*. Clarendon Press, Oxford, 1962.

[177] H Scherf. Beiträge zur kenntnis des cuticularpanzers der käfer auf grund von untersuchungen im polarisierten licht an larve, puppe und imago von Oryctes nasicornis L. *Zeitschrift für Morphologie und Ökologie der Tiere.*, 43(3):213, 1954.

[178] H Ghiradella. Structure and development of iridescent butterfly scales: Lattices and laminae. *Journal of Morphology*, 202(1):69, 1989.

[179] H Ghiradella. Structure of butterfly scales: patterning in an insect cuticle. *Microscopy Research and Technique*, 27(5):429, 1994.

[180] HT Ghiradella and MW Butler. Many variations on a few themes: a broader look at development of iridescent scales (and feathers). *Journal of The Royal Society Interface*, 6(Suppl. 2):S243, 2009.

[181] V Saranathan, CO Osuji, SGJ Mochrie, H Noh, S Narayanan, A Sandy, ER Dufresne, and RO Prum. Structure, function, and self-assembly of single network gyroid (I4132) photonic crystals in butterfly wing scales. *Proceedings of the National Academy of Sciences*, 107(26):11676, 2010.

[182] RO Prum, ER Dufresne, T Quinn, and K Waters. Development of colour-producing -keratin nanostructures in avian feather barbs. *Journal of The Royal Society Interface*, 6(Suppl. 2):S253, 2009.

[183] AR Parker. The diversity and implications of animal structural colours. *Journal of Experimental Biology*, 201(16):2343–2347, 1998.

[184] V Sharma, M Crne, JO Park, and M Srinivasarao. Structural origin of circularly polarized iridescence in jeweled beetles. *Science*, 325(5939):449, 2009.

[185] T Hunt, J Bergsten, and Z Levkanicova. A comprehensive phylogeny of beetles reveals the evolutionary origins of a superradiation. *Science*, 318(5858):1913, 2007.

[186] LF Del Rio, H Arwin, and K Järrendahl. Polarizing properties and structure of the cuticle of scarab beetles from the Chrysina genus. *Physical Review E*, 94(1), 2016.

[187] D Voigt, N Hosoda, J Schuppert, and S Gorb. On the laboratory rearing of green dock leaf beetles Gastrophysa viridula (Coleoptera: Chrysomelidae). *Insect Science*, 18(3):379, 2011.

[188] AC Neville and BM Luke. A Two-system model for chitin-protein complexes in insect cuticles. *Tissue and Cell*, 1(4):689, 1969.

[189] AC Neville and BM Luke. Molecular architecture of adult locust cuticle at the electron microscope level. *Tissue and Cell*, 1(2):355, 1969.

[190] T van de Kamp and H Greven. On the architecture of beetle elytra. *Entomologie heute*, 22:191–204, 2010.

[191] P Yeh. *Optical waves in layered media*. John Wiley & Sons inc., Hoboken, 2005.

[192] HL Leertouwer, BD Wilts, and DG Stavenga. Refractive index and dispersion of butterfly chitin and bird keratin measured by polarizing interference microscopy. *Optics Express*, 19(24):24061, 2011.

[193] DG Stavenga, HL Leertouwer, and BD Wilts. Quantifying the refractive index dispersion of a pigmented biological tissue using Jamin–Lebedeff interference microscopy. *Light: Science & Applications*, 2(9):e100, 2013.

[194] K Inaba, Y Takahashi, and K Ito. Critical role of a thiolate-quinone charge transfer complex and its adduct form in de novo disulfide bond generation by DsbB. *Proceedings of the National Academy of Sciences*, 103(2):287, 2006.

[195] Y Uesawa and K Mohri. Degradation of Methyldopa by Banana. *Pharmaceuticals*, 3(3):441, 2010.

[196] TM Trzeciak, BD Wilts, DG Stavenga, and P Vukusic. Variable multilayer reflection together with long-pass filtering pigment determines the wing coloration of papilionid butterflies of the nireus group. *Optics express*, 20(8):8877–8890, 2012.

[197] M Sugumaran. Complexities of cuticular pigmentation in insects. *Pigment Cell & Melanoma Research*, 22(5):523, 2009.

[198] SO Andersen. Insect cuticular sclerotization: A review. *Insect Biochemistry and Molecular Biology*, 40(3):166, 2010.

[199] B Moussian. Recent advances in understanding mechanisms of insect cuticle differentiation. *Insect Biochemistry and Molecular Biology*, 40(5):363, 2010.

[200] G Shamim, SK Ranjan, DM Pandey, and R Ramani. Biochemistry and biosynthesis of insect pigments. *European Journal of Entomology*, 2014.

[201] PJ Wittkopp and P Beldade. Development and evolution of insect pigmentation: Genetic mechanisms and the potential consequences of pleiotropy. *Seminars in Cell & Developmental Biology*, 20(1):65, 2009.

[202] KJ McGraw, EA Mackillop, J Dale, and ME Hauber. Different colors reveal different information: how nutritional stress affects the expression of melanin-and structurally based ornamental plumage. *Journal of Experimental Biology*, 205(23):3747–3755, 2002.

[203] MG Meadows, TE Roudybush, and KJ McGraw. Dietary protein level affects iridescent coloration in anna's hummingbirds, calypte anna. *Journal of Experimental Biology*, 215(16):2742–2750, 2012.

[204] J Örnborg, S Andersson, SC Griffith, and BC Sheldon. Seasonal changes in a ultraviolet structural colour signal in blue tits, parus caeruleus. *Biological Journal of the Linnean Society*, 76(2):237–245, 2002.

[205] RM Kilner. The evolution of egg colour and patterning in birds. *Biological Reviews*, 81(3):383–406, 2006.

[206] W Jetz, GH Thomas, JB Joy, K Hartmann, and AO Mooers. The global diversity of birds in space and time. *Nature*, 491(7424):444, 2012.

[207] CJ Vernon. On the eastern green-backed honeyguide. *Honeyguide*, 33:6–12, 1987.

[208] J Walton and R Martin. Secrets of the brown-backed honeybird. *African Birdlife*, pages 60–63, 2013.

[209] N Davies. *Cuckoo: cheating by nature*. Bloomsbury Publishing, London, 2015. p. 15.

[210] CN Spottiswoode, KF Stryjewski, S Quader, JFR Colebrook-Robjent, and MD Sorenson. Ancient host specificity within a single species of brood parasitic bird. *Proceedings of the National Academy of Sciences*, 108(43):17738–17742, 2011.

[211] CN Spottiswoode and M Stevens. How to evade a coevolving brood parasite: egg discrimination versus egg variability as host defences. *Proceedings of the Royal Society of London B: Biological Sciences*, page rspb20110401, 2011.

[212] MC Stoddard and M Stevens. Avian vision and the evolution of egg color mimicry in the common cuckoo. *Evolution*, 65(7):2004–2013, 2011.

[213] CN Spottiswoode and M Stevens. Visual modeling shows that avian host parents use multiple visual cues in rejecting parasitic eggs. *Proceedings of the National Academy of Sciences*, 107(19):8672–8676, 2010.

[214] GY Kennedy and HG Vevers. A survey of avian eggshell pigments. *Comparative Biochemistry and Physiology Part B: Comparative Biochemistry*, 55(1):117–123, 1976.

[215] N Davies. *Cuckoo: cheating by nature*. Bloomsbury Publishing, London, 2015. p. 120.

[216] T Birkhead. *The most perfect thing; inside (and outside) a bird's egg*. Bloomsbury Publishing, London, 2016. Chapter 2.

[217] EM Caves, M Stevens, ES Iversen, and CN Spottiswoode. Hosts of avian brood parasites have evolved egg signatures with elevated information content. In *Proceedings of the Royal Society B*, volume 282, page 20150598. The Royal Society, 2015.

[218] KH Falchuk, JM Contin, TS Dziedzic, Z Feng, T C French, G J Heffron, and M Montorzi. A role for biliverdin ixα in dorsal axis development of xenopus laevis embryos. *Proceedings of the National Academy of Sciences*, 99(1):251–256, 2002.

[219] A Verdes, W Cho, M Hossain, PLR Brennan, D Hanley, T Grim, ME Hauber, and M Holford. Nature's palette: Characterization of shared pigments in colorful avian and mollusk shells. *PloS one*, 10(12):e0143545, 2015.

[220] A Gorchein, CK Lim, and P Cassey. Extraction and analysis of colourful eggshell pigments using hplc and hplc/electrospray ionization tandem mass spectrometry. *Biomedical Chromatography*, 23(6):602–606, 2009.

[221] E Armstrong and C O'Dwyer. Artificial opal photonic crystals and inverse opal structures–fundamentals and applications from optics to energy storage. *Journal of Materials Chemistry C*, 3(24):6109–6143, 2015.

[222] G Van Dalen and MW Koster. 2d & 3d particle size analysis of micro-ct images. *Unilever Res Dev Netherlands*, 2012.

[223] C Bohren and DR Huffman. *Absorption and Scattering of Light by Small Particles*. Wiley Science Paperback Series, 1998. pp. 82-129.

[224] B Igic, D Fecheyr-Lippens, M Xiao, A Chan, D Hanley, PRL Brennan, T Grim, GIN Waterhouse, ME Hauber, and MD Shawkey. A nanostructural basis for gloss of avian eggshells. *Journal of The Royal Society Interface*, 12(103):20141210, 2015.

[225] HM Whitney, M Kolle, P Andrew, L Chittka, U Steiner, and BJ Glover. Floral iridescence, produced by diffractive optics, acts as a cue for animal pollinators. *Science*, 323(5910):130–133, 2009.

[226] J Moreno, JL Osorno, J Morales, S Merino, and G Tomás. Egg colouration and male parental effort in the pied flycatcher ficedula hypoleuca. *Journal of Avian Biology*, 35(4):300–304, 2004.

[227] D Walsh and S Mann. Fabrication of hollow porous shells of calcium carbonate from self-organizing media. *Nature*, 377(6547):320–323, 1995.

[228] KE Mikhailov. *Avian eggshells: an atlas of scanning electron micrographs*. British Ornithologists' Club, 1997.

[229] N Muller, J Haberko, C Marichy, and F Scheffold. Silicon hyperuniform disordered photonic materials with a pronounced gap in the shortwave infrared. *Advanced Optical Materials*, 2(2):115–119, 2014.

[230] C Battaglia, M Boccard, F-J Haug, and C Ballif. Light trapping in solar cells: When does a lambertian scatterer scatter lambertianly? *Journal of Applied Physics*, 112(9):094504, 2012.

[231] H Tributsch, H Goslowsky, U Küppers, and H Wetzel. Light collection and solar sensing through the polar bear pelt. *Solar energy materials*, 21(2-3):219–236, 1990.

[232] RE Grojean, JA Sousa, and MC Henry. Utilization of solar radiation by polar animals: an optical model for pelts. *Applied Optics*, 19(3):339–346, 1980.

[233] DW Koon. Is polar bear hair fiber optic? *Applied optics*, 37(15):3198–3200, 1998.

[234] P Thibault, M Dierolf, A Menzel, O Bunk, C David, and F Pfeiffer. High-resolution scanning x-ray diffraction microscopy. *Science*, 321(5887):379–382, 2008.

[235] M Holler, A Diaz, M Guizar-Sicairos, P Karvinen, E Färm, E Härkönen, M Ritala, A Menzel, J Raabe, and O Bunk. X-ray ptychographic computed tomography at 16 nm isotropic 3d resolution. *Scientific reports*, 4:3857, 2014.

[236] M Holler, M Guizar-Sicairos, EHR Tsai, R Dinapoli, E Müller, O Bunk, J Raabe, and G Aeppli. High-resolution non-destructive three-dimensional imaging of integrated circuits. *Nature*, 543(7645):402–406, 2017.

[237] K Yee. Numerical solution of initial boundary value problems involving maxwell's equations in isotropic media. *IEEE Transactions on antennas and propagation*, 14(3):302–307, 1966.

[238] K Parratt, JM Yao, GR Poirier, and N Yao. Plasma-etching of the organic layer in nacre. *Soft Nanoscience Letters*, 4(03):63, 2014.

[239] A Blanco and C López. Silicon onion-layer nanostructures arranged in three dimensions. *Advanced Materials*, 18(12):1593–1597, 2006.

[240] JL Shamshina, G Gurau, LE Block, LK Hansen, C Dingee, A Walters, and RD Rogers. Chitin–calcium alginate composite fibers for wound care dressings spun from ionic liquid solution. *Journal of Materials Chemistry B*, 2(25):3924–3936, 2014.

[241] TR Sarrubi, MF Ross, M Neisser, T Kocab, BT Beauchemin Jr, WR Livesay, SS Wong, and W Ng. Mechanism studies of scanning electron microscope measurement effects on 193-nm photoresists and the development of improved line-width measurement methods. In *26th Annual International Symposium on Microlithography*, pages 211–221. International Society for Optics and Photonics, 2001.

[242] N Tétreault, G von Freymann, M Deubel, M Hermatschweiler, F Pérez-Willard, S John, M Wegener, and GA Ozin. New route to three-dimensional photonic bandgap materials: Silicon double inversion of polymer templates. *Advanced Materials*, 18(4):457–460, 2006.

[243] DT Pierce and WE Spicer. Electronic structure of amorphous si from photoemission and optical studies. *Physical Review B*, 5(8):3017, 1972.

[244] DO Caplan. Laser communication transmitter and receiver design. *Journal of Optical and Fiber Communications Reports*, 4(4-5):225–362, 2007.

[245] K Barta and PC Ford. Catalytic conversion of nonfood woody biomass solids to organic liquids. *Accounts of chemical research*, 47(5):1503–1512, 2014.

[246] P Vukusic. Natural designs for manipulating the appearance of surfaces. *Ophthalmic and Physiological Optics*, 30(5):435–445, 2010.

[247] J H Braun, A Baidins, and R E Marganski. Tio2 pigment technology: a review. *Progress in organic coatings*, 20(2):105–138, 1992.

[248] A Weir, P Westerhoff, L Fabricius, K Hristovski, and N Von Goetz. Titanium dioxide nanoparticles in food and personal care products. *Environmental science & technology*, 46(4):2242–2250, 2012.

[249] S Bettini, E Boutet-Robinet, C Cartier, C Coméra, E Gaultier, J Dupuy, N Naud, S Taché, P Grysan, S Reguer, et al. Food-grade tio2 impairs intestinal and systemic immune homeostasis, initiates preneoplastic lesions and promotes aberrant crypt development in the rat colon. *Scientific reports*, 7, 2017.

[250] RD Perlack, LL Wright, AF Turhollow, RL Graham, BJ Stokes, and DC Erbach. Biomass as feedstock for a bioenergy and bioproducts industry: the technical feasibility of a billion-ton annual supply. Technical report, Oak Ridge National Lab TN, 2005.

[251] RJ Moon, A Martini, J Nairn, J Simonsen, and J Youngblood. Cellulose nanomaterials review: structure, properties and nanocomposites. *Chemical Society Reviews*, 40(7):3941–3994, 2011.

[252] S Tanpichai, F Quero, M Nogi, H Yano, RJ Young, T Lindström, WW Sampson, and SJ Eichhorn. Effective young's modulus of bacterial and microfibrillated cellulose fibrils in fibrous networks. *Biomacromolecules*, 13(5):1340–1349, 2012.

[253] T Saito, R Kuramae, J Wohlert, L A Berglund, and A Isogai. An ultrastrong nanofibrillar biomaterial: the strength of single cellulose nanofibrils revealed via sonication-induced fragmentation. *Biomacromolecules*, 14(1):248–253, 2012.

[254] N Lin and A Dufresne. Nanocellulose in biomedicine: Current status and future prospect. *European Polymer Journal*, 59:302–325, 2014.

[255] M Nogi, S Iwamoto, AN Nakagaito, and H Yano. Optically transparent nanofiber paper. *Advanced materials*, 21(16):1595–1598, 2009.

[256] MS Toivonen, S Kurki-Suonio, FH Schacher, S Hietala, OJ Rojas, and O Ikkala. Water-resistant, transparent hybrid nanopaper by physical cross-linking with chitosan. *Biomacromolecules*, 16(3):1062–1071, 2015.

[257] H Zhu, Z Fang, C Preston, Y Li, and L Hu. Transparent paper: fabrications, properties, and device applications. *Energy & Environmental Science*, 7(1):269–287, 2014.

[258] SM Mahpeykar, Y Zhao, X Li, Z Yang, Q Xu, Z-H Lu, EH Sargent, and X Wang. Cellulose nanocrystal: Polymer hybrid optical diffusers for index-matching-free light management in optoelectronic devices. *Advanced Optical Materials*, 2017.

[259] MS Toivonen, A Kaskela, OJ Rojas, EI Kauppinen, and O Ikkala. Ambient-dried cellulose nanofibril aerogel membranes with high tensile strength and their use for aerosol collection and templates for transparent, flexible devices. *Advanced Functional Materials*, 25(42):6618–6626, 2015.

[260] A J Benítez, J Torres-Rendon, M Poutanen, and A Walther. Humidity and multiscale structure govern mechanical properties and deformation modes in films of native cellulose nanofibrils. *Biomacromolecules*, 14(12):4497–4506, 2013.

[261] A Tejado and TGM van de Ven. Why does paper get stronger as it dries? *Materials Today*, 13(9):42–49, 2010.

[262] M Henriksson, L A Berglund, P Isaksson, T Lindstrom, and T Nishino. Cellulose nanopaper structures of high toughness. *Biomacromolecules*, 9(6):1579–1585, 2008.

[263] KMO Håkansson, IC Henriksson, C de la Peña Vázquez, V Kuzmenko, K Markstedt, P Enoksson, and P Gatenholm. Solidification of 3d printed nanofibril hydrogels into functional 3d cellulose structures. *Advanced Materials Technologies*, 1(7), 2016.

[264] SV Buldyrev, S Havlin, AY Kazakov, MGE Da Luz, EP Raposo, HE Stanley, and GM Viswanathan. Average time spent by lévy flights and walks on an interval with absorbing boundaries. *Physical Review E*, 64(4):041108, 2001.

[265] H Sehaqui, N Ezekiel Mushi, S Morimune, M Salajkova, T Nishino, and L A Berglund. Cellulose nanofiber orientation in nanopaper and nanocomposites by cold drawing. *ACS applied materials & interfaces*, 4(2):1043–1049, 2012.

[266] H Yano, J Sugiyama, A N Nakagaito, M Nogi, T Matsuura, M Hikita, and K Handa. Optically transparent composites reinforced with networks of bacterial nanofibers. *Advanced Materials*, 17(2):153–155, 2005.

[267] M Nogi and H Yano. Transparent nanocomposites based on cellulose produced by bacteria offer potential innovation in the electronics device industry. *Advanced Materials*, 20(10):1849–1852, 2008.

[268] A Rack, T Weitkamp, S Bauer Trabelsi, P Modregger, A Cecilia, T dos Santos Rolo, T Rack, D Haas, R Simon, R Heldele, M Schulz, B Mayzel, AN Danilewsky, T Waterstradt, W Diete, H Riesemeier, BR Müller, and T Baumbach. The micro-imaging station of the TopoTomo beamline at the ANKA synchrotron light source. *Nuclear Instruments and Methods in Physics Research Section B: Beam Interactions with Materials and Atoms*, 267(11):1978, 2009.

[269] A Cecilia, A Rack, P A Douissard, T Martin, T dos Santos Rolo, P Vagovič, E Hamann, T Van de Kamp, A Riedel, M Fiederle, and T Baumbach. LPE grown LSO:Tb scintillator films for high-resolution X-ray imaging applications at synchrotron light sources. *Nuclear Instruments and Methods in Physics Research Section A: Accelerators, Spectrometers, Detectors and Associated Equipment*, 648:S321, 2011.

[270] T dos Santos Rolo, A Ershov, T Van de Kamp, and T Baumbach. In vivo X-ray cine-tomography for tracking morphological dynamics. *Proceedings of the National Academy of Sciences*, 111(11):3921, 2014.

[271] M Vogelgesang, S Chilingaryan, T dos Santos Rolo, and A Kopmann. Ufo: A scalable gpu-based image processing framework for on-line monitoring. In *High Performance Computing and Communication & 2012 IEEE 9th International Conference on Embedded Software and Systems (HPCC-ICESS), 2012 IEEE 14th International Conference on*, pages 824–829. IEEE, 2012.

Appendix A

Beetle (Coleoptera) anatomy

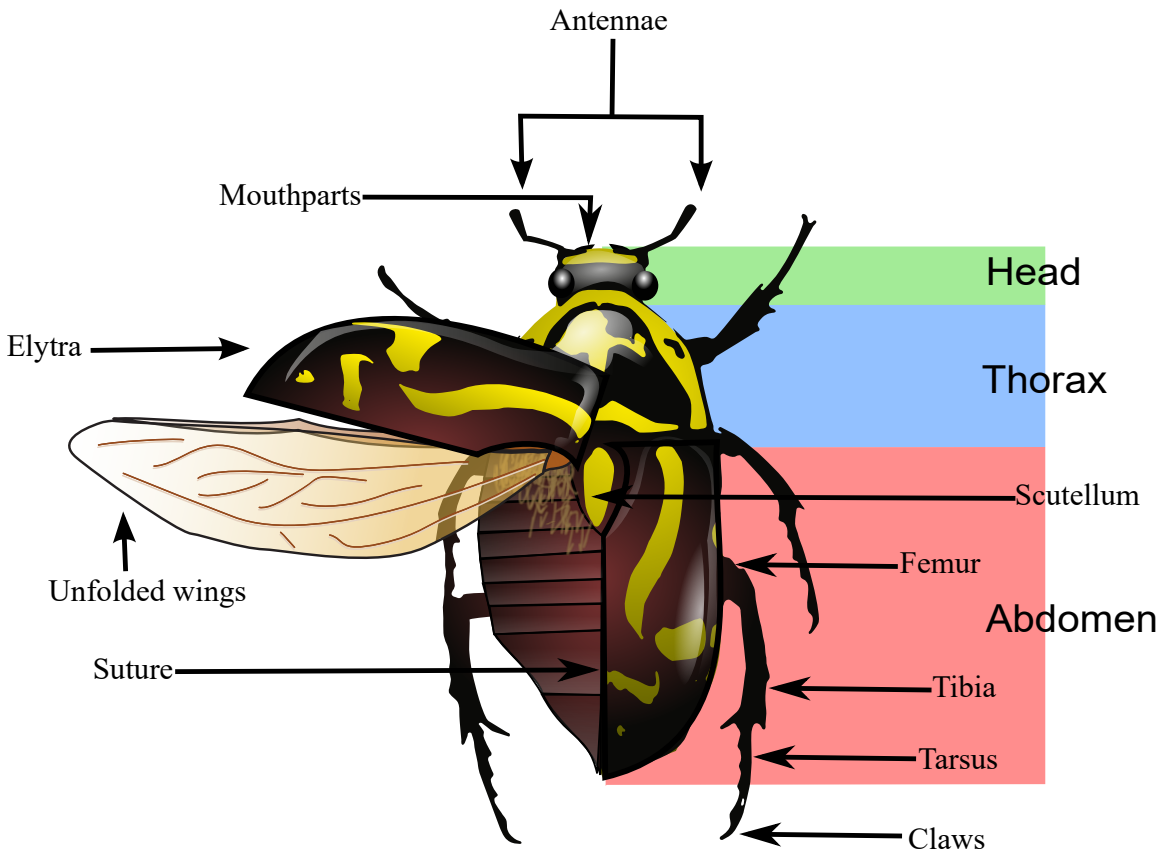

Fig. A.1 The parts that compose a beetle. Like the others insects, beetles show a three-part body formed by a head, a thorax, and an abdomen. The whole body is supported and protected by an external skeleton known as *exoskeleton*. Image by Nicholas Caffarilla, licensed under CC BY-SA 3.0.

Appendix B

Preparation of biological samples for microscopy

Transmission electron microscopy (TEM)

TEM sections of beetle elytra (see Appendix A) are prepared by Dr Jeremy Skepper and Janet Powell at the Cambridge Advanced Imaging Centre (CAIC) according to the following procedure: fixation is initiated by immersing the sample in a buffer containing glutaraldehyde (2 wt%), formaldehyde (2 wt%) and sodium cacodylate (0.05 M) at pH 7.4 for 18 hours at 4°C. Then the samples are rinsed five times with deionized water (DIW) and fixed for 48 hours at 4°C in a second buffer containing osmium ferricyanide (1 wt%) and sodium cacodylate (0.05 M) at pH 7.4. They are rinsed again in DIW and dehydrated in an ascending series of ethanol solutions from 50 wt% to 100 wt% dry ethanol. The next step is to bulk stain them with magnesium uranyl acetate (3 wt%) in pure dry ethanol for 48 hours at 4°C in the dark. Afterwards, the samples are rinsed 5 times in pure dry ethanol and repeatedly frozen and thawed in liquid nitrogen. This rinsing procedure is repeated 10 times in order to facilitate the subsequent infiltration with epoxy resin. The elytra are rinsed 5 times in dry ethanol (100 wt%), twice in dry acetone and 3 times in dry acetonitrile. They are incubated overnight in a 50/50 mixture of acetonitrile and Quetol 651 epoxy resin (without the catalyst BDMA) in uncapped tubes to allow the acetonitrile to gradually evaporate. They are subsequently placed in fresh Quetol (without BDMA) for 2 weeks and subsequently in Quetol 651 (with BDMA) for a further 2 weeks.

In order to perform vertical sectioning, the samples are oriented in a coffin mould and the resin is left to cure for a minimum of 48 hours at 65° C. Finally, the samples are sectioned at a thickness of 50–60 nm with a Leica UCT ultramicrotome using a 35° wedge angle

diamond knife (Diatome Ltd) and mounted on 300 mesh copper grids with a carbon film (EM Resolutions Ltd) for imaging.

A FEI Tecnai G2 operated at 200 kV (camera: AMT XR60B; software: Deben) is used to view the samples discussed in this thesis.

Scanning electron microscopy (SEM)

Samples are sectioned using a sharp scalpel and mounted on SEM stubs (Agar Scientific). Carbon tape (Elektron Technology) is used to attach the sections onto the stubs at the desired angle. For samples mounted on glass slides, conductive silver paste (Sigma-Aldrich) is used to bridge the slides and the stubs.

Non-conductive samples are sputter coated (Emitech) with Au/Pd for 7 s at 55 mA, resulting in a homogeneous coating about 2 nm thick.

Samples are imaged using a Leo Variable pressure SEM (Zeiss). The typical operating voltage was 1.3-3.0 kV with a working distance between 2 and 3 mm. Unless otherwise stated, an in-lens detector is used.

Focussed ion beam milling

Due to the higher voltages and the long exposure time involved in ion beam milling, the samples are prepared analogously to the one for SEM imaging but they are coated with a thicker conductive layer (Au for 3 minutes at 20 mA – the slow coating rate minimise the risk of cracks in the coating), typically 150 nm.

Table B.1 Parameters used for milling of eggshells and beetles cuticles. The current is the electric flow delivered by the ion beam, whilst the depth is the extent of the cut in the direction orthogonal to the sample plane.

Cut type	Avian eggshell		Beetle cuticle	
	Current (/nA)	Depth (/μm)	Current (/nA)	Depth (/μm)
Rough first cut	47.0	4	6.50	6
Normal cut	20.0	50	0.92	2
Fine cut for imaging	2.5	50	0.46	2

Synchrotron microtomography

Dead beetles at different life stages are immersed in an EtOH 70 % aqueous solution and scanned at the TOPO-TOMO beamline [268] of the ANKA Synchrotron Radiation Facility

at KIT (Germany) by Dr. Thomas van de Kamp and collaborators. 3,000 radiographic projections covering an angular range of 180° are acquired using a filtered polychromatic beam with the spectral peak at about 15 keV. An indirect detector system composed of a 12 μm LSO:Tb scintillator [269], diffraction limited optical microscope (Optique Peter) and 12 bit pco.dimax high speed camera with 2016 x 2016 pixels resolution [270] is employed to capture the frames with an exposure time of 16.6 ms each, resulting in an overall scan duration of 49.8 s. A 5x optical magnification leads to an effective pixel size of 2.44 μm. Tomographic reconstruction is performed with the GPU-accelerated filtered back projection algorithm implemented in the software framework UFO [271]. Volume renderings of tomographic data are performed with Drishti 2.5.

Appendix C

Fabrication methods

Plasma etcher

A PlasmaEtch Model RIE200 system is used to remove the upper layer of the samples when necessary. For decapping *Cyphochilus* scales (Figure C.1) a low pressure environment is used with a 20-80% Oxygen-Argon mixture. The optimal etching time for this application is 9-10 minutes.

Atomic Layer Deposition (ALD)

The ALD system used to deposit thin dieletric layers is a Savannah model by Cambridge Nanotech.

For the deposition of titania (TiO_2) the temperature of the deposition chamber is set to 110°C and the rate of coating is about 100 nm/24 hours. Titanium isopropoxide (Sigma-Aldrich, 97% purity) and deionised water are used as the metal and oxygen source, respectively.

Zinc oxide is deposited in an analogous manner (rate: 80nm/hour) starting from zinc (Sigma-Alrich, 98% purity) and deionised water.

Chemical Vapour Deposition (CVD)

The set up for CVD of amorphous silicon is designed and built by Dr. N. Muller under the supervision of Prof. F. Scheffold at the University of Fribourg (Switzerland).

The precursor used is disilane (Si_2H_6, Linde disilane 4.8) which deposits amorphous silicon (a-Si:H) at a rate of about 15nm/minute. The reaction is preferably conducted at 650°C in a low pressure environment.

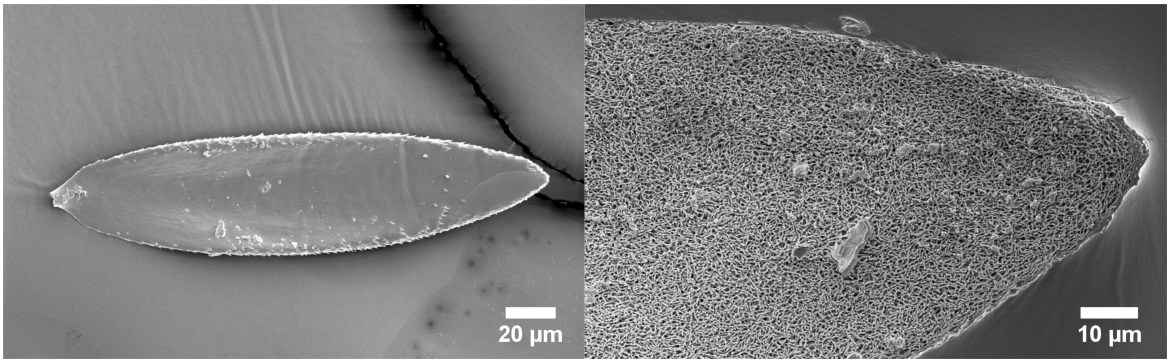

Fig. C.1 SEM images. On the left: a *Cyphochilus* scale before plasma etching. On the right: after plasma etching for 10 minutes the scales reveal their inner structure.

Acknowledgements

First and foremost my gratitude goes to my supervisor, Silvia Vignolini, for she has believed and invested in me ever since we met. Her door was always ajar and I never felt there was anything I could not discuss with her. I am also grateful for the warm and vibrant research group that she has created: I would like to thank all the present and past members of the Bio-Inspired Group (BIPs) for all the science and Cyber lunches that we shared over the years.

In particular, I would like to thank Gen who taught me so much when I joined the group and Villads who had infinite patience with my programming skills (and, even more importantly, bought the kettle for the common room). I want to thank Giulia for being the best lab mate I could have wished for: not only she continuously supported and helped me throughout the years but she was also a great friend to me - the Chip to my Dale. My gratitude goes to Gianni who went, in the blink of an eye, from being "my" student to teaching me a thing or two. I would like to thank Bruno for the most unlikely (and yet most interesting) conversations as well as Richard for the cutting jokes and for being the most proactive in providing help when I needed it, and when I did not know I needed it. A special acknowledgement goes to Ahu who made me fall in love with structural colours when I was a part III student looking for a project and introduced me to Silvia.

My gratitude extends to other departments in Cambridge: I would like to acknowledge Walter Federle and Yanmin Zhou for teaching me the secrets of beetle rearing. I would also like to thank Claire Spottiswoode for introducing me to the marvellous world of ornithology and letting me measure her *eggstraordinary* samples.

A paragraph of its own goes to the electron microscopists who mentored me and trusted me with some pretty expensive equipment: Jeremy Skepper at Cambridge Institute for Advanced Imaging, David Nicol at the Materials Science department, Jon "JJ" Rickard, Eric Tapley, and Richard Langford at the Cavendish Laboratory.

I would like to thank Bodo Wilts at the Adolf-Merckle Institute in Fribourg for the fruitful discussions and for being the best conference and winterschool companion: I feel privi-

leged to be able to send silly Snapchats to one of the most respected people in the field of biophotonics.

Also at the University of Fribourg I would like to thank Frank Scheffold for hosting me in his group, Nicolas Muller for sharing his double-inversion know-how, and Nathan Fuchs for powering through the speckle measurements with me.

At Aalto University, my gratitude goes to Olli Ikkala and Matti Toivonen for including me in their project and in their patent: it has been a real pleasure to work with you and I believe that our differences only made our work stronger.

At KIT (Karlsruhe Institute of Technology) I would like to thank Thomas van de Kamp for the x-ray tomography of the beetles and for bearing with my ignorance in entomology. Also at KIT I would like to thank Radwan Hasan Siddique for the discussion of many aspects of my work (and for the cheesecake!).

On a strictly IT-related note, I need to thank Krishna Kumar for the thesis' Latex template and, more in general, Stack Overflow for always having an answer to my coding questions.

I would also like to acknowledge my PhD examiners Jeremy Baumberg (University of Cambridge) and Pedro David Garcia Fernandez (ICN2) for the time that they have dedicated to reading and discussing this thesis with me and for their valuable additions.

Murray Edwards College has been my "home from home", just like the brochure promised, for over 7 years. I am extremely grateful for having had the opportunity to grow in such a special environment which made me not only a better physicist, under the supervision of Dr Saxton, but also a better woman.

At Murray Edwards I made friends that have supported me through the years (sometimes despite considerable geographical distances - Didi and Andreea, I am looking at you!) and that, without doubt, will last a lifetime. I am grateful to the ladies of the fifth floor in Canning & Eliza house for turning a blind eye about my cooking adventures and for listening to my occasional ranting. I would also like to thank the Murray Edwards Boat Club for keeping my *corpore sano* when my *mens* was *insana* and the Dome for spoiling me every Tuesday evening with a delicious menu.

I cannot thank enough Skype for making me feel at home whenever I needed. My gratitude

goes to my parents, Mirella and Savino, who always sustained me and kept my feet on the ground. A particular thank you goes to my mother who somehow managed to make me recover from glandular fever at the speed of light when I was just starting my PhD. My thoughts are also with my extended family, united in the sudden loss of my grandmother, Delia "Elide" Biocchi.

As if it was not enough to have one loving Italian family, I was also lucky to be welcomed in a British one: my gratitude goes to Gill and Martin for kindly hosting me in their house.

I have walked many miles in heavy boots, like Oskar Schell would say...until I met someone who would walk by my side and made me forget about the boots altogether: I would like to conclude with acknowledging il mio ragazzo, Connor, for he is the rock when I am a shipwreck.